



**Josué Danilo Molina Rodriguez**

**Amplitude analysis of the decay  $D^+ \rightarrow \pi^- \pi^+ \pi^+$  in  
the LHCb experiment**

**Tese de Doutorado**

Thesis presented to the Programa de Pós-Graduação em Física  
of the Departamento de Física do Centro Técnico Científico da  
PUC–Rio, as partial fulfillment of the requirements for the degree  
of Doutor em Física.

Advisor: Prof. Carla Göbel Burlamaqui de Mello

Rio de Janeiro  
September 2015



**Josué Danilo Molina Rodriguez**

**Amplitude analysis of the decay  $D^+ \rightarrow \pi^- \pi^+ \pi^+$  in  
the LHCb experiment**

Thesis presented to the Programa de Pós-Graduação em Física  
of the Departamento de Física do Centro Técnico Científico da  
PUC–Rio, as partial fulfillment of the requirements for the degree  
of Doutor.

**Prof. Carla Göbel Burlamaqui de Mello**

Advisor

Departamento de Física – PUC–Rio

**Prof. Tobias Frederico**

ITA

**Prof. Andre Sznajder**

UERJ

**Prof. Jussara Marques de Miranda**

CBPF

**Prof. Hiroshi Nunokawa**

Departamento de Física – PUC–Rio

**Prof. José Eugenio Leal**

Coordinator of the Centro Técnico Científico — PUC–Rio

Rio de Janeiro, September 10<sup>th</sup>, 2015

All rights reserved.

### **Josué Danilo Molina Rodriguez**

The author is graduated in Physics from Universidad Nacional Autónoma de Honduras – UNAH in 2008. He also studied Chemistry at the same university, and Mathematics at Universidad Pedagógica Nacional, Francisco Morazán – UPN-FM. He then obtained a Master's degree in Particle Physics at the PUC–Rio, in collaboration with the LHCb experiment.

#### Bibliographic data

Molina Rodriguez, Josué Danilo

Amplitude analysis of the decay  $D^+ \rightarrow \pi^- \pi^+ \pi^+$  in the LHCb experiment / Josué Danilo Molina Rodriguez ; advisor: Carla Göbel Burlamaqui de Mello. — 2015.

124 f. : il. ; 30 cm

Tese (Doutorado em Física)-Pontifícia Universidade Católica do Rio de Janeiro – PUC–Rio, Rio de Janeiro, 2015.

Inclui bibliografia

1. Física – Teses. 2. Física de Partículas;. 3. Análise de Dalitz plot;. 4. Violação CP;. 5. Modelo Isobárico;. 6. Análise de Ondas Parciais;. 7. Análise de Amplitudes;. 8. LHCb.. I. Göbel Burlamaqui de Mello, Carla. II. Pontifícia Universidade Católica do Rio de Janeiro – PUC–Rio. Departamento de Física. III. Título.

## Acknowledgments

Through the course of the four years of my PhD many talented and fundamental particles contributed to shape the universe of my research, from the big-bang to the ends of the space-time, to whom I am very grateful for having had the pleasure of working together, because without their help I would have been completely lost on the sea of uncertainty. “If they ever tell my story let them say that I walked with giants. Men rise and fall like the winter wheat, but these names will never die. Let them say I lived in the time of Hector, tamer of horses. Let them say I lived in the time of Achilles”<sup>1</sup>. Let them say I worked on the *LHCb Charm Rio Group*.

Firstly, I would like to express my profound gratitude to my advisor Carla Göbel, for the immense support in setting the course of my studies, the everyday kindness, as well as her continued guidance, her incentive for the realization of this work and for all the good things I learned from her.

To Alberto Reis, for his gentleness, his always relevant deep insights, different points of view and his passion for research. To Sandra Amato for her charisma and invaluable effort in the treatment of samples to be used in the different analyzes. To Erica Polycarpo, for always being willing to help and for the exciting discussions that she always established with the rest of the group.

To Danielle Tostes, for always being collaborating on anything needed, which greatly facilitated the research flow for all of us. Many thanks to my Dalitz plot analysis fellows, for the excellent working atmosphere: to Daniel Vieira and Clarissa Baesso, for the countless hours we spent discussing about the fitting code and the main components of the analysis, and to my crime partner, Rafael Aoude, for the outstanding work he has been doing, and for the nice friendship we developed over the last year.

I would also like to thank all the colleagues in the Physics Department for the great harmony. To Harold Camargo and Alexander Quiroga, for their invaluable help since my first visit to Brazil.

To the CNPq, CAPES and the PUC-Rio, for the financial support, without which this work would not have been realized.

Graças um milhão para Larissa Martins, Tia Vera, Andreia Martins e Carla Mello, pela enorme ajuda ao me cederem o espaço da sua casa e me acolherem como parte da família. Para Carlos Nunes, pelas eternas conversas que sempre tivemos sobre cinema, pelas dicas de filmes e seriados e pelos conselhos sobre como me tornar uma melhor pessoa na vida. Agradeço também ao meu caro amigo Pablo Adrián, pela amizade desinteressada, pelos momentos

<sup>1</sup>Odysseus character, from Troy film based on Homer's Iliad.

de descontraimento, pelas conversas e pela grande pessoa que ele é. Todos vocês fizeram mais leve o peso da vida cotidiana.

A mi papá, Danilo Molina, por enseñarme el valor de la honradéz y del trabajo. A mi madre, Marleny Lobo, por el regalo de la vida. A mi abuelita Julia, por convertirse en mi madre, por educarme y enseñarme valores morales. A mi abuelita Olinda, por sus constantes regaños y críticas para nunca permitirme ser conformista. A mis bellas tias, Soledad y Lourdes, por su enorme corazón y porque siempre estuvieron presentes cuando yo necesitaba una mano piadosa que me ayudase a levantarme. A mis hermanos maternos y paternos, a todos los amo por igual. A los miembros de mi familia en general, son tantos que resulta inviable mencionarlos a todos.

A mis amigos de Honduras, a Segisfredo Infante – presente siempre, cuando la hora del poema se aproxima, con sus consejos, sus libros y su particular visión enmedio de la bruma de nuestros tiempos –, Abraham Corleone – y a la pandilla del “Cubil Felino”, por el maizal, por el tabaco y por las innumerables e interesantes horas de conversación – y a Baltazar Alvarado – y todos sus hermanos, por los consejos, por las bromas y la complicidad –, gracias a todos por la amistad a prueba de balas y por mantener viva la llama de la amistad a pesar de la distancia y de los medios de incomunicación.

Al núcleo de la colonia Covespul de Tegucigalpa, principalmente a mi hermano Iván Lobo y mis amigos Tomás Cruz, Nery Romero, Kevin Acosta y Vera Acosta, por fortalecerme con sus saludos y conversaciones, por los excelentes recibimientos y porque las horas pasan de prisa, cual navío pirata que voga *entre el humo y la risa*, cuando estamos todos reunidos en santa comunión en “El Templo del Pensamiento”, haciéndole pucheros al jarabe de cebada.

A la pandilla de hondureños que nos reuníamos aquí en Rio – Darwin Pereira, Leonel Arévalo, Helmut Padilla y José Ramón Madrid – a sufrir por la Decepción Nacional, por las discusiones, las bromas y la diversión de siempre.

Y por último pero en primer lugar en mi corazón, a las dos bellas reinas que dirigen los destinos de mi existencia: a Karencita, por su enorme coraje, porque *sin su amor nada valgo, nada soy*, por darle orden a mis sueños, por hacerse cargo del trabajo pesado estos últimos meses y por las dos nuevas criaturitas que actualmente lleva en su vientre, que habrán de traer mucha alegría a nuestra casa; a mi hijita Camila, reyna de mi corazón y princesa de mis pensamientos, por traerle alegría a mi vida todos los días, por darle rumbo a mis pasos y por los besos con que me despierta cada mañana, que me animan a existir y a buscar siempre convertirme en un mejor ser humano.

## Abstract

Molina Rodriguez, Josué Danilo; Göbel Burlamaqui de Mello, Carla.  
**Amplitude analysis of the decay  $D^+ \rightarrow \pi^- \pi^+ \pi^+$  in the LHCb experiment.** Rio de Janeiro, 2015. 124p. PhD Thesis — Departamento de Física, Pontifícia Universidade Católica do Rio de Janeiro.

This thesis is dedicated to the study of the resonant structure of the  $D^+ \rightarrow \pi^- \pi^+ \pi^+$  decay mode using Dalitz plot analysis in a data sample corresponding to an integrated luminosity of  $2.0 \text{ fb}^{-1}$  of proton–proton collisions at 8 TeV recorded by the LHCb detector during 2012. The Dalitz Plot Analysis is a unique tool to investigate the spectroscopy of light mesons. In particular for the scalar sector there are a few  $\pi^- \pi^+$  resonances, such as the  $\sigma(500)$ ,  $f_0(980)$  and higher mass  $f_0$  states which are not well understood, with properties poorly known. The study of the Dalitz plot through and amplitude analysis is performed for about 600 thousand events of  $D^+ \rightarrow \pi^- \pi^+ \pi^+$  with two techniques. We first use the so-called Isobar Model, where the final state is described as a coherent sum of quasi two-body states. Within this formalism we find that the Dalitz plot is well represented by a combination of seven quasi-two-body decay channels, which are the  $\sigma(500)$ ,  $\rho(770)^0$ ,  $f_0(980)$ ,  $f_2(1250)$ ,  $f_0(1370)$ ,  $\rho(1450)^0$  and  $f_0(1500)$  resonances in the  $\pi^+ \pi^-$  system as well as a nonresonant (NR) component. Then a Model Independent Partial Wave Analysis (MI-PWA) to measure the  $S$ -wave component on the  $\pi^+ \pi^-$  system is also implemented for the first time on this channel. We show that  $D^+ \rightarrow \pi^- \pi^+ \pi^+$  decay is dominated by the  $S$ -wave structure.

## Keywords

Particle Physics; Dalitz Plot Analysis; CP Violation; Isobar Model; Partial Wave Analysis; Amplitude Analysis; LHCb.

## Resumo

Molina Rodriguez, Josué Danilo; Göbel Burlamaqui de Mello, Carla. **Análise de amplitudes do decaimento  $D^+ \rightarrow \pi^- \pi^+ \pi^+$  no experimento LHCb**. Rio de Janeiro, 2015. 124p. Tese de Doutorado — Departamento de Física, Pontifícia Universidade Católica do Rio de Janeiro.

Esta tese é dedicada ao estudo da estrutura ressonante do decaimento  $D^+ \rightarrow \pi^- \pi^+ \pi^+$  usando análise de Dalitz plot em uma amostra de dados correspondente a uma luminosidade integrada de  $2.0 \text{ fb}^{-1}$  de colisões próton-próton a 8 TeV coletadas pelo detector LHCb. A Análise de Dalitz Plot é uma ferramenta única para investigar a espectroscopia de mésons leves. Em particular, no setor escalar, existem algumas ressonâncias  $\pi^- \pi^+$ , como  $\sigma(500)$ ,  $f_0(980)$  e estados  $f_0$  de maior massa, que não são bem compreendidos, com propriedades pouco conhecidas. O estudo do Dalitz plot através da análise de amplitudes é realizado com aproximadamente 600 mil eventos de  $D \rightarrow \pi^- \pi^+ \pi^+$  usando duas técnicas. Primeiro, usamos o Modelo Isobárico, onde o estado final é definido como uma soma coerente de estados de quasi-dois corpos. Dentro desse formalismo, encontra-se que o Dalitz plot é bem representado pela combinação de sete canais quasi-dos corpos, que são  $\sigma(500)\pi^+$ ,  $\rho(770)^0\pi^+$ ,  $f_0(980)\pi^+$ ,  $f_2(1250)\pi^+$ ,  $f_0(1370)\pi^+$ ,  $\rho(1450)^0\pi^+$  e  $f_0(1500)\pi^+$ , bem como uma componente não-ressonante (NR). Então, uma análise de ondas parciais modelo-independente para medir a componente da onda-S no sistema  $\pi^- \pi^+$  é implementada pela primeira vez para este canal. Mostramos que o decaimento  $D^+ \rightarrow \pi^- \pi^+ \pi^+$  é dominado pela estrutura da onda-S.

## Palavras-chave

Física de Partículas; Análise de Dalitz plot; Violação CP; Modelo Isobárico; Análise de Ondas Parciais; Análise de Amplitudes; LHCb.

# Contents

1	Introduction	15
2	Phenomenology of Hadronic 3-Body Decays of D Mesons	18
2.1	Charmed Mesons	18
2.2	Kinematics of 3-Body Decays	22
2.3	Dalitz Plot	23
2.4	Introduction to Dalitz Plot Analysis	26
2.5	Experimental status	35
3	The LHCb Detector and the LHC acelerator	39
3.1	The LHC Experiments	40
3.2	The LHCb Detector	42
3.3	Track Reconstruction	43
3.4	Particle Identification	47
3.5	Trigger System	51
3.6	Online Selection System	52
3.7	LHCb Software Framework	53
3.8	Summary	54
4	Data Analysis	55
4.1	Main Variables For Sample Selection	57
4.2	Stripping Selection	59
4.3	Trigger Selection	61
4.4	Monte Carlo (MC) samples	62
4.5	Final Selection	63
4.6	Invariant mass fit	70
4.7	Signal efficiency variation across the Dalitz plot	73
4.8	Background	75
5	Dalitz plot fitting	78
5.1	Signal and Background PDF	79
5.2	Fitting procedure	80
5.3	Fitting algorithm consistency test	81
6	Results	87
6.1	Resonance models	87
6.2	Isobar fit results	88
6.3	MI-PWA fit results	97
7	Conclusions	103
A	Search for CP violation in the decay $D^+ \rightarrow \pi^- \pi^+ \pi^+$	109
B	Calculating fit fractions in $R_{\text{io}}^+$ .	121
B.1	Fractions and errors for the amplitude-phase form.	121



## List of Figures

2.1	Feynman diagrams for the charmed mesons decays.	20
2.2	Detail of the penguin diagram.	20
2.3	Tree and penguin diagrams for $D^+ \rightarrow \pi^- \pi^+ \pi^+$ decay.	21
2.4	Dalitz plot limits	24
2.5	Argand Diagram	28
2.6	Toy MC samples showing the shape of some possible resonant states in the $D^+ \rightarrow \pi^- \pi^+ \pi^+$ decay. The Non-Resonant (NR) state it is also showed as reference.	33
2.7	Dalitz plot	34
2.8	Dalitz plot distribution of the sample used by CLEO.	36
2.9	Mass and Dalitz plot distributions of the samples used by BABAR.	37
2.10	MI-PWA results for the BABAR analysis	38
3.1	LHCb luminosity	40
3.2	Location of the experiments at the LHC	41
3.3	Schematic overview of the CERN accelerator complex	41
3.4	LHCb luminosity	42
3.5	Side view of LHCb	42
3.6	Schematic view of the LHCb magnet	44
3.7	Geometry of VELO sensors.	45
3.8	VELO view	45
3.9	Tracker Turincensis	46
3.10	Tracking Stations T1-T3.	47
3.11	Graphs of RICH momentum distributions	48
3.12	RICH 1 and RICH 2	49
3.13	Muon System	50
3.14	Online Selection System	53
4.1	Topology of the production process of the $D$ meson and its decay $D^+ \rightarrow \pi^- \pi^+ \pi^+$ .	57
4.2	Mass spectrum for $D^+ \rightarrow \pi^- \pi^+ \pi^+$ after stripping and trigger cuts plus a muon veto.	62
4.3	Set of variables used in $D^+ \rightarrow \pi^- \pi^+ \pi^+$ selection. The signal and background efficiency for each cut, as well as the correspondent purity are showed. From this set, only $\log IP$ and $D \chi_{IP}^2$ show good signal-background separation, but they do not help to eliminate most of the background.	65
4.4	Second set of variables used in $D^+ \rightarrow \pi^- \pi^+ \pi^+$ selection.	66
4.5	Output from training showing the BDT efficiencies (up) and signal and background distributions (down).	69
4.6	Invariant-mass distribution of $D^+ \rightarrow \pi^- \pi^+ \pi^+$ candidates. The blue line shows the total $D^+$ pdf, the red line shows the combinatorial background, the green shows the total signal pdf from the two (light blue) Gaussians.	71
4.7	Dalitz plot distribution of the signal region.	72

4.8	(Top) Total efficiency across the $D^+ \rightarrow \pi^- \pi^+ \pi^+$ Dalitz plot histogram obtained after applying the selection criteria and weighed using the PIDCaLib package. (Bottom) the (left) same histogram in squared coordinates and (right) smoothed square DP using a cubic spline function.	75
4.9	Plot of sidebands.	76
4.10	Fitted Square DP obtained using spline interpolation for the sidebands regions showed above.	76
4.11	$K_s^0$ veto.	77
5.1	Gen-fit 1	82
5.2	Results of the MI-PWA consistency test. Up: comparison of the distribution from the generated toy MC sample (black dots) and the PDF with parameters from fit (blue line). The light color lines represent the lineshapes of the individual contributions. Down: comparison of the generated (red line) and fitted (blue dots) $S$ -wave. We can see that both the isobar generated sample, and the MI-PWA fit projections are in good agreement and hence we can be confident on the results when this method is applied to data.	85
6.1	Squared mass ( $s_{\text{low}}, s_{\text{high}}$ ) projections for the model-1. The dotted distribution represents the data, while the dark blue line represent the total PDF from the fit. Lineshapes for the intensity of individual contributions are also shown.	90
6.2	$s_{\text{low}}$ and $s_{\text{high}}$ projections for the model-2 PDF. Including the $\rho(1450)$ resonance to model-1 does not improves the fit quality substantially but its contribution can not be ignored.	91
6.3	Results for the model-3 are shown in this figure. It can be observed that the fit gets a little better on the high mass region, but even considering eight contributions, the isobar model does not give an acceptable result.	92
6.4	Squared mass projections illustrating model-4 results. The $f_0 X$ region gets better described when floating its mass and width.	93
6.5	Projection for model-5. As observed, we do not obtain a good fit when floating the $\sigma(500)$ mass and width.	94
6.6	Results for the model-6 are shown. In this figure it is possible to observe the complications that presents the isobar model for the $D^+ \rightarrow \pi^- \pi^+ \pi^+$ channel: even including all possible contributions, and floating the not well defined resonance parameters, the fit continues providing a poor performance.	95
6.7	Polar coordinates comparison of fitted quantities for model-3.	97
6.8	MI-PWA fit results.	99
6.9	MI-PWA magnitude and phase.	100

## List of Tables

2.1	Results for the nominal fits of E791 and CLEO Dalitz plot analysis. Errors are statistics and systematic.	35
4.1	Luminosity corresponding to the data sample used in this analysis.	55
4.2	Stripping20: Off-line selection criteria for the LHCb data in Run II (2012) for candidates of $D^+ \rightarrow \pi^- \pi^+ \pi^+$ .	60
4.3	Trigger selection applied to the $D$ candidates.	61
4.4	Analysis pre-selection requirements prior to BDT training	64
4.5	Variables used as inputs to train the BDT selection. Variable ranking from BDT training.	68
4.6	BDT configuration for the training.	68
4.7	Signal shape parameters obtained from unbinned fit to the $M(\pi^- \pi^+ \pi^+)$ invariant mass with two Gaussian functions.	71
4.8	Signal and sidebands regions	71
5.1	Generation parameters of the code validation tests, inspired in the E791 model.	81
6.1	Resonances that are included in the fit to the data sample. Parameters (and uncertainties) are taken from the PDG [56] unless stated otherwise.	87
6.2	Distribution of the different models used in the fit.	88
6.3	Results for magnitude, phase and fit fractions for the model–1. As mentioned above, $\sigma(500)$ and $\rho(770)$ dominates the decay. We can also observe secondary contributions from $f_2(1270)$ and $f_0(980)$ .	89
6.4	Results for the model–2. This is model–1 plus $\rho(1450)$ resonance. It can be seen that the $\rho(1450)$ fit fraction very small although not negligible.	90
6.5	Fit results for the model–3, which consists of model–2 plus the NR term. In this model we observe that all the contributions, but $\rho(1450)$ , $f_0(1370)$ and $f_0(1500)$ , are increased, while the NR fit fraction is about 8%, which means that it cannot be neglected.	91
6.6	Results for model–4. In this fit we allowed to float mass and width for $f_0 X$ . We observe that, compared to model–3, the $f_0 X$ fit fractions increases six times, while the NR decreases half of its previous value.	93
6.7	Model–5 results when mass and width for $\sigma(500)$ are allowed to float. The main point here is the lower $\sigma(500)$ fit fraction, compared to previous models.	94
6.8	Results for model–6, with eight resonances, with free masses and widths for $f_0 X$ and $\sigma(500)$ . This model increases the $f_0 X$ portion but maintain a low $\sigma(500)$ fit fraction and lowers the non–resonant contribution.	95
6.9	Summary of the models fitted using the Isobar Model. Results for all the relevant models are showed.	96

- 6.10 Results of the magnitude, phase and fraction for every included contribution on the MI-PWA fit. We can observe that the  $S$ -wave dominates de decay, with secondary contributions from  $\rho(770)$  and  $f_2(1270)$ . The  $\rho(1450)$  fit fraction is compatible with zero. In this fit, we used 86 free parameters, 82 from the  $S$ -wave and 4 for the  $f_2(1270)$  and  $\rho(1450)$  resonances parameters. 98
- 6.11 Fitted  $S$ -wave parameters at each mass bin edge in the form of magnitude and phase. 101

*What I Have Lived For:*

*Three passions, simple but overwhelmingly strong, have governed my life: the longing for love, the search for knowledge, and unbearable pity for the suffering of mankind. These passions, like great winds, have blown me hither and thither, in a wayward course, over a great ocean of anguish, reaching to the very verge of despair. I have sought love, first, because it brings ecstasy - ecstasy so great that I would often have sacrificed all the rest of life for a few hours of this joy. I have sought it, next, because it relieves loneliness—that terrible loneliness in which one shivering consciousness looks over the rim of the world into the cold unfathomable lifeless abyss. I have sought it finally, because in the union of love I have seen, in a mystic miniature, the prefiguring vision of the heaven that saints and poets have imagined. This is what I sought, and though it might seem too good for human life, this is what—at last—I have found.*

*With equal passion I have sought knowledge. I have wished to understand the hearts of men. I have wished to know why the stars shine. And I have tried to apprehend the Pythagorean power by which number holds sway above the flux. A little of this, but not much, I have achieved.*

*Love and knowledge, so far as they were possible, led upward toward the heavens. But always pity brought me back to earth. Echoes of cries of pain reverberate in my heart. Children in famine, victims tortured by oppressors, helpless old people a burden to their sons, and the whole world of loneliness, poverty, and pain make a mockery of what human life should be. I long to alleviate this evil, but I cannot, and I too suffer.*

*This has been my life. I have found it worth living, and would gladly live it again if the chance were offered me.*

**Bertrand Russel, *Autobiography*.**

# 1

## Introduction

*“The object of knowledge is what exists and its function to know about reality”.*

A deep look at the scientific foundations of nature is always an open door to new challenges that can lead us to magical moments of inner transformation. The scientist begins to live an unique experience, full of new questions that permeate daily life. After all, we are simply curious creatures asking questions that lead us to deeper issues. What is the nature of time? What interactions were present in the early universe? What is the universe and why it is composed of matter rather than antimatter? What, indeed, are the ultimate constituents of matter? And obviously, what is the nature of ultimate reality? Most of us have echoes from these questions constantly hammering in our heads. The merely act of asking these kind of questions has led mankind to build from scratch a set of thoughts, allowing us to clarify our position in the universe, but in turn, the light on such issues has provided us darker questions which we also seek the way to answer. The above quoted philosopher<sup>1</sup> stated that the object of knowledge, was not the *real reality*, because that was in the *Form*, so we must observe the object in order to figure out what the *Form* is.

Despite the immaterial case<sup>2</sup>, if ultimate reality is composed of matter and energy, the particle physicists have constructed a reliable method to bring our particular view of nature. This method involves mathematically consistent formulations or statements of proposed facts along with asseverations about relationships between the facts, in the form of physical laws called the *Standard Model*, which is subject to criticism and testing by observation and experiment. As this is the most consistent theory explaining the known forces of nature, keeping intact its principles after many experiments, it has earned the right to be given the task of explaining the status of the “actual facts”, or in better words if you wish, to explain reality.

The Standard Model [1–3] of particle physics is a gauge quantum field theory representing the synthesis of our current understanding of elementary particles and fundamental processes in nature, owing its outstanding success

<sup>1</sup>Plato, 428/427 or 424/423 BC

<sup>2</sup>Some philosophers may argue that our perceptions of the world around us cannot be knowledge. Immaterial reality then pertains to what is not constrained by physical laws, i.e. concepts such as *mind* and *Forms*.

to both profound theoretical insights and singular experimental research. It describes the dynamics of particles under the influence of the strong, weak and electromagnetic forces. The last two are described by a unified ElectroWeak theory, while the strong interaction is described by Quantum Chromodynamics (QCD)

With the prediction of the existence of the Higgs Boson which was observed recently by experiments at the CERN Large Hadron Collider (LHC) in 2012 [4,5], the unified electro-weak theory reached one of its biggest triumphs and highest peak of success in the road to describe what we think is the reality in nature. Nonetheless, various aspects of the Standard Model remain relatively poorly delimited by experiments, giving space to unanswered questions in different fields, prominent among CP violation<sup>3</sup>, one of such main questions regarding the nature of matter was quoted above, which may be answered from the study of hadron spectra.

Nonetheless, various aspects of the Standard Model remain relatively poorly constrained by experiment, prominent among which is the precise nature of CP violation.

QCD was developed 50 years ago. It is formulated in analogy to quantum electrodynamics (QED), with quarks that carry a color charge, and gluons which mediate the force between the quarks, as degrees of freedom. However, important differences with respect to QED prevent the deduction of the hadron spectrum from QCD. First of all, it is a non-abelian gauge theory, which manifests itself in the color charge of the gluons and their ability to interact among themselves. In this domain, the quarks and gluons are confined into color-neutral hadrons, which are the relevant degrees of freedom. Precise knowledge of the hadron spectrum is therefore essential in order to understand the strong interaction at low energies.

The hadronic decays of charmed particles have special characteristics that make them excellent laboratories for light quarks spectroscopy studies. The advantages of charm decays are many: always well defined initial state, with small non-resonant component which facilitates scalars identification; the fact of continuously covering the  $\pi^+ \pi^-$  mass spectrum till  $\sim 2 \text{ GeV}$ , which is known to be a semi-perturbative region. As we know, non-perturbative effects represent one of the major difficulties on the strong interactions studies. In this

<sup>3</sup>Although the Standard Model is compatible with CP violation in all observed hadron transitions, there are reasons to believe that there may exist new physics effects associated with CP violation in the decays of  $B$ ,  $D$  mesons which are incompatible with the Standard Model that might be observed at a previously inaccessible energy scale. As noted by Sakharov [6], CP violation is required for baryogenesis under the Big Bang model of the universe, yet the CP violation allowed under the Standard Model is not sufficient to explain the matter-antimatter asymmetry observed in the universe today.

sense, these particles, especially through its weak hadronic decays, represent a great testing ground for the study of weak interactions in the presence of strong interactions, as stated by the Constituent Quark Model (QCM), which has been very successful in describing the hadron spectrum and the description of the pseudo-scalars, vectorial and tensorial mesons nonet. Meanwhile, there is still no consensus with respect to the scalar mesons, as there are more states than the scalar nonet predicted by the quark model.

Light mesons can be studied by decays of heavy mesons to light hadronic states (intermediary resonances), decaying such resonances predominately into two bodies. Therefore, the observed final state may be the product of a decay chain where the produced resonances decay by strong interactions.

Since this thesis is concerned with the study of  $D$  meson decays into three charged pions, in addition to what was said in this chapter, in the next chapter we summarize a theoretical overview of selected topics in order to establish the importance of Dalitz Plot analysis of  $D^+ \rightarrow \pi^- \pi^+ \pi^+$ , starting from a general overview of the principles of hadronic decays of  $D$  meson, until the review of the full Dalitz plot analysis techniques.

On Chapters 3 and 4 we explain the main experimental related concepts, first we show a general overview of the LHCb detector and then we review the steps followed, with  $\sim 2 \text{ fb}^{-1}$  of data collected in 2012, in order to obtain the final sample prior to perform the Dalitz plot analysis, described in Chapter 5, with results shown in Chapter 6.

Conclusions from the main results and perspectives are presented in Chapter 7.

## Phenomenology of Hadronic 3-Body Decays of D Mesons

This chapter describes the general aspects of non-leptonic decays of  $D$  mesons. These decays are quite difficult to be treated theoretically due to the presence of strong interactions with the weak interaction responsible for the decay itself.

We shall see how the hadronic 3-body decays, despite its complexity, can be studied using an important technique called Dalitz Plot Analysis.

As we know, the Standard Model describes with great success the weak interactions between elementary particles through the exchange of mediators bosons ( $W^\pm$ ,  $Z^0$ ). In disintegrations of free quark where  $m_q \ll m_W$  (low energies compared to the  $W^\pm$  mass), we can write the effective amplitude as a current product as follows:

$$\mathcal{A} = \frac{4G_F}{\sqrt{2}} V^{q_1 q_2} V_{q_3 q_4} J^\mu J_\mu , \quad (2-1)$$

where  $V_{qq'}$  are the elements of the Cabibbo-Kobayashi-Maskawa (CKM) matrix [7, 8] and  $G_F$  is the Fermi constant [9].

Nevertheless, the Standard Model can not adequately describe the weak interactions between composite particles (mesons and baryons) due to the presence of the strong interaction.

### 2.1

#### Charmed Mesons

Mesons are grouped into scalar, pseudo scalar, vector, axial vector and so on, according to their quantum numbers  $J^{PC}$ , being  $J = L + S$  the total angular momentum,  $L$  the orbital angular momentum and the total spin  $S$  of the  $q_1 \bar{q}_2$  pair.  $P$  and  $C$  are the eigenvalues of parity and charge conjugation.

All mesons are unstable: they decay by strong, weak or electromagnetic interaction depending on their characteristics, and most of their masses come from binding energy and not from the mass sum of its constituents. One particular case of study are the charmed mesons.

According to the Standard Model, the  $c$  quark decays weakly<sup>1</sup> into an  $s$  or a  $d$  quark by the exchange of a virtual boson  $W^+$ . This type of decay  $c\bar{q}$  can be represented according to some of the annihilation diagrams,  $W^\pm$  exchange or quark mixing (just for the neutral  $D^0$ ).

<sup>1</sup>Known as flavour change.

In the annihilation diagram the  $c$  quark interacts with an initial antiquark annihilating and producing a boson  $W^\pm$  which soon produces a leptonic or hadronic pair. In the  $W^\pm$  exchange diagram, quarks of the initial state exchange a boson  $W^\pm$  and suppress each other. The mixing diagram is the double exchange of bosons and are very suppressed with respect to the previous diagrams.

The so-called external spectator diagram can couple the boson  $W^\pm$  both to a pair of leptons in semileptonic decay, or to a quark-antiquark pair in a hadronic decay in which the initial light quark behaves as spectator.

In the internal spectator diagram there exists no freedom in the choice of color, so the  $W$  can only couple to a quark-antiquark pair to hadronize and remain neutral in color, for this reason is called *color suppressed*. Penguin diagram involves strong interaction and considers virtual quarks *loops* in which the boson  $W^\pm$  is reabsorbed in the same line of quark from which it was emitted.

Figure 2.1, shows the basic processes described above; whereas in Figure 2.2 it is shown the loop process for a  $c$  quark in a flavor exchange  $c \rightarrow u\bar{q}q$ , a transition that is possible only by means of a penguin diagram, emitting a gluon which soon emits a quark-antiquark pair. These types of processes are of great interest because it is known that they can be especially sensitive to new physics effects. In our case we study the meson  $D^+(1869) = (c\bar{d})$  decaying into three pions.<sup>2</sup> Figure 2.3 shows the Feynman diagrams for the  $D^+ \rightarrow \pi^- \pi^+ \pi^+$  decay in which the final state can be reached either via tree or penguin contributions.

<sup>2</sup>In the expression  $D^+(1869)$  the value 1869 represents the  $D^+$  meson mass in  $\text{MeV}/c^2$  ( $c = 1$  in natural units).

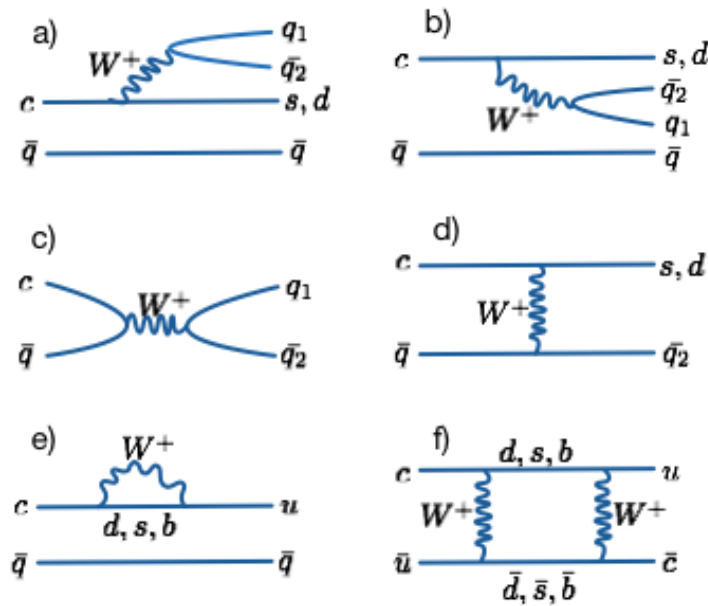


Figure 2.1: Feynman diagrams for the charmed mesons decays. (a) and (b) are external and internal spectator diagrams, respectively. (c) and (d) in turn show the annihilation diagrams  $c\bar{q}$  and boson exchange. The case in which the charmed meson makes a transition through a penguin is represented in (e), and the quark mixing diagram is represented by (f).

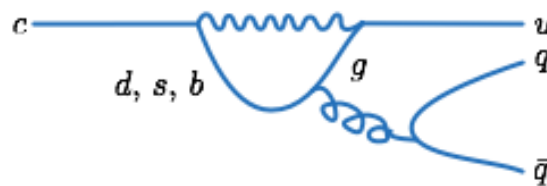


Figure 2.2: Detail of penguin diagram for the charm quark decay. The possible transitions in the loop are  $c \rightarrow d$ ,  $c \rightarrow s$  and  $c \rightarrow b$  each of them with the corresponding transition amplitude  $|V_{cq}|$ . However, the final transition probability is given by the expression  $|V_{cq}||V_{qu}|$ , which makes this quantity negligible in some cases. The gluon emitted from the loop produces a quark-antiquark pair which then form bound states with other quarks.

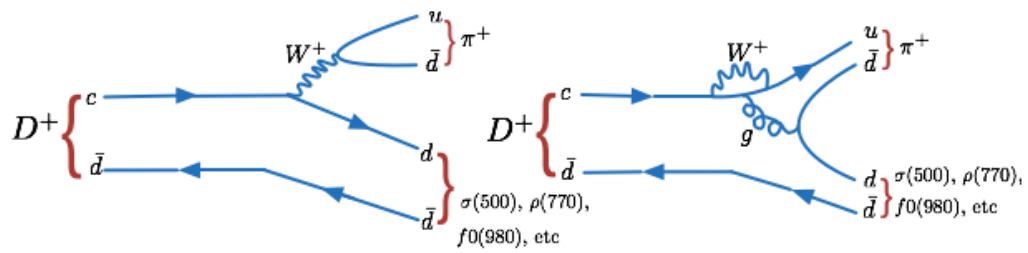


Figure 2.3: Tree and penguin diagrams for  $D^+ \rightarrow \pi^- \pi^+ \pi^+$  decay. Left, the decay as a tree diagram by external emission of  $W^+$  boson. Right we have the same final state via the penguin contribution.

## 2.2

### Kinematics of 3-Body Decays

In this section we shall describe general fundamentals of kinematics and dynamics of non-leptonic decays of  $D$  mesons into a three body final state.

Consider the decay of a spinless particle with mass  $M$  into three spinless particles with masses  $m_1$ ,  $m_2$  e  $m_3$ . Let us denote its 4-momenta as  $P$ ,  $p_1$ ,  $p_2$  and  $p_3$ , respectively.

$$P \rightarrow p_1 + p_2 + p_3 \quad (2-2)$$

To describe this decay there are in principle 9 degrees of freedom (from the three *tri-momenta* of the particles in the final state). There are four equations of energy-momentum conservation and, in the case of spinless particles, the decay is isotropic (in the rest frame of the decaying particle), thus the final state cannot be dependent on the three angles that describe the orientation. The set of available configurations for any array of kinematics variables is called *phase space*. These conditions define a surface, having dimension 2 in our case, which means that we only need two independent variables to describe the process.

Momentum-Energy conservation<sup>3</sup> demands

$$P^\mu = p_1^\mu + p_2^\mu + p_3^\mu . \quad (2-3)$$

We define the following invariants:

$$s = P^2 = M^2 , \quad (2-4)$$

$$s_{23} = (P - p_1)^2 = (p_2 + p_3)^2 , \quad (2-5)$$

$$s_{13} = (P - p_2)^2 = (p_3 + p_1)^2 , \quad (2-6)$$

$$s_{12} = (P - p_3)^2 = (p_1 + p_2)^2 . \quad (2-7)$$

Equations together with Eq. (2-3) lead to

$$s_{23} + s_{31} + s_{12} = M^2 + m_1^2 + m_2^2 + m_3^2 . \quad (2-8)$$

The invariants  $S_{ij}$  from Eqs. (2-6) to (2-7) represent the square of the invariant masses,  $m_{ij} = \sqrt{s_{ij}}$ , of the sub-system formed by particles  $i$  and  $j$ .

<sup>3</sup> We use natural units system, in which  $\hbar = 1$ .

## 2.3

### Dalitz Plot

Consider the decay process in the rest frame of the mother particle (CM). From Eq. (2-6) we have:

$$s_{23} = M^2 + m_1^2 - 2ME_1 . \quad (2-9)$$

However, knowing that

$$E_1 = \sqrt{m_1^2 + p_1^2} \geq m_1 , \quad (2-10)$$

we see that  $s_{23}$  will be maximum if  $E_1$  is minimum, i.e. when  $E_1 = m_1$ :

$$s_{23,\max} = M^2 + m_1^2 - 2Mm_1 = (M - m_1)^2 . \quad (2-11)$$

To find the minimum value of  $s_{23}$  we calculate in the CM frame of the (2,3) ensemble. There, we clearly see:

$$s_{23} = (p_2 + p_3)^2 = (E_1 + E_3)^2 \geq (m_2 + m_3)^2 . \quad (2-12)$$

Therefore, and considering that  $\vec{p}_2 = -\vec{p}_3$  in this frame

$$s_{23,\min} = (m_2 + m_3)^2 . \quad (2-13)$$

Analogously for the other subsystems, we have the following kinematic limits:

$$s_{23} \in [(m_2 + m_3)^2, (M - m_1)^2] , \quad (2-14)$$

$$s_{13} \in [(m_3 + m_1)^2, (M - m_2)^2] , \quad (2-15)$$

$$s_{12} \in [(m_1 + m_2)^2, (M - m_3)^2] . \quad (2-16)$$

As we have only two independent variables, each observed event of the process  $P \rightarrow p_1 + p_2 + p_3$  is represented by a point in the two-dimensional phase space which describes the decay. If two of these variables are used, the generated phase space is known as *Dalitz Plot*.

When imposing Eq. (2-8) condition to Eq. (2-14), Eq. (2-15) and Eq. (2-16), we obtain the minimum and maximum values that e.g.  $s_{13}$  can have, given  $s_{12}$ . We find:

$$s_{13\pm} = m_1^2 + m_3^2 + \frac{1}{2\sqrt{s_{12}}} [(s_{12} - s + m_3^2)(s_{12} + m_1^2 - m_2^2) \pm \lambda^{1/2}(s_{12}, s, m_3^2)\lambda^{1/2}(s_{12}, m_1^2, m_2^2)] , \quad (2-17)$$

where the kinematic *triangular function* is given by

$$\lambda(x, y, z) = x^2 + y^2 + z^2 - 2xy - 2yz - 2zx . \quad (2-18)$$

The contour described by Eq. (2-17) is the physical region (*phase space*) in which the decay takes place and is defined in terms of any pair of invariants  $s_{ij}$ , or in a more general way, it may be defined as a physical region in terms of any variables related to those of a linear transformation with constant *Jacobian*.

An example of Dalitz plot is shown in Figure 2.4 for the distribution corresponding to the invariant squared masses  $s_{12}$  and  $s_{23}$ .

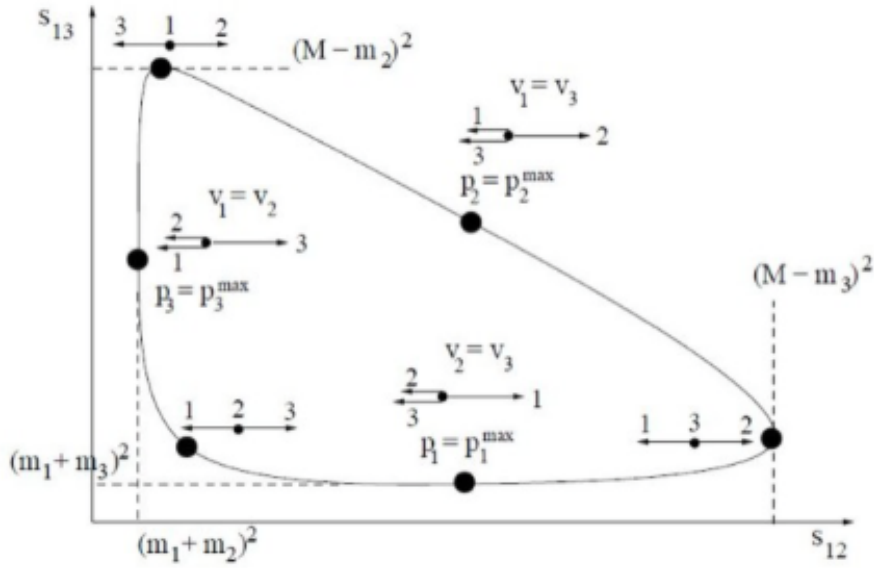


Figure 2.4: Dalitz plot limits showing the minimum and maximum configurations for the two-dimensional represented by  $s_{12}, s_{23}$ .

In order to understand the limits imposed by the momentum conservation in the phase space density, consider the integral of the decay rate

$$\Gamma = \frac{(2\pi)^4}{2M} \int |\mathcal{A}|^2 \delta^4(P - \sum_{i=1}^3 p_i) \prod_{i=1}^3 \frac{d^4 p_i}{2\pi^3} \delta(p_i^2 - m_i^2) , \quad (2-19)$$

where  $\mathcal{A}$  represents the quantum amplitude of the dynamic process responsible

for the decay, and the total moment and Einstein relation of each particle is defined by the 4-dimensional and 1-dimensional  $\delta$ -Dirac functions, respectively.

Using the property of  $\delta$ -Dirac to rewrite  $d^4 p_i \delta(p_i^2 - m_i^2)$

$$\delta[f(x)] = \frac{\delta(x - x_0)}{\left| \frac{df}{dx} \right|_{x_0}}, \quad (2-20)$$

we can express the decay rate in the CM reference as:

$$\Gamma = \frac{1}{2(2\pi)^5 M} \int |\mathcal{A}|^2 \delta^4(P - p_1 - p_2 - p_3) \frac{dp_1}{2E_1} \frac{dp_2}{2E_2} d^4 p_3 \delta(p_3^2 - m_3^2). \quad (2-21)$$

Performing some algebraic operations and defining

$$\delta_c = \delta \left( \cos \theta_{12} - \frac{M^2 + m_1^2 + m_2^2 - m_3^2 - 2M(E_1 + E_2) + 2E_1 E_2}{2p_1 p_2} \right) \quad (2-22)$$

the integral in  $d^4 p_3$  can be trivially solved to obtain a more compact expression for the decay rate

$$\Gamma = \frac{\pi^2}{2(2\pi)^5 M} \int |\mathcal{A}|^2 \delta_c dE_1 dE_2 d \cos \theta_{12} \quad (2-23)$$

which can be integrated for the cosine. Using the relations in Eq. (2-5), Eq. (2-6), Eq. (2-7) and Eq. (2-9), to express the decay rate in terms of Dalitz variables –where the total 4-moment configuration makes the decay occurs in a plane, and each event is represented by a point in the two-dimensional phase space of the system– it can be shown that:

$$\Gamma = \frac{1}{256\pi^3 M^3} \int |\mathcal{A}|^2 ds_{ij} ds_{jk}. \quad (2-24)$$

With this expression it is evident that the differential decay rate is proportional to the squared amplitude:

$$\frac{d\Gamma}{ds_{ij} ds_{jk}} \propto |\mathcal{A}|^2. \quad (2-25)$$

In this way, we can expect a complete description of the information about the dynamics of the decay to be contained in the distribution of the Dalitz plot.

## 2.4

### Introduction to Dalitz Plot Analysis

The Dalitz plot (DP) analysis technique has been widely explored as a tool to study three-body decays. It is particularly interesting for investigating the presence of resonant structures in quasi two-body states. An interesting application of the DP analysis is related to the study of charge parity (CP) violation, which is expressed, for example, by determining different characteristics for the particle and anti-particle decays. This manifests in particular when observing different branching ratios for a decay and its charge conjugated. Since the analysis deals directly with the amplitudes and phases of each intermediate state, doing such analysis separately for the decay and its conjugate would allow to study the CP violation: an indication of this effect would be to obtain different amplitudes and/or phases for particle and antiparticle. A fascinating application of these ideas is presented in Appendix A, where we show a model independent search for CP violation in  $D^+ \rightarrow \pi^- \pi^+ \pi^+$  [10], a work that I have contributed in the first half of my PhD.

#### 2.4.1

##### Isobar Model

The three-body decays of  $D$  meson are generally dominated by resonant processes in which  $D$  meson decays into two bodies, one of them being a resonance, which then decays by strong interaction, that is, for a  $D \rightarrow abc$  process the final state  $abc$  can be achieved with a contribution from the intermediate state [11]:

$$D \rightarrow rc \quad r \rightarrow ab \quad D \rightarrow (ab)c, \quad (2-26)$$

where  $r$  represents a resonant state that hereinafter decays to particles  $ab$ .

In Dalitz plot analysis based on the so-called Isobar Model [12], the total decay amplitude is represented as the coherent sum of a constant term (NR) for direct decay into three bodies and every possible resonance amplitude is commonly expressed as a resonance propagator multiplied by an angular distribution associated with the spin resonance, and form factors. Thus the array element of the sum of the partial amplitudes:

$$\mathcal{A} = a_{NR} e^{i\delta_{NR}} + \sum_i a_i e^{i\delta_i} \mathcal{A}_i(s_{12}, s_{13}). \quad (2-27)$$

The quantity  $a_i$  is the magnitude of the  $i$ -th channel and  $\delta_i$  is a phase; then two parameters for each intermediary state parameterize the relative contribution of each channel.

$\mathcal{A}_i = \mathcal{A}_i(m_i, s_{ij})$  is a function depending on the invariant masses and is usually described as a product of form factors, angular terms and lineshape propagators

$$\mathcal{A}_i = \underbrace{F_D F_r}_{\text{form factors}} \times \underbrace{\mathcal{M}_i^J}_{\text{angular function}} \times \underbrace{\mathcal{BW}_i}_{\text{lineshape-propagator}} \quad (2-28)$$

being the latter usually a relativistic Breit-Wigner function.

### Breit–Wigner Lineshape Propagator

For the resonance mass terms, several forms of dynamic models are proposed in the literature to parameterize various resonances. The most used is the Relativistic Breit–Wigner (RBW), which is suitable for narrow, isolated resonances

$$\mathcal{BW} = \frac{1}{m_0^2 - s_{ab} - im_0 \Gamma(\sqrt{s_{ab}})} \quad (2-29)$$

with

$$\Gamma(\sqrt{s_{ab}}) = \Gamma_0 \left( \frac{p^*}{p_0^*} \right)^{2L+1} \frac{m_0}{\sqrt{s_{ab}}} \left( \frac{F_L'(z)}{F_L'(z_0)} \right)^2 \quad (2-30)$$

$L$  is the quantum number of the angular momentum (as the particle decay into two pseudoscalar particles, the angular momentum of the 2-body final state,  $L$ , must equals the resonance's spin,  $J$ ), and  $\Gamma(\sqrt{s_{ab}})$  represents the decay width;  $p^*$  is the decay moment in the resonance frame and  $p_0^*$  is  $p^*$  calculated at nominal mass  $m_0$ .

In the complex plane, the amplitude follows a circle with radius 0.5 around  $0.5i$  in the anti-clockwise direction. Figure 2.5 shows this so-called Argand diagram of the complex plane. At the mass of the resonance, the amplitude is purely imaginary and the intensity, which is defined as the absolute value of the amplitude squared, is maximal. Going across the resonance, the phase of the amplitude varies by  $180^\circ$  and is  $90^\circ$  at  $m_0$  (Figure 2.5).

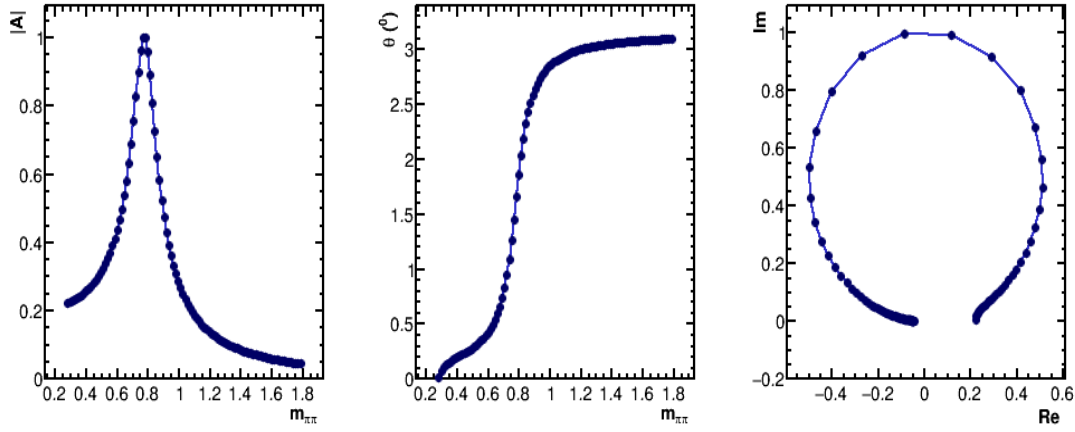


Figure 2.5: Argand diagram (right) using Relativistic Breit–Wigner function for a particle with  $\rho(770)$  characteristics ( $m_0$ ,  $\Gamma_0$ ). At  $m_0$  its intensity is maximal (left), while its phase is  $90^\circ$  (center).

### Blatt–Weisskopf barrier factors

$F_D$  ( $F_r$ ) represents the meson form factor according to the Blatt–Weisskopf parameterization [13], where  $z = |\vec{p}|r$ , represents the barrier factor in terms of a single parameter,  $r$ , the radius of the barrier, which we take to be  $5.0 \text{ GeV}^{-1}$  ( $1.5 \text{ GeV}^{-1}$ ), and the momenta  $|\vec{p}|$ , on the  $ij$  rest frame at  $m_{ij}$ .

The form of  $F_r = F_D$ , ( $F_r$ ), for angular momentum  $L$ , is:

$$F_r(z)_{L=0} = 1, \quad (2-31)$$

$$F_r(z)_{L=1} = \sqrt{\frac{1+z_0^2}{1+z^2}}, \quad (2-32)$$

$$F_r(z)_{L=2} = \sqrt{\frac{z_0^4 + 3z_0^2 + 9}{z^4 + 3z^2 + 9}}, \quad (2-33)$$

where  $z_0$  represents the value of  $z$  when the invariant mass is equal to the pole mass of the resonance.

### Angular Function

The angular dependence  $\mathcal{M}_i^J$  is described using Zemach tensors formalism [14],

$$\begin{aligned} \mathcal{M}_i^0 &= 1 \\ \mathcal{M}_i^1 &= -2\vec{p}_a \cdot \vec{p}_c \\ \mathcal{M}_i^2 &= \frac{4}{3} [3(\vec{p}_a \cdot \vec{p}_c)^2 - (|\vec{p}_a| |\vec{p}_c|)^2] \end{aligned} \quad (2-34)$$

## Nonresonant term

As the available phase space in the  $D^+ \rightarrow \pi^- \pi^+ \pi^+$  decay is small, it is assumed that the ( $S$ -wave) ‘non-resonant’ amplitude will have a constant value over the entire phase space. We parametrize its component using a complex constant amplitude (i.e. no form factors are introduced).

### 2.4.2

#### Resonance lineshapes

So far, we have described the most basic parametrization within the Isobar Model. Below, we describe alternative lineshapes for the resonant states that will be used/tested in our studies.

#### Gounaris–Sakurai lineshape

Strictly speaking, the Breit–Wigner parameterization works well only in the case of narrow states. The use of the mass-dependent width results in the amplitude  $\mathcal{A}(\sqrt{s_{ij}})$  becoming a nonanalytic function. An alternative parametrization proposed by Gounaris and Sakurai (GS) [15] recovers the analyticity of the amplitude and provides a better description for broad vector resonances such as  $\rho(770)$  and  $\rho(1450)$ :

$$\mathcal{A}(\sqrt{s_{ij}}) = \mathcal{A}_j(m) \frac{1 + d \cdot \Gamma_0/m_0}{(m_0^2 - m^2) + f(m) - i m_0 \Gamma(m)} , \quad (2-35)$$

where  $\Gamma_0$  is the nominal width of the  $\rho(770)$  or  $\rho(1450)$  mesons and  $M_\rho^2(s) = m_\rho^2 + f(s)$  were

$$\begin{aligned} f(m) &= \Gamma_0 \frac{m_0^2}{q_0^3} \left[ q^2 (h(m) - h(m_0)) + (m_0^2 - m^2) q_0^2 \frac{dh}{dm} \Big|_{m_0} \right] , \\ h(m) &= \frac{2}{\pi} \frac{q}{m} \ln \left( \frac{m + 2q}{2m_\pi} \right) , \\ \frac{dh}{dm} \Big|_{m_0} &= h(m_0) \left[ (8q_0^2)^{-1} - (2m_0^2)^{-1} \right] + (2\pi m_0^2)^{-1} , \\ d &= f(0)/(\Gamma_0 m_0) , \\ d &= \frac{3}{\pi} \frac{m_\pi^2}{q_0^2} \ln \left( \frac{m_0 + 2q_0}{2m_\pi} \right) + \frac{m_0}{2\pi q_0} - \frac{m_\pi^2 m_0}{\pi q_0^3} . \end{aligned} \quad (2-36)$$

### $\rho - \omega$ interference

The interference coming from the phenomenon known as  $\rho(770) - \omega(782)$  mixing is tested. To model this effect we use a composed lineshape:

$$\mathcal{A}_{\rho-\omega} GS(\sqrt{s_{ij}}, m_\rho, \Gamma_\rho) \times (1 + ae^{i\theta} BW(\sqrt{s_{ij}}, m_\omega, \Gamma_\omega)) \quad (2-37)$$

where  $\Gamma_\omega$  is taken as the nominal width of  $\omega(782)$ , and  $a, \theta$ , are real parameters obtained from previous measurements on the reaction  $e^+e^- \rightarrow \pi^+\pi^-$  [16].

### Alternative for spin-0 resonances

The use of relativistic Breit–Wigner shapes to describe resonances is known to fail when there is more than one overlapping amplitude input, or when there is significant interference with a non-resonant component, since the sum of the contributions in the isobar model violates unitarity. This constitutes a problem for the description of broad resonances, and in particular means that alternative models must be considered for the  $\pi\pi$  scalar sector, where there is known to be a broad ( $\Gamma \sim 500$  MeV) contribution from the  $\sigma(500)$  as well as significant  $f_0(980)$  and nonresonant (or very broad, or “slowly varying”) components.

In order to find the best description for data, various lineshapes were tested; here we briefly outline the different descriptions of those scalars considered as subjects of model variation.

### $\sigma(500)$ lineshape

In the  $\pi\pi$  system, the  $\sigma(500)$  resonance interferes strongly with a non-resonant (or “slowly varying”) term. The parameterisation of D.V.Bugg [17] has been used to combine these amplitudes in a physical way:

$$A_{\sigma(500)}(m_{\pi^+\pi^-}) = \rho(m_{\pi^+\pi^-}^2) \frac{m_{\pi^+\pi^-}^2 - m_A^2}{M^2 - m_{\pi^+\pi^-}^2} f(m_{\pi^+\pi^-}^2) e^{-\left(\frac{m_{\pi^+\pi^-}^2 - M^2}{A}\right)}. \quad (2-38)$$

$A$  is the Adler-Weinberg zero [18] term at  $A \approx M_K^2 - M_\pi^2/2$ . Several simple forms for  $(m_{\pi^+\pi^-}^2)$  were tried. Empirically, the best form is  $(m_{\pi^+\pi^-}^2) = b_1 + b_2 m_{\pi^+\pi^-}^2$ .

If the lineshape used is a complex pole, the mass and width of  $\sigma(500)$  are found from the position of the nearest pole in the process amplitude

$$\sqrt{s_{pole}} = M - i\Gamma/2. \quad (2-39)$$

In the case when using a RBW, the mass ( $471 \pm 21$ ) MeV and width ( $534 \pm 53$ ) MeV values were taken from Ref. [19].

### f<sub>0</sub>(980) lineshape

For resonances such as the  $f_0(980) \rightarrow \pi^+ \pi^-$  that lie close to the threshold of another channel ( $f_0(980) \rightarrow KK$  in this case), the effect of the opening of the second channel must be taken into account, for example, by employing the Flatte coupled channel form [20],

$$A_{f_0(980)}(m_{\pi^+ \pi^-}) = \frac{1}{m_R^2 - m_{\pi^+ \pi^-}^2 - im_R(g_{\pi\pi}\rho_{\pi\pi} + g_{KK}\rho_{KK})}. \quad (2-40)$$

The coupling constants  $g_{\pi\pi}$  and  $g_{KK}$  are the  $f_0(980)$  couplings to  $\pi^+ \pi^-$  and  $K^+ K^-$  final states respectively ( $0.165 \text{ GeV}^{-1}$ ,  $4.21 g_{\pi\pi} \text{ GeV}^{-1}$ ). Values of the mass and width of resonances are in general taken from world averages ([21]).

The phase-space factors  $\rho$  are given by Lorentz-invariant phase space

$$\rho_{\pi\pi} = \frac{2}{3} \sqrt{1 - \frac{4m_{\pi^\pm}^2}{m_{\pi^+ \pi^-}^2}} + \frac{1}{3} \sqrt{1 - \frac{4m_{\pi^0}^2}{m_{\pi^+ \pi^-}^2}}, \quad (2-41)$$

$$\rho_{KK} = \frac{1}{2} \sqrt{1 - \frac{4m_{K^\pm}^2}{m_{\pi^+ \pi^-}^2}} + \frac{1}{2} \sqrt{1 - \frac{4m_{K^0}^2}{m_{\pi^+ \pi^-}^2}}. \quad (2-42)$$

#### 2.4.3

##### Remarks on the Isobar Model

The way in which the full amplitude is defined so far is what we know as *Isobar Model*, which allows complete access to the informations of the three body decay (once trusting that this parameterization is acceptable); through a *likelihood* fit to the data we obtain values for  $a_i$ ,  $\phi_i$  and according to the probability density function  $|\mathcal{A}|^2$ , we can quantitatively see the contribution of each resonance in the Dalitz Plot phase space.

Using Toy Monte Carlo generated samples<sup>4</sup>, we can see the individual resonances behaviour. Figure 2.6 illustrates how various intermediate two-body states appear in the Dalitz plot. Unlike the uniform distribution of the phase-space decay (top left of the aforementioned figure, which is also the NR shape), scalar resonances appear as bands in the Dalitz plot. Angular distributions for vector and tensor intermediate states introduce characteristic non-uniformity of the event density along the resonance, bands with number of nodes equals to the spin of the particle. Finally, Figure 2.7 shows the complete Dalitz plot behavior when all those resonances are included in the model, simulated with a given set of  $a_i$  and  $\delta_i$  that are close to what is seen for real data, we clearly see how the region where the amplitudes of two resonances

<sup>4</sup>The concept of Toy MC will be explained later on chapter 4.

overlap is sensitive to the phase difference between the two amplitudes, so it is possible to observe the interference between resonances.

The decay fraction contributions are defined as a function of each resonance  $r$  parameters, with the integration in the entire Dalitz plot:

$$f_i = \frac{\int |\mathcal{M}_i|^2 ds_{12} ds_{13}}{\int |\mathcal{M}_{NR} + \sum_i \mathcal{M}_i|^2 ds_{12} ds_{13}} . \quad (2-43)$$

Detailed information with regard to decay fractions is shown in Appendix B.

#### 2.4.4

#### Model Independent Partial Wave Analysis (MI-PWA)

Even though in some cases the Isobar Model yields a good description of the data, one of its biggest issues, besides its model dependence, is that it has a limited ability in disentangling individual contributions from broad components in the  $S$ -wave. Although it is good for narrow, well separated states, it fails in particular to describe the overlap of broad resonances in the same wave. The use of relativistic BW shapes to describe resonances is known to fail when there is more than one overlapping resonance, or when there is significant interference with a nonresonant component, since modeling the  $S$ -wave as a superposition of Breit-Wigners is unphysical because it leads to a violation of unitarity when broad resonances overlap.

This constitutes a complication for the description of troublesome resonances, and in particular, it means that alternative models must be considered for the  $\pi^+ \pi^-$   $S$ -wave where there is known to be a broad ( $\Gamma \sim 500$  MeV) contribution from  $\sigma(500)$ , as well higher mass  $f_0$  states.

One of the possibilities in dealing with these issues is to describe the  $S$ -wave by means of the Model Independent Partial Wave Analysis technique, developed by the Fermilab E791 Collaboration [22], which is an attempt to alleviate the model dependency of the Isobar Model.

The main idea here is that the decay matrix element is written as a sum of partial waves, truncated at the  $D$ -wave (which is already a very small contribution).

Terms appearing in Eq. (2-27) are grouped according to the value of  $L(J)$ . The  $S$ -wave part (all terms with  $J = 0$ , including the NR) is factored

$$\mathcal{S} = S(\sqrt{s_{ij}}) \times \mathcal{M}_0^J(p^*, p_0^*) F_D(q^*, r_D, 0) \quad (2-44)$$

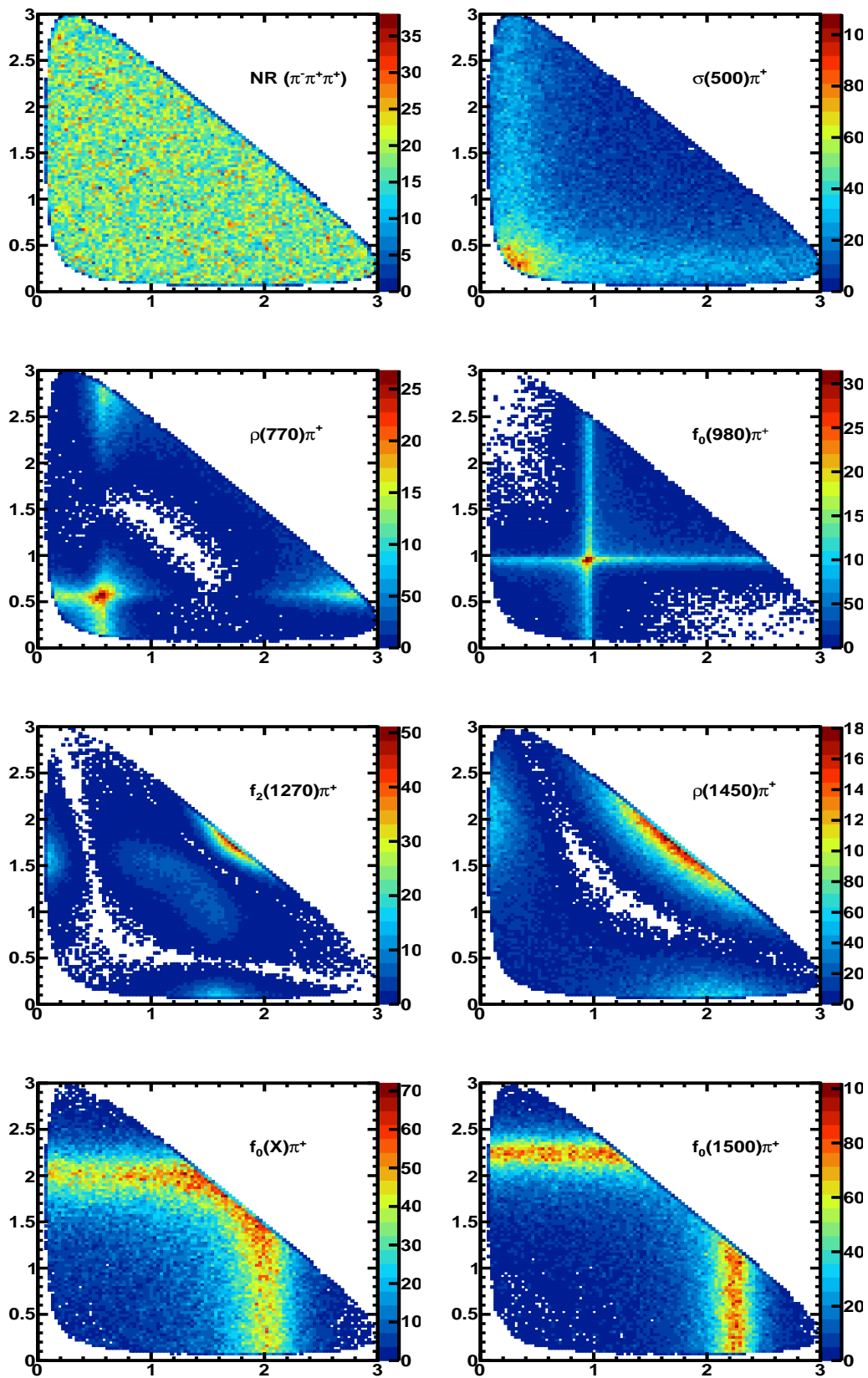


Figure 2.6: Toy MC samples showing the shape of some possible resonant states in the  $D^+ \rightarrow \pi^- \pi^+ \pi^+$  decay. The Non-Resonant (NR) state is also shown as reference.

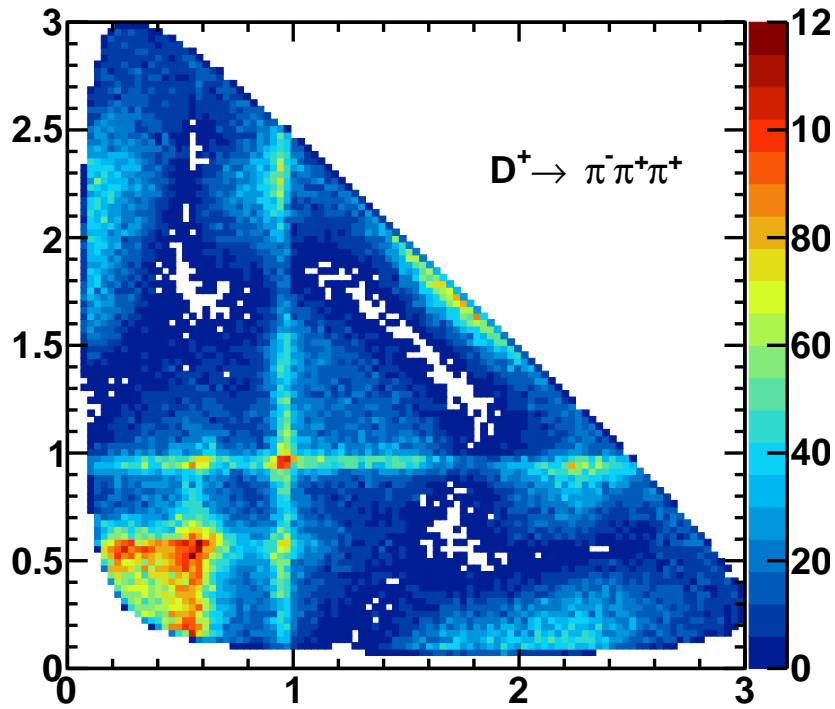


Figure 2.7: Dalitz representation for Toy MC generated sample with the known possible resonances showed in Fig. 2.6, with features similar to those in real data.

into a partial wave  $S(s)$ , describing the  $\pi^+\pi^-$  scattering, and the product  $\mathcal{M}_0^J(p^*, p_0^*)F_D(q^*, r_D, 0)$  describing the  $D$  decay<sup>5</sup>.

No assumption is made on the nature of the  $S$ -wave. Instead of including the  $S$ -wave amplitude as a superposition of relativistic Breit-Wigner functions, the  $\pi^+\pi^-$  mass spectrum is divided into  $n - 1$  slices and the  $S$ -wave its parameterized by an interpolation<sup>6</sup> between the  $n$  endpoints in the complex plane, so that two real numbers are fitted at each slice:

$$\mathcal{A}_{S\text{-wave}}(m_{\pi^+\pi^-}) = c_i e^{i\phi_i} \quad (2-45)$$

The  $c_i$  and  $\phi_i$  values are treated as model-independent parameters and are determined by a fit to the data.

The P- and D-waves ( $J = 1, 2$ , respectively) are assumed well represented by the isobar formalism consisting of a sum of Breit-Wigner amplitudes.

<sup>5</sup>Since  $L = 0$ , the product  $\mathcal{M}_0^J(p^*, p_0^*)F_D(q^*, r_D, 0)$  equals to 1.

<sup>6</sup>This interpolation is implemented by a Relaxed Cubic Spline.

Contribution	E791	CLEO
NR	$7.8 \pm 6.0 \pm 2.7$	–
$\rho(770)\pi^+$	$33.6 \pm 3.2 \pm 2.2$	$20.0 \pm 2.3 \pm 0.9$
$f_0(980)\pi^+$	$6.2 \pm 1.3 \pm 0.4$	$4.1 \pm 0.9 \pm 0.3$
$f_2(1270)\pi^+$	$19.4 \pm 2.5 \pm 0.4$	$18.2 \pm 2.6 \pm 0.7$
$f_0(1370)\pi^+$	$2.3 \pm 1.5 \pm 0.8$	$2.6 \pm 1.8 \pm 0.6$
$\rho(1450)\pi^+$	$0.7 \pm 0.7 \pm 0.3$	–
$f_0(1500)\pi^+$	–	$3.4 \pm 1.0 \pm 0.8$
$\sigma\pi^+$	$46.3 \pm 9.0 \pm 2.1$	$41.8 \pm 1.4 \pm 2.5$

Table 2.1: Results for the nominal fits of E791 and CLEO Dalitz plot analysis. Errors are statistics and systematic.

## 2.5

### Experimental status of $D^+ \rightarrow \pi^- \pi^+ \pi^+$ Decay

The  $D^+ \rightarrow \pi^- \pi^+ \pi^+$  decay has been previously studied by E791 Collaboration, using the isobar technique with  $\approx 1200$  events [23] and including a  $\sigma$  resonance. In contrast, FOCUS uses the K–matrix approach in  $\approx 1500$  events [24].

The most recent result comes from the CLEO Collaboration [25], using  $\approx 2600$  signal events. CLEO considers isobar models with different descriptions of the  $f_0(980)$  and  $\sigma$ . Events from the decay  $D^+ \rightarrow K_s^0 \pi^+$ , which has a large rate and contributes to the same final state, are isolated with a veto on the  $\pi^+ \pi^-$  invariant mass. An Isobar Model is used to parametrize the signal decay where the description from Bugg for the  $\sigma$  and Flatte parameterization for the threshold effects on the  $f_0(980)$  are included. Alternative models are also tried and give comparably good fit results. Table 2.1 shows the results for the nominal fits of the E791 and CLEO Dalitz plot analysis, whereas Fig. 2.8 shows the Dalitz plot of the data used in CLEO fit.

Though no Model Independent Partial Wave Analysis MI-PWA has been done on this channel, BABAR Collaboration [26] made an analysis for the  $D_s^+ \rightarrow \pi^- \pi^+ \pi^+$  using  $\approx 10000$  events, employing 40 points to fit the  $S$ -wave. Fig 2.9 shows the mass and Dalitz plot distributions for the data sample used, while Fig. 2.10 shows the magnitude and phase behaviour of the  $D_s^+ \rightarrow \pi^- \pi^+ \pi^+$  decay, as well as its comparison with previous results from FOCUS and E791 analysis.

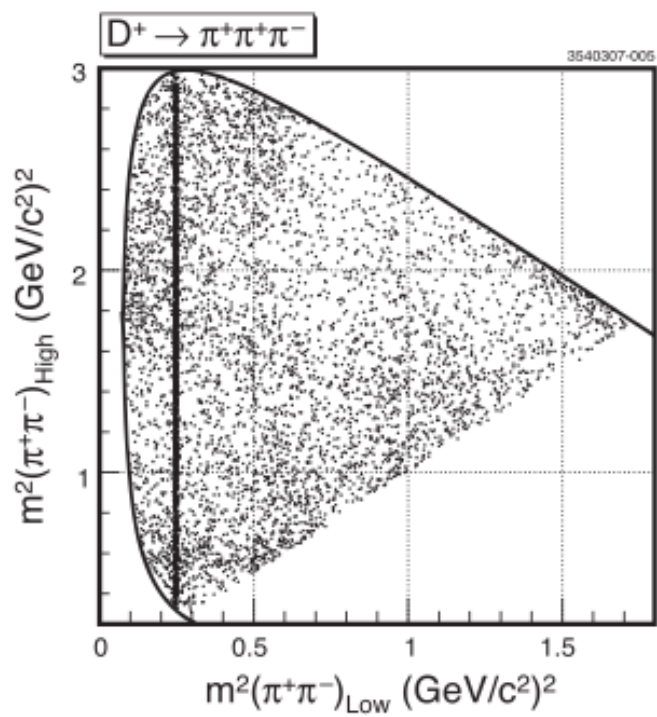


Figure 2.8: Dalitz plot distribution showing the sample used by CLEO as well as the veto on the  $K_s^0$ .

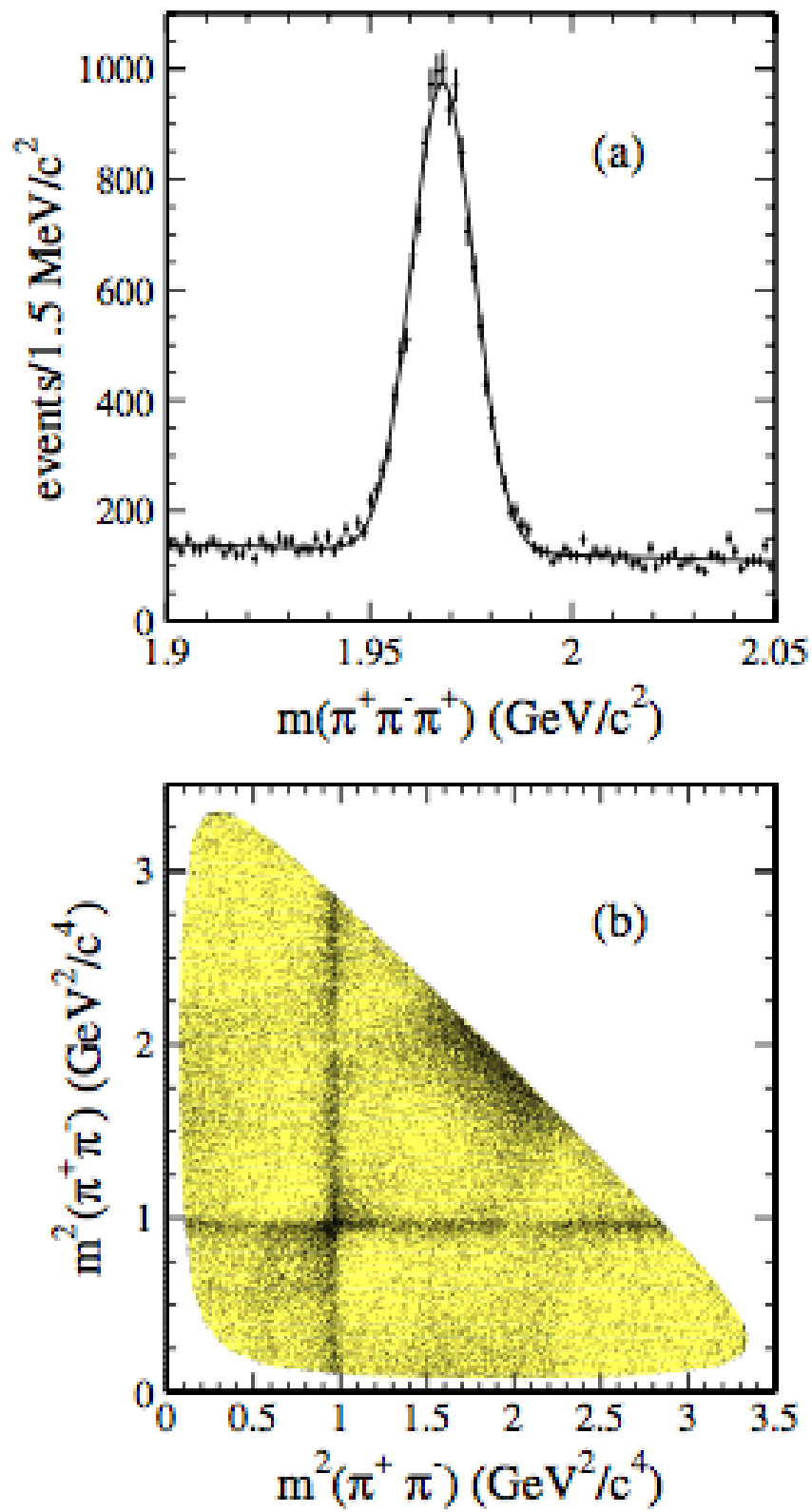


Figure 2.9: Mass and Dalitz plot distributions of the samples used by BABAR.

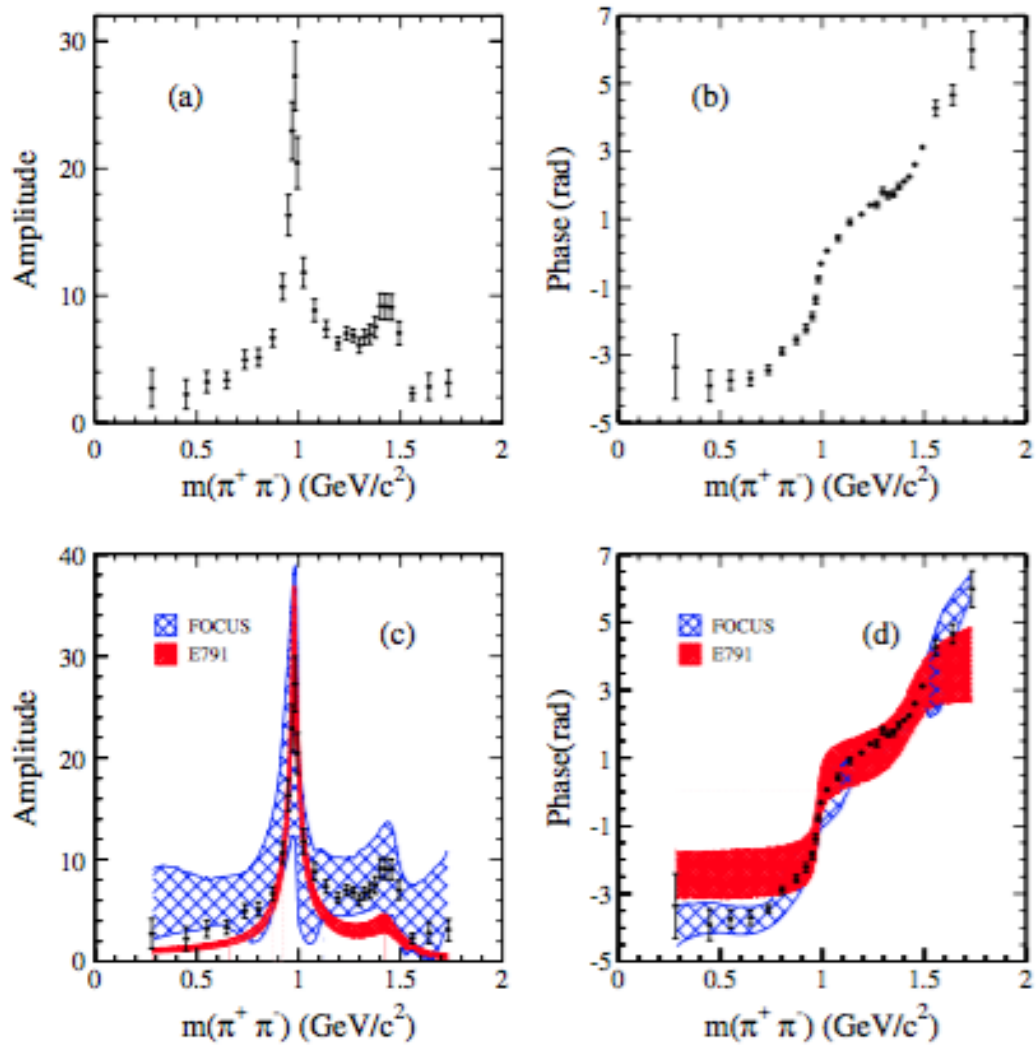


Figure 2.10: MI-PWA results for the BABAR analysis of the  $D_s^+ \rightarrow \pi^- \pi^+ \pi^+$  decay. Up: Magnitude and phase distribution of the  $S$ -wave fitted by BABAR. Down: Comparison with previous results from FOCUS and E791.

### 3

## The LHCb Detector and the LHC accelerator

The LHC [27] is the most powerful tool of particle physics in the world. Located beneath the border of France and Switzerland, near Geneva, it is a superconducting proton-proton collider originally designed to collide beams with a center of mass energy of 14 TeV and luminosity of  $10^{34} \text{ cm}^{-2}\text{s}^{-1}$ , with the main objective of reproducing -and testing- the Standard Model predictions in high energy collisions, as well as search for New Physics phenomenon. The analysis of these collisions could answer fundamental questions about our universe, such as: what is the origin of mass? Why there is an asymmetry in nature resulting in most matter than antimatter? In the 2012 data taking conditions the center of mass energy was 8.0 TeV (4 TeV by each proton beam).

The peak luminosity delivered by the LHC during this period reached values approaching  $10^{33} \text{ cm}^{-2}\text{s}^{-1}$  for the general purpose detectors. Luminosity is an important parameter for an accelerator, as it allows to estimate the expected event rate for a process with a known cross section or, in the other way around, to obtain the cross section from the measured rate of the process. The luminosity is defined as

$$L = f n \frac{N_1 N_2}{A} \quad (3-1)$$

where  $f$  is the revolution frequency,  $n$  is the number of proton bunches in each beam,  $N_i$  is the number of protons in each bunch for beam  $i$  and  $A$  is the cross sectional area of the beams. In order to estimate the number of events expected in a given data sample, the integrated luminosity  $L_{int} = \int L(t)dt$  is usually preferred with respect to the instantaneous luminosity,  $L$ . Fig. 3.8 illustrates the integrated luminosity over time.

In order to inject bunches of protons into the LHC for acceleration, a series of pre-accelerators is used. Hydrogen atoms are first stripped of their electrons to produce protons and subsequently accelerated to an energy of 50 MeV by a linear accelerator (Linac2). They are then injected into the Proton-Synchrotron Booster (PSB) followed by the Proton Synchrotron (PS), where they are accelerated to 25 GeV. From there, the Super Proton Synchrotron accelerates them to an energy of 450 GeV before they are injected into the LHC. In 2010 and 2011, the LHC reached an energy of 3.5 TeV per beam and in 2012 this was increased to 4 TeV per beam. An overview of the CERN accelerator complex is shown in Figure 3.2

The number of events generated in LHC collisions is determined by the

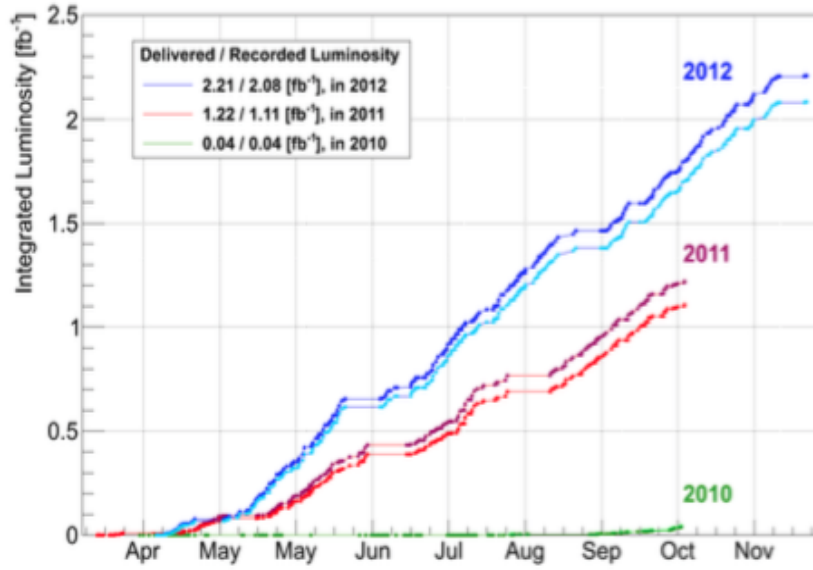


Figure 3.1: Cumulative integrated luminosity delivered to (2012) and recorded by LHCb (2010-2012).

expression

$$N_{events} = L\sigma_{pp} , \quad (3-2)$$

where  $\sigma_{pp}$  is the cross section, which depends only on beam parameters.

### 3.1 The LHC Experiments

Each of the four collision points of the LHC allocates a detector which captures and analyses the results from the proton collision. The four main experiments are:

#### *ALICE A Large Ion Collider Experiment*

It is a heavy ion (Pb-Pb nuclei) detector which is dedicated to the study of strong interactions (QCD) in extreme energy densities, where it is expected the formation of a new phase of matter, the plasma of quarks and gluons.

#### *ATLAS A Toroidal LHC Apparatus*

It is a general-purpose detector used to cover the broadest possible range of physics at the LHC, from the search for the Higgs boson to supersymmetry (SUSY) and extra dimensions.

**CMS** *Compact Muon Solenoid*

It is a general purpose detector with the same goals of ATLAS but with different techniques and conception.

**LHCb** *Large Hadron Collider beauty*

It is dedicated to the study of production and decays of hadrons containing the  $b$  and  $c$  quarks (heavy flavors), with emphasis to CP violation and rare decays.

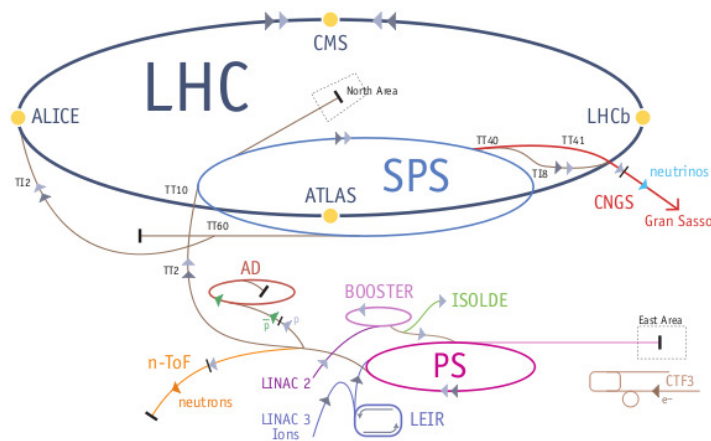


Figure 3.2: Location of the experiments on the 27 km circumference of the LHC.

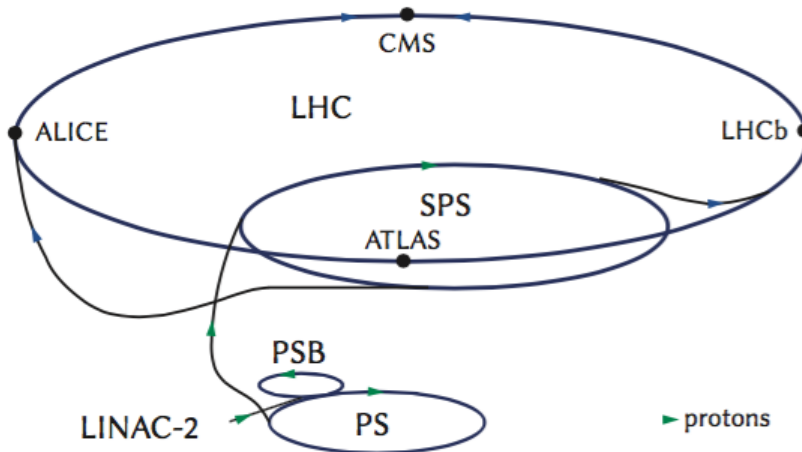


Figure 3.3: Schematic overview of the CERN accelerator complex. The location of the LHC experiments is also shown.

### 3.2 The LHCb Detector

The LHCb is an experiment dedicated to making precision measurements of heavy flavors in the LHC. It is a single arm detector that collects only frontal events, a geometry that was chosen taking into account that the proton-proton collision ( $pp$ ) will produce quark-antiquark pairs  $b\bar{b}$  mainly toward the collision axis (see Fig. 3.4), with a Lorentz *boost* which consequently forms a cone, and covers the angular limits of 15 mrad to 300 mrad in the horizontal plane and at 10 to 250 mrad in the vertical plane, as illustrated in Figure 3.5.

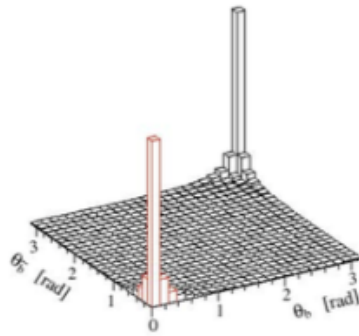


Figure 3.4: Polar angle distribution of  $b$  quark pairs produced at the LHC. It is clear that the majority of the quarks are produced in the forward and backward regions with the region of LHCb's acceptance highlighted in red.

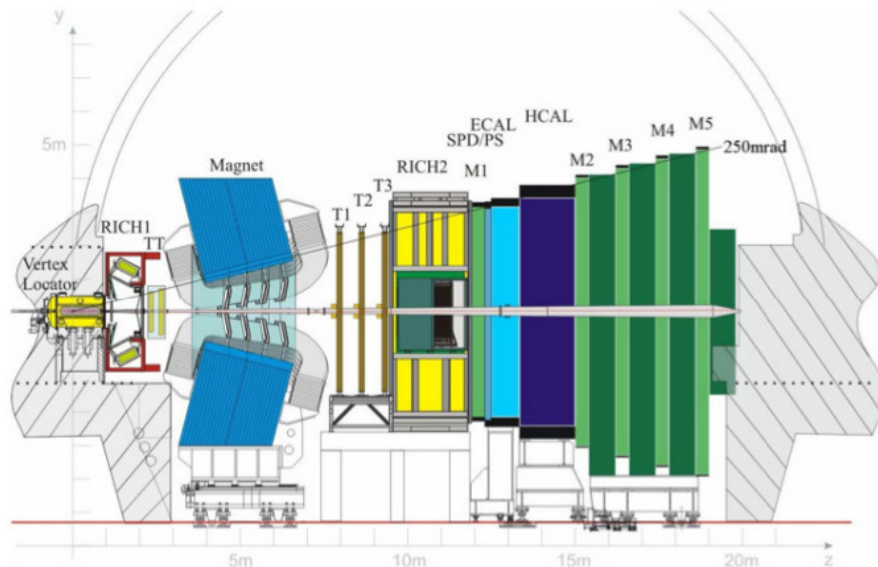


Figure 3.5: Side view of LHCb. It was adopted the positive side of the  $z$ -axis from the vertex of the interaction position to the muon detector. The  $y$  axis represents the vertical coordinate and the  $x$  axis is perpendicular to both.

### 3.3

#### Track Reconstruction

The beams produced by the LHC pass through the LHCb detector within a tube consisting of four conical sections having 2 to 6 meters in length and connected to a vacuum chamber where is located the VELO, which will be explained later. The first three segments of the beam-pipe located after the vacuum chamber are composed of beryllium and measuring 1.9, 3.7 and 6.0 m respectively. Beryllium was chosen because of its transparency and elasticity since, as LHCb looks for events in directions near to the direction of the beam, the properties of the beam-pipe directly influence the data taking, and characteristics of the amount of material traversed by the particles have a direct impact on information collected.

#### 3.3.1

##### The Magnet

A magnetic dipole [28] is used in the experiment for measurements of charge and linear momentum of charged particles. The linear moment are measured by the deflection due to the dominant component of the magnetic field  $B_y$  and therefore the trajectories are observed in the plane  $xz$ . The integrated field is:

$$\int B_y dz = 4.2 \text{ Tm} \quad (3-3)$$

In order to achieve the required momentum resolution for charged particles, the full magnetic field must be measured with a relative precision  $\sim 10^{-4}$ , and the position of the  $B$  field peak with accuracy of a few millimeters. The measurement of three magnetic components is provided by the mapping of the field inside the detector track volume. The LHCb magnet has the ability of changing the orientation of the magnet field with respect to the  $y$  axis: it can be upwards (called MagUp) or downwards (MagDown). In 2012, indeed, half of the data was taken with MagUp orientation and the other one with MagDown configuration. Figure 3.6 presents a schematic view of the LHCb magnet.

#### 3.3.2

##### Tracking System

The LHCb tracking system consists of the VELO and four planar track stations as explained below. It is designed to provide efficient reconstruction

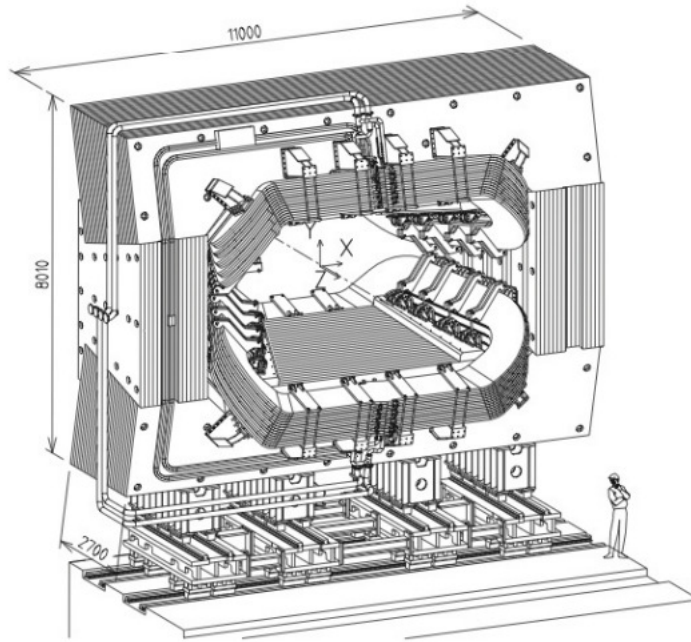


Figure 3.6: Schematic view of the LHCb magnet

of charged-particle tracks.

### Vertex Locator (VELO)

The ability to reconstruct the tracks of the particles is of fundamental importance in the LHCb. The VELO [29] is the sub-detector closest to the primary interaction region. It is designed to measure the trajectory of charged particles as well as pinpoint their origin. Charged particles can emanate from a primary vertex (PV) i.e. a proton-proton interaction within the detector acceptance, or from the decay of any long-lived particles that produce secondary decay vertices (SVs) which are distinct from any PVs in the event.

The VELO consists of 21 stations placed along the beam axis, each counting with two measurement planes; a plan ( $r$ -sensor) is used to measure the radial coordinates ( $r$ ), and the second plane ( $\phi$ -sensor) is in charge of measuring the azimuth coordinates<sup>1</sup> ( $\phi$ ). The third coordinate is obtained from the knowledge of each sensor plane position within the experiment. Fig 3.7 illustrates the geometry of the VELO sensors. In addition to track and vertex reconstruction the VELO also plays a role in the high level trigger at LHCb.

<sup>1</sup>We chose the cylindrical coordinate system to allow a fast track reconstruction and provide the spatial information  $3 - D$ .



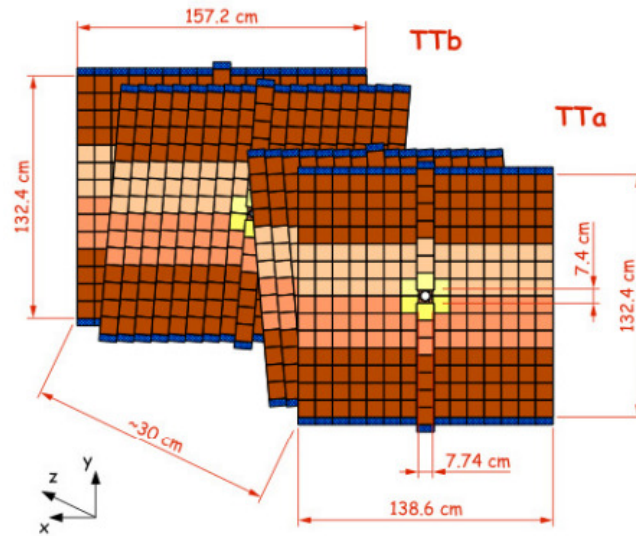


Figure 3.9: Tracker Turicensis. Arrangement of the TT layers, rotated in  $\pm 5^\circ$ .

respectively in  $-5^\circ$  and  $5^\circ$  in the canonical LHCb reference frame, which facilitates the work of the trajectory reconstruction algorithms (see Figure 3.9).

### Inner Tracker

It covers a roughly 120 cm wide and 40 cm high cross-shaped region in the centre of three large planar tracking stations downstream of the magnet. It uses silicon strips technology and covers the inner region corresponding to around 20% of the particle flow.

### Outer Tracker

It is located on the outer region of the T stations, aims to detect the position of the tracks that are in the acceptance region of the LHCb, with an angle greater than 15 mrad. An illustration of the Inner and Outer Tracker stations can be seen in figure 3.10

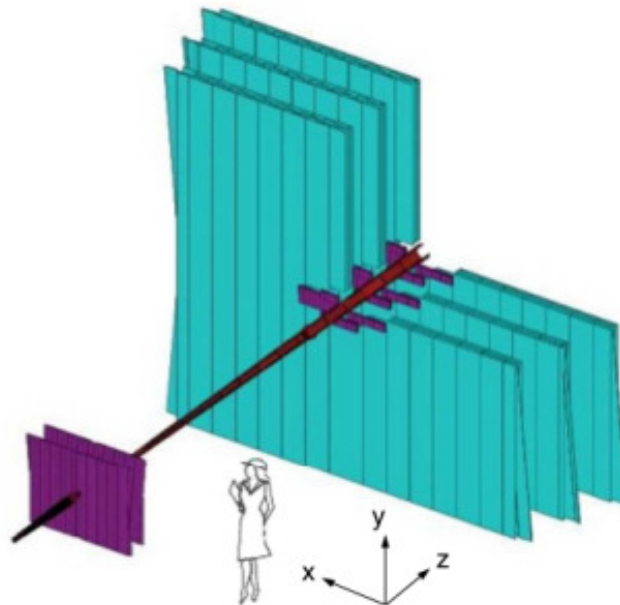


Figure 3.10: Tracking Stations Inner Trackers (purple) and Outer trackers (green).

### 3.4 Particle Identification

For the study of decays of heavy flavor hadrons, it is essential to identify them and their daughters. Thus for experimental purposes it is an absolutely necessary requirement to separate, for example, kaons from pions. The LHCb Particle Identification (PID) system consists of RICH detectors, calorimeters and muon detectors. Electrons are detected in the electromagnetic calorimeter, muons in the muon chambers, pions, kaons and protons are separated by RICH and have their energy measured; at the hadron calorimeter for all hadrons in general. The neutral particles are identified in the electromagnetic calorimeter (photons and  $\pi^0$ 's) or hadron calorimeter (neutrons).

#### 3.4.1 RICH

The RICH<sup>2</sup> [33] is based on the effect known as Cherenkov radiation to determine the velocity of a particle by measuring the angle at which emits radiation. The Cherenkov effect constitutes electromagnetic radiation emitted by particles that propagate at higher speed than light in a given medium.

For large polar angles the spectrum of momentum is smooth, while for small angles this spectrum is increased, so the PID system<sup>3</sup> consists of two

<sup>2</sup>Ring-Imaging Cherenkov detector.

<sup>3</sup>We will use PID whenever we speak of Particle Identification.

RICH detectors which will be explained below, to fully cover the range of momentums shown in Figure 3.11.

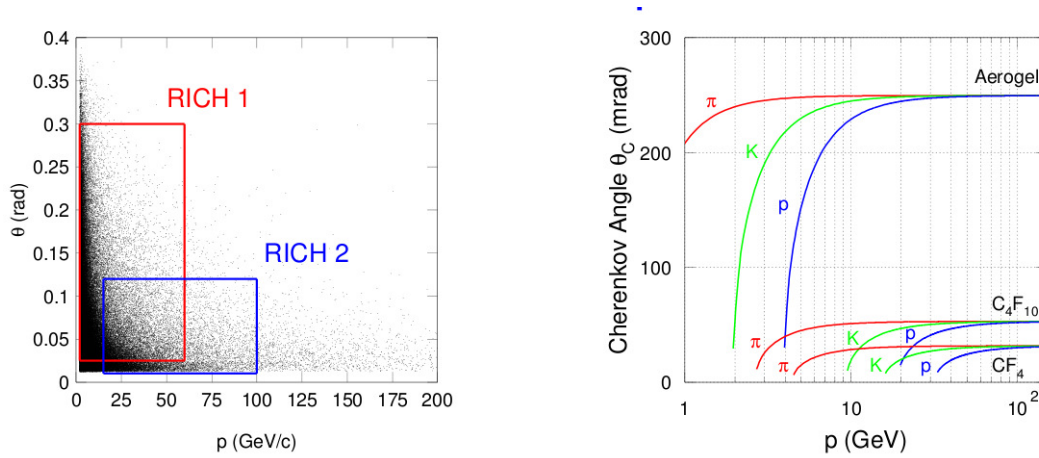


Figure 3.11: Graphs of RICH momentum distributions. Left: scatter plot of events with Cherenkov radiation angle as a function of momentum. Right: Graph showing the various momentum intervals for the particles.

## RICH 1

Located between the VELO and Trigger Tracker detectors, the RICH 1 is used to identify charged particles with low momentum ( $\sim 1 - 60$  GeV/c), employing Aerogel and FluoroButano ( $C_4F_{10}$ ) radiators.

## RICH 2

Located between the Outer Tracker and the Electromagnetic Calorimeter, it contains the tetrafluoromethane ( $CF_4$ ) gas radiator, and provides PID to high momentum particles (from 15 to 100 GeV/c) within the acceptance region of the polar angle  $\pm 120$  mrad (horizontal) up to 100 mrad (vertical). The representation of both RICH detectors 1 and 2 may be observed in Figure 3.12.

### 3.4.2 Calorimeter System

The main scope of calorimeters system [34] is to identify candidates for the first level trigger ( $L0$ ) as hadrons, photons and electrons to measure their energy and the position of each of them. The particles, when crossing plaques of dense material, generate showers of lighter particles and lower energy. These showers excite internal states of particles of a scintillator that emits radiation in a well-defined wavelength. The measurement of the photons from this

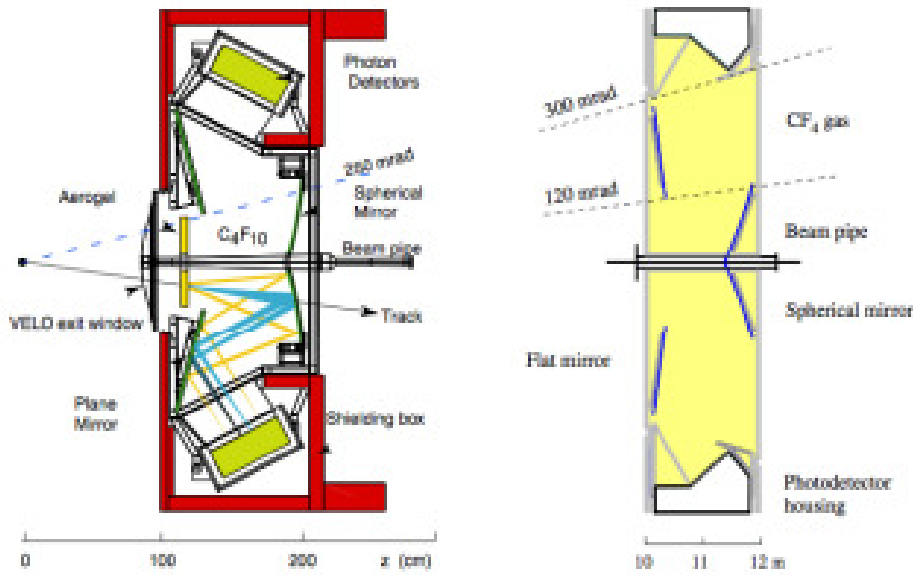


Figure 3.12: Side representation of RICH 1 and RICH 2.

radiation, by photomultipliers, allows the determination of the total energy of the incident particle.

The calorimeter system consists of an electromagnetic calorimeter (ECAL) and a Hadron Calorimeter (HCAL). The ECAL consists of 6016 cells of different sizes, designed to have an energy resolution of

$$\frac{\sigma_E}{E} = \frac{(8 \pm 10)\%}{\sqrt{E(\text{GeV})}} + 0.9\% \quad (3-4)$$

and it is preceded by two planes of scintillating plaques, or Scintillating Detector (SPD- Scintillating Pad Detector) and Pre-Shower (PS Pre-Shower). SPD provides the separation between neutral and charged particles and the PS contributes to the identification of the electromagnetic shower. In all four subdetectors the light produced by the scintillator is captured by wavelength displacer fibers and transported to the photomultipliers. The HCAL is a calorimeter composed of iron plaques and scintillators of 16 mm and 4 mm respectively, this information is read by the 1488 wavelength displacer cells, and has a resolution of

$$\frac{\sigma_E}{E} = \frac{(69 \pm 5)\%}{\sqrt{E(\text{GeV})}} + (9 \pm 2)\% \quad (3-5)$$

### 3.4.3 Muon System

The muon system [35] (Figure 3.13) for semi-leptonic decays of heavy hadrons is a fundamental tool for determining the flavor of the produced quark, which makes this system crucial for LHCb trigger and offline reconstruction.

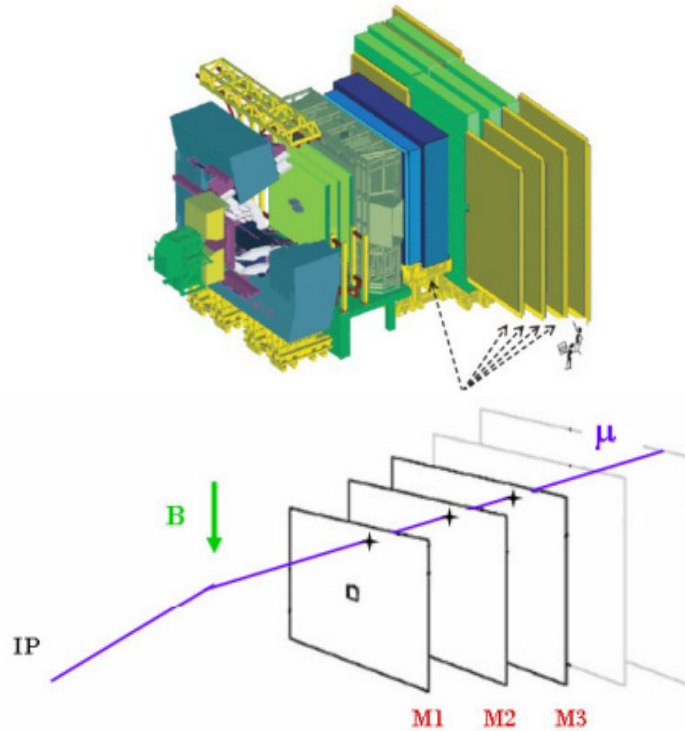


Figure 3.13: Muon system of the LHCb. Left: scaled drawing the muon system location. Right: Trajectory of a muon from the interaction point until cross the 5 track stations.

From the particles that interact with the detector, muons are those having more penetration power. This system has the role of determining the trajectory of muons, linking up with the initial trigger in search of muons with high transverse momentum, as explained in the following sections.

It consists of five muon tracker stations (M1-M5) disposed along the beam axis, interspersed with filters (steel walls) for eventual attenuation of survival hadrons, electrons and photons. M1 is situated before the calorimeters and the other stations are located at the end of the detector, separated by 80 cm steel walls that prevents the passage of other particles.

Each of the 5 stations is divided into four regions R1-R4 and comprises muons chambers of different types, sizes and granularities. Each region is divided into cells that determine the position of the passage of the muon. In M1R1 Gaseous Electron Multiplier (GEM) detectors are used, consisting of a thin perforated metal sheet with a high hole density. Applying a high

potential difference creates electric fields in the holes that collect electrons produced in the gas ionization. The additional M1 regions, along with all the other stations are composed of proportional chambers Multi-Wire Proportional Chambers (MWPC) based on the principle of ionization of a gas by the passage of particles. The ions created by the passage of particles migrate to the electrodes with opposite polarity, causing a small current that can be amplified and measured, thus identifying the position of the muon.

### 3.5 Trigger System

Each intersection of the LHC beams corresponds to approximately 40 MHz (event rate) data, which means an average frequency of 10 MHz visible data on the LHCb detector. This amount of information is too large to be read and stored in the long term in disks. Moreover, most of this information is not of interest to the purposes of study because the cross section of  $q\bar{q}$  pair production, compared to the inelastic cross section of  $pp$  collision shows that a small number of collisions generate interesting events to the LHCb study objectives. The trigger system makes the quick decision if an event should be discarded or recorded. Through a sophisticated system [36] it filters the data in real time with the aim to reduce the output rate written to disk at around 2 kHz. This reduction is achieved by two levels of trigger: The trigger Level-0 (L0), based on hardware components, and High Level Trigger (HLT), based in software lines.

#### 3.5.1 L0 Trigger

It is a trigger based on the LHCb hardware components [37] which reduces the initial rate of 10 MHz of visible collisions to 1 MHz. It combines information from the muon chamber, the electromagnetic and hadron calorimeters and SPD detector. It takes advantage of the fact that the heavy flavor hadrons, due to their large masses, decay in particles with transverse momentums ( $P_T$ ) relatively large, to trigger events (with lepton, hadron or photon). This information is sent to the L0 Decision Unit (L0DU) which also receives as input the estimated number of interactions from the storage unit. The L0DU performs a simple arithmetic calculation with the contributions received and issues a decision for the different types of trigger: muon, dimuon, hadron, electron and  $\pi^0$ , and this decision is made on  $4 \mu\text{s}$  while the decision time of reconstruction algorithms in the calorimeter and the muon detector is  $1 \mu\text{s}$ .

### 3.5.2

#### High Level Trigger HLT

The LHCb experiment uses a series of servers to filter the received events from the detector. This is a complex task because the decision must be made very quickly and reliably. The High Level Trigger (HLT) is the second (and last) level of trigger of LHCb, running on events passing the  $L0$  trigger.

##### HLT1 High Level Trigger 1

Once accepted the event by  $L0$ , the HLT1 reconstructs tracks in 2D at VELO and measures the momentum in T stations.

##### HLT2 High Level Trigger 2

It consists of a chain of inclusive trigger lines, so-called topological lines, allowing to determine particular decay channels, fully reconstructs individual channels, and finally writes the data to tape.

After the HLT2, the data contains mostly events of physical interest; each HLT1 and HLT2 selection produces summary information for accepted events, which are written in the storage units.

### 3.6

#### Online Selection System

The task of the online selection system is to ensure the transfer of data from electronic devices in the detector until the permanent storage under known and controlled conditions.

The LHCb Online System architecture consists of three components (see Figure 3.14):

##### DAQ Data Acquisition System.

Its purpose is to carry the data belonging to the intersection of a given group and identified by the trigger, from the electronic devices in the detector until the permanent storage.

##### TFC Timing and Fast Control system.

Leads all stages of data read from the LHCb detector between electronic devices and the online processing, by the beam synchronization clock, the  $L0$  trigger and the synchrony reset and speed control commands.

##### ECS Experimental Control System.

Ensures control and monitoring of the operational status of the entire LHCb detector. This covers not only the traditional areas of control

detector, such as high and low voltages, temperatures, gas flows and pressures, but also the control and monitoring of trigger systems, TFC and DAQ.

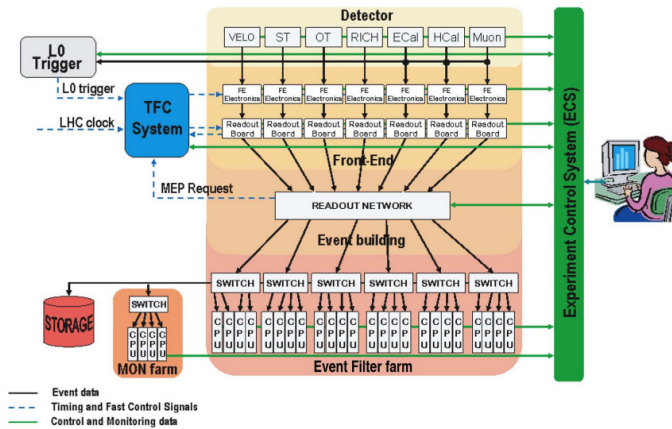


Figure 3.14: Architecture of the Online Selection System of the LHCb with its three components: DAQ, TFC and ECS.

### 3.7 LHCb Software Framework

All the LHCb software environment is based upon the full Object Oriented GAUDI framework [38]. The analysis, performed into the GAUDI architecture, can be splitted in problems involving only a single proton collision that is considered independent from the previous and the next one except for effects due to dead-times, treated statistically. Because of the non mixing events procedure, the workload can be easily split on many computing nodes in exactly the same way for all the purposes.

The main LHCb software tools are:

**Gauss** Both the event generation and detector simulation are handled by Gauss [39]. A tuned version of Pythia [40] is used to generate the pp interactions, while the decays of the particles is described by the EvtGen package [41]. The Geant4 toolkit [42] simulates the interaction of particles in the detector. To save time and increase the production efficiency, selected cuts can be applied at the generator level.

**Boole** The BOOLE software package [43] is in charge of simulating each sub-detector response. It recreates the digitization of the energy deposited in

the LHCb detector active material. At this stage, the hardware trigger (L0) is also emulated. The output format of `BOOLE` is exactly that used in real raw data files, allowing the following software chain to be the same for MC and real data.

**Moore** The HLT 1 and HLT 2 are software triggers which are implemented by the `MOORE` package [44] for both the online system and offline simulated events. The trigger settings are defined via an unique hexadecimal word called Trigger Configuration Key (TCK) that identifies the set of trigger decisions (e.g. trigger algorithms run in L0, in HLT1 and in HLT2, the selection criteria, etc.). To ensure a correct reproduction of the trigger performance in the simulated events, each TCK must be processed with a specific version of the `MOORE` software (exactly the same that has been run when the real data was taken).

**Brunel** Brunel [45] is the reconstruction program that creates physics object starting from raw detector hits. The physics objects consist of charged tracks, photons, calorimeter clusters and Cherenkov rings. Also informations about the tracks are obtained, such as PID likelihoods and track quality.

**DaVinci** The last reconstruction step is DaVinci [46]. With this program it is possible to create composed objects and to perform candidate selection. Selected candidates can be stored in different file formats useful for statistical analyses (e.g. histograms or ntuples) or visualization (using the Panoramix software package [47]). DaVinci is also used for the selection procedure, in which case an output format readable by DaVinci itself is used.

### 3.8

#### Summary

In short, the LHCb has been described from its location in the LHC tunnel to its main components including the detector and its interface with the machine, and the first level hardware-based trigger, the high level trigger based on software components, and the online monitoring system.

With the above in mind, we can say that we have a high level of confidence in the data obtained in each run, hoping to get interesting results studying the physics of heavy flavors sector, search for new physics effects through high-precision measurements of CP violation and rare decays in the sector of  $b$  and  $c$  physics and possibly reach beyond what other experiments allowed, in the knowledge of the fundamental processes of particle physics.

## Data Analysis

The first demand to face in a data analysis is the enhancement of the sensitivity on the observables of interest: an optimized selection that reduces the number of background events must be found. This Chapter is dedicated to describe the logical course in data treatment and the techniques used in the present analysis in order to get our final sample.

In this thesis, the data used for our decay channel corresponds to part of Run I with an integrated luminosity of  $2.0 \text{ fb}^{-1}$  and a center-of-mass energy of  $\sqrt{s} = 8 \text{ TeV}$  [48] for proton-proton collisions taken during 2012. The information provided by the LHCb detectors is combined to reconstruct events. Most of the events, however, are not of our interest. Therefore, some criteria are necessary to enrich the data sample with events containing true  $D^+ \rightarrow \pi^- \pi^+ \pi^+$  decays.

We work with data that has been taken with both magnet orientations or polarities, namely MagUp and MagDown. A breakdown of the data sample is given in Table 4.1.

Table 4.1: Luminosity corresponding to the data sample used in this analysis.

	Stripping20
Magnet Up	$1.000 \pm 0.012 \text{ pb}^{-1}$
Magnet Down	$0.988 \pm 0.012 \text{ pb}^{-1}$

The analysis to select our final sample of  $D^+ \rightarrow \pi^- \pi^+ \pi^+$  (charge conjugate implicit) proceeds through the following steps:

1. *Trigger selection:*

In order to be stored and processed offline, the collected data are filtered at the L0 and the HLT trigger levels by specific trigger lines. Each event that passes the selection can be classified as TOS (Trigger On Signal) or TIS (Trigger Independent of Signal). We call TOS events, with respect to a given trigger implementation, those events for which our decay of interest is responsible for the whole event to be kept. TIS events are triggered due to decays of particles from other part of the event, independent of our signal. In this analysis, specific trigger lines for TOS or TIS events are required at each trigger level, in order to facilitate the understanding of the trigger efficiency.

## 2. *Offline pre-selection (stripping).*

This process, described in Section 4.2, consists of combining the reconstructed particles to form signal candidates responding to specific requirements mainly related to the decay's kinematic. Stored events are reconstructed by the BRUNEL application [45], which converts hits and calorimeter depositions into tracks and particles. The reconstructed events are then further filtered in a process called stripping, which uses the analysis tools contained in the DAVINCI<sup>1</sup> application [46], such as particle identification algorithms and vertex fitting functions, to reduce the data sample. Different stripping lines are used, each of them optimized for a defined decay topology. One specific stripping line for the exclusive selection of  $D$  candidates is used for the analysis: the `StrippingD2hhh_PPPLine`, for decays with three charged pions in the final state. In this case the pion mass is assigned to all the particles that are combined into the final decay chain. A detailed list of the criteria defining this stripping line is given in Section 4.2.

## 3. *Offline selection.*

A cut-based selection is applied to the reconstructed candidates, in order to get rid of those events which are most easily identifiable as background and improve the signal significance. The value of the applied cuts maximises a defined figure of merit or must be highly efficient on signal, in order not to lose precious events, but at the same time they provide significant background suppression.

## 4. *MVA: Multivariate Analysis (see Section 4.5.2)*

It is applied as a finer selection. This algorithm combines a set of discriminating variables, chosen conveniently by the user, in order to build a new variable which provides an optimal signal-background discrimination. Cutting on this variable could then provide both high signal efficiency and background rejection.

In the next section, some variables relevant to the study are defined, previous to enter the different stages of the selection.

<sup>1</sup>Physics analysis software for the LHCb experiment.

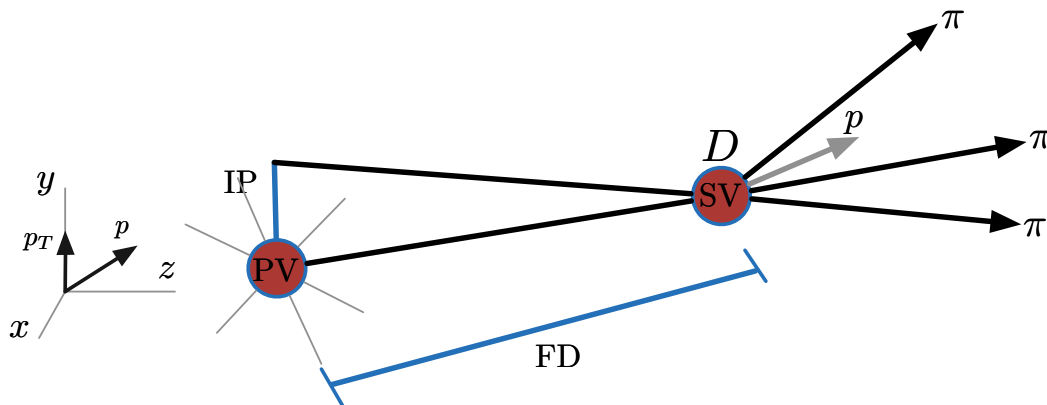


Figure 4.1: Topology of the production process of the  $D$  meson and its decay  $D^+ \rightarrow \pi^- \pi^+ \pi^+$ .

#### 4.1 Main Variables For Sample Selection

Variables involved in the optimization are: kinematic variables of the particles associated with the decay (such as momentum ( $p$ ), transverse momentum ( $p_T$ ), and energy ( $E_T$ )). Particle Identification (PID) variables (based on the information provided by RICH detectors, muon system, and calorimeters) and Topological variables: events are accepted or rejected according to the value of some variables directly related to the topology of the decay.

Following we explain the characteristics of some of the variables involved in the optimization used in accordance with the topology of the decay shown in Figure 4.1:

**D\_MM** *Invariant mass of the  $D$  candidate.*

It is obtained from information of the 4-momenta of each daughter particle. Its value is required to be close to the nominal mass of  $D$ .

**D\_PT** *Transverse moment of  $D$  candidate.*

It is the modulus of transverse momentum of the  $D$  candidate with respect to the beam direction ( $z$ ).

**PV** Primary Vertex (PV)

It is the point where the  $p-p$  interaction occurs and where the  $D$  meson is produced.

**SV** Secondary Vertex (SV)

It is the point where the  $D$  meson candidate decays in its products (daughters).

$\chi_{FD}^2$  Flight distance  $\chi^2$  of  $D$  related to its own primary vertex.

It is the square of distance between the PV and the SV, in other words, the distance between the collision point (where  $D$  is created) and the decay point, divided by the square of its uncertainty.

**D**  $\chi_{IP}^2$  a  $\chi^2$  difference of PV related to Impact Parameter.

This is the difference in the  $\chi^2$  of the PV fit with and without the  $D$  candidate particle. If the particle comes from the primary vertex (which is the case for a true  $D$ ) this difference should be very small.

**pi**  $\chi_{IP}^2$  ( $i = 1, 2, 3$ ) It is the same quantity as that for the  $D$ , but now for each  $i$  daughter. Since none of them should come from the PV, this quantity must be large for true  $D$  daughters.

**DIRA** Direction angle.

Cosine of the angle between the  $D$  displacement vector (obtained from the 3D PV and SV location) and the reconstructed moment of  $D$  meson from the three daughters. For real three body  $D$  decays, it must be close to 1.

**pi\_PT** ( $i = 1, 2, 3$ ) Transverse moment of the daughters.

The  $D$  meson is generally produced with large transverse momentum, and this feature is inherited by its daughters, so **pi\_PT** is a good discriminant of signal/background. However, the low  $PT$  region is located on the edges of the Dalitz plot, thus implementing a strong cut in any of these variables introduces undesirable sculpting of the Dalitz plot acceptance.

**DOCA\_ij** Distance of minimum approach between the tracks  $i$  and  $j$ .

Given the two daughters, it is the minimum distance between their reconstructed trajectories.

**$\Delta \ln \mathcal{L}_{K\pi}$**  Particle Identification

From the quality of identification of the daughter particles it depends the confidence in the  $D$  meson candidates selection. In our case we need to identify in the best possible way pions and kaons.

From the RICH information, for each track it is associated a probability to be one of the five possible particles: pion, kaon, proton, electron or

muon. We use the likelihood hypothesis of the particles, and calculate the logarithmic difference of these amounts. For  $K\pi$  separation one uses the expression  $\ln\mathcal{L}(K) - \ln\mathcal{L}(\pi) = \ln\mathcal{L}(K - \pi)$ .

$\chi^2/\mathbf{ndof}$   $\chi^2$  per degree of freedom of the track reconstruction fit.

It is the  $\chi^2$  of the track reconstruction fit divided by the number of degrees of freedom.

**PTsum** Scalar  $p_T$  sum of the three daughters.

As  $D$  is a particle with high PT, the produced particles will also have high PT values. PTsum it is defined as the scalar sum of the three daughters PT.

**logIP** The logarithm of the ratio between the product of all daughter's  $\chi_{IP}^2$  and the  $\chi_{IP}^2$  of the  $D$ ,

$$\log IP = \log\left(\frac{\prod_i \chi_{IP\pi_i}^2}{\chi_{IPD}^2}\right)$$

## 4.2

### Stripping Selection

The data collected online by the trigger (see Section 4.3) passes through an off-line selection system known as *stripping*, which is a unified selection process for data to be permanently stored in the LHCb and further cleaned in an ‘off-line’ mode in order to get rid of those events that can be identified as background and improve the signal significance. This off-line process provides the data that will be permanently saved in the LHCb.

Among the basic criteria for event selection at this stage are the quality of tracks, good vertex definition and an excellent identification of particles. The relevant variables are briefly described in Section 4.1. In 2012, the stripping cuts for selection of the LHCb data is called as **Stripping20** and for our decay under study,  $D^+ \rightarrow \pi^- \pi^+ \pi^+$ , it is defined by a line called **StrippingDhhh\_PPPLine**. Table 4.3 shows a full description of the stripping selections.

Variable	Cuts
Daughter cuts	
$p_T$	$> 250 \text{ MeV}/c$
$p$	$> 2000 \text{ MeV}/c$
$p_T$ sum	$> 2800 \text{ MeV}/c$
pi $\chi_{IP}^2$	$> 6$
$\Delta \log \mathcal{L}_{K\pi}$	$< 3$
Mother cuts	
$\chi^2$ vtx	$< 30$
$Dp_T$	$> 1000 \text{ MeV}/c$
Mass	$1800 \text{ MeV}/c^2 < m_D < 2040 \text{ MeV}/c^2$
$\chi_{FD}^2$	$> 125$
D $\chi_{IP}^2$	$> 12$
DIRA	$> 0.98$
DOCA max	$< 0.5 \text{ mm}$

Table 4.2: Stripping20: Off-line selection criteria for the LHCb data in Run II (2012) for candidates of  $D^+ \rightarrow \pi^- \pi^+ \pi^+$ .

### 4.3

#### Trigger Selection

The data collected in the LHCb experiment is initially filtered by the L0 and HLT trigger levels (see Section 3.5) by different selection criteria known as trigger lines. At this stage the data selection occurs ‘on-line’. The events can be labeled of TOS (Trigger On Signal) if they are triggered by associating the information of the detector and the candidate signal itself or TIS (Trigger Independent of Signal) if they are triggered without the requirement to be associated to the candidate signal.

At the L0 level, the candidates for the decay channel studied here are required to be TOS in the trigger lines `D_LOHadronDecision` (meaning that one of our pion daughters was responsible for firing the trigger) or a combination of L0 TIS line, as shown in Table 4.3.

The reconstruction of tracks is performed at the HLT1 level with a three-dimensional pattern recognition using the information provided by the VELO detector and the tracking systems OT and IT. In this analysis, we use a particular HLT1 trigger line that guarantees at least one of our daughter with high  $p_T$  and  $\chi_{IP}^2$ ; this is the line `D_Hlt1TrackAllL0Decision`. Finally, the events corresponding to charm decays in three hadrons are obtained by requiring our  $D$  candidate to be TOS by the line `D_Hlt2ChamHadD2HHHDecision` at HLT2. Table 4.3 shows the trigger selection used in our decay channel studied.

At this stage we apply a muon veto to all three tracks, in order to control the contamination from semileptonic decays. Figure 4.2 shows the mass spectrum for  $D^+$  candidates decaying in three pions,  $M(\pi^- \pi^+ \pi^+)$ , after the trigger and stripping selections are applied. Additional cuts are, however, necessary as discussed in the following section.

Trigger level	Condition required
L0	<code>D_LOHadronDecision_TOS</code> or <code>D_LOHadronDecision_TIS</code> or <code>D_LOMuonDecision_TIS</code> or <code>D_LOElectronDecision_TIS</code> or <code>D_LOPhotonDecision_TIS</code>
HLT1	<code>D_Hlt1TrackAllL0Decision_TOS</code>
HLT2	<code>D_Hlt2CharmHadD2HHHDecision_TOS</code>

Table 4.3: Trigger selection applied to the  $D$  candidates.

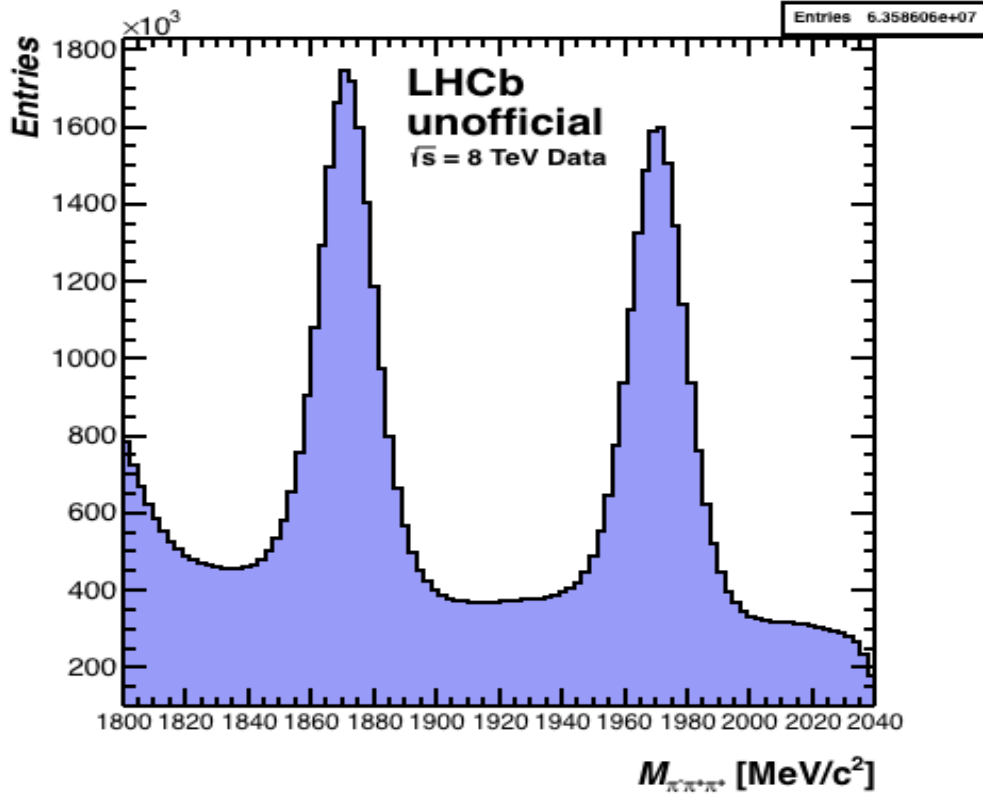


Figure 4.2: Mass spectrum for  $D_{(s)}^+ \rightarrow \pi^- \pi^+ \pi^+$  after stripping and trigger cuts plus a muon veto on all tracks. The invariant-mass  $M(\pi^- \pi^+ \pi^+)$  ranges from 1810 to 1930  $\text{MeV}/c^2$ .

#### 4.4 Monte Carlo (MC) samples

The Monte Carlo simulated samples are used in this analysis to guide the selection criteria and to extract the efficiencies when it cannot be done using the data. All samples were generated in phase space, i.e. with uniform distribution through the Dalitz plot, using the standard LHCb MC 2012 generation procedure, with GAUSS, BRUNEL and DAVINCI, as explained in Section 3.7.

In order to be able to generate large MC samples, we have provided them with generator level cuts and only stored events that passed some dedicated trigger lines. It was generated a total of 18 M events of  $D^+ \rightarrow \pi^- \pi^+ \pi^+$ , half of this data was generated with Magnet Down polarity and the other half with Magnet Up. These samples are passed through a set of processes (e.g. stripping, Hlt1 and Hlt2 filters) with selection criteria similar to data. After this procedure, the total sample consist of 5.5 M events. The samples are not required to pass through Particle Identification criteria ( $\Delta \log \mathcal{L}_{K\pi}$ ), because

these variables are poorly simulated on LHCb MC. Instead, a reweighting process is used, to take into account eventual differences between data and MC, due to Particle Identification variables. This reweighting is a data driven method from calibration samples (better explained in Section 4.7), performed using the PIDCalib tool [49].

After applying in MC all the selection criteria for data (except PID), which will be presented in the following, the MC sample for  $D^+ \rightarrow \pi^- \pi^+ \pi^+$  consists of 129 274 events in a  $2\sigma$  window which we shall define in the Section 4.6.

## 4.5

### Final Selection

In the final stage of the selection a multivariate analysis based in Boosted Decision Trees (BDT) [50] was implemented. Prior to this final stage, rectangular cuts were applied in an initial stage.

#### 4.5.1

##### Study of variables

The aim of the initial selection is to apply loose requirements and reduce backgrounds in the decay channel so that the multivariate selection may be used to reduce them further to implement the final analysis requirements. Since we are interested in charm meson decays in three bodies, the invariant-mass corresponding to the mother particle is calculated based on momenta and masses associated to three possible daughters. From Figure 4.2, for example, we can observe that the peak around 1870 MeV must be formed by candidates corresponding to the expected  $D^+ \rightarrow \pi^- \pi^+ \pi^+$  decay. Other candidates are contributions from the background, both under the peak and in the mass sidebands. These may come from random three-track associations (combinatorial background) or from other  $D$  decays (reflections).

We made a study on the variables of the decay, in order to apply some cuts and also with the objective of find those variables with better signal-background separation power, to give them as input for a neural net to be explained in next section. This study is performed as follows: we plot the variable distribution, with a restriction on the  $D$  mass, i.e. if we want to observe the signal distribution of the variable under study, we restrict it to the  $D$  mass signal region. Logically, to observe its background distribution, the restriction is applied on the sidebands (lateral regions of the nominal  $D$  mass) of the  $D$  candidate. This variable study is twofold, first, we want to observe the variable distribution in order to apply some rectangular cuts, and second,

because we also want to compare the signal and background distributions of the variables of interest, against the distribution of those variables simulated on MC, prior to use them in the next stage of the selection, as shown in next section.

The efficiency of a cut is calculated as the number of events of interest, after applying the cut, divided by the number of events before applying it. The purity for signal ( $s$ ) or background ( $b$ ) is a relation between the number of events of the specie of interest ( $s$  or  $b$ ), and the total number of candidates in the region under study ( $s + b$ ). The number of signal and background are obtained from mass fit. We apply very loose rectangular cuts on some variables, taking into account the distributions of signal and background efficiencies and purities, from Figure 4.3 and Figure 4.4. Those figures show the signal (data and MC) and background distributions of the more relevant variables. The MC distributions are corrected using weights from the PIDcalib package. A summary of the cuts applied is shown in Table 4.4. We do not apply further cuts because we do not have variables considered optimal discriminants, so a multivariate analysis is applied, as explained following.

Table 4.4: Analysis pre-selection requirements prior to BDT training

	Selection variables	Requirements
1	$\log IP$	$> 10$
2	$D \chi_{IP}^2$	$< 9$
3	$\chi_{FD}^2$	$> 250$
4	$\chi_{vtx}^2$	$< 12$

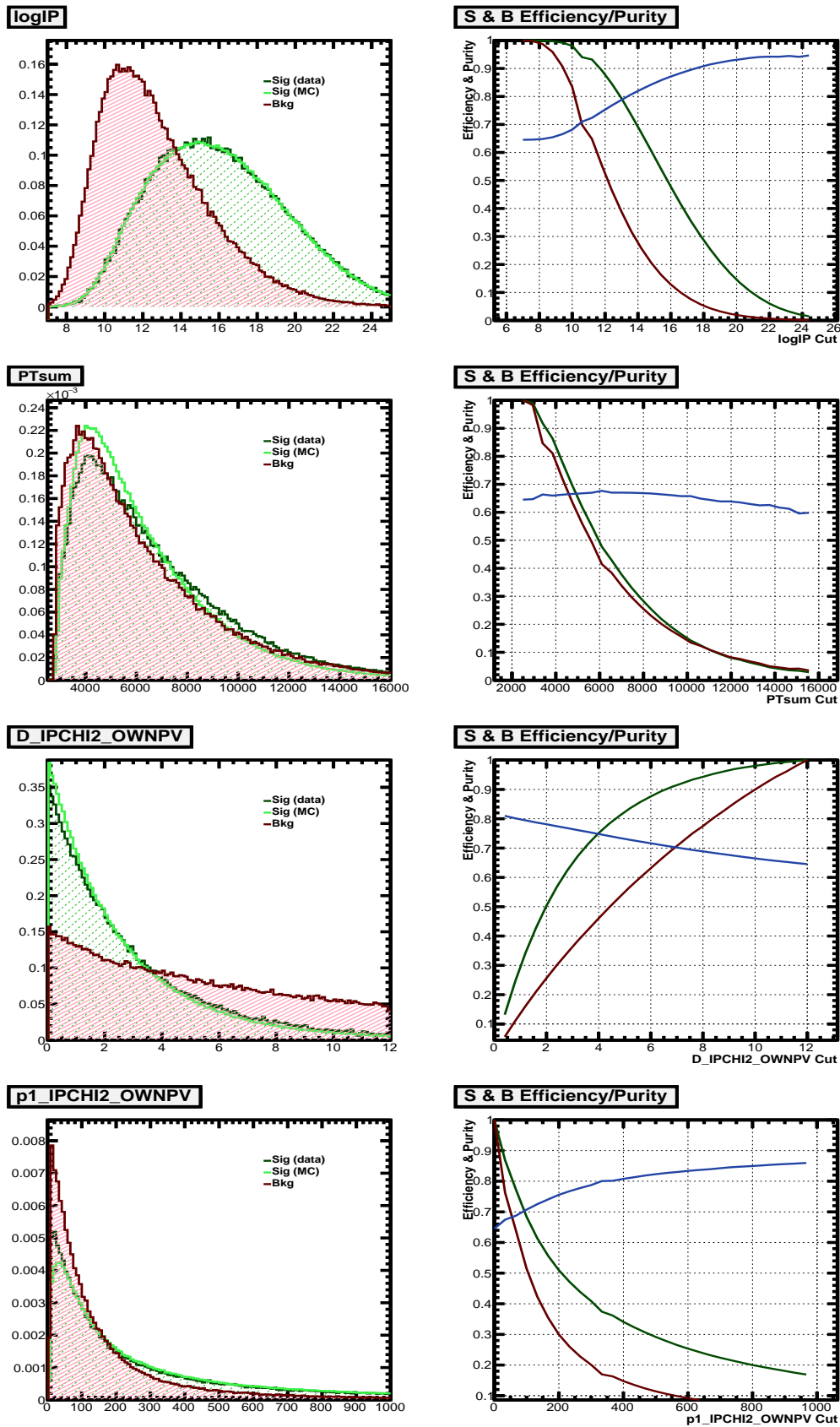


Figure 4.3: Set of variables used in  $D^+ \rightarrow \pi^- \pi^+ \pi^+$  selection. The signal and background efficiency for each cut, as well as the correspondent purity are showed. From this set, only  $\log IP$  and  $D \chi_{IP}^2$  show good signal-background separation, but they do not help to eliminate most of the background.

PUC-Rio - Certificação Digital Nº 1122072/CA

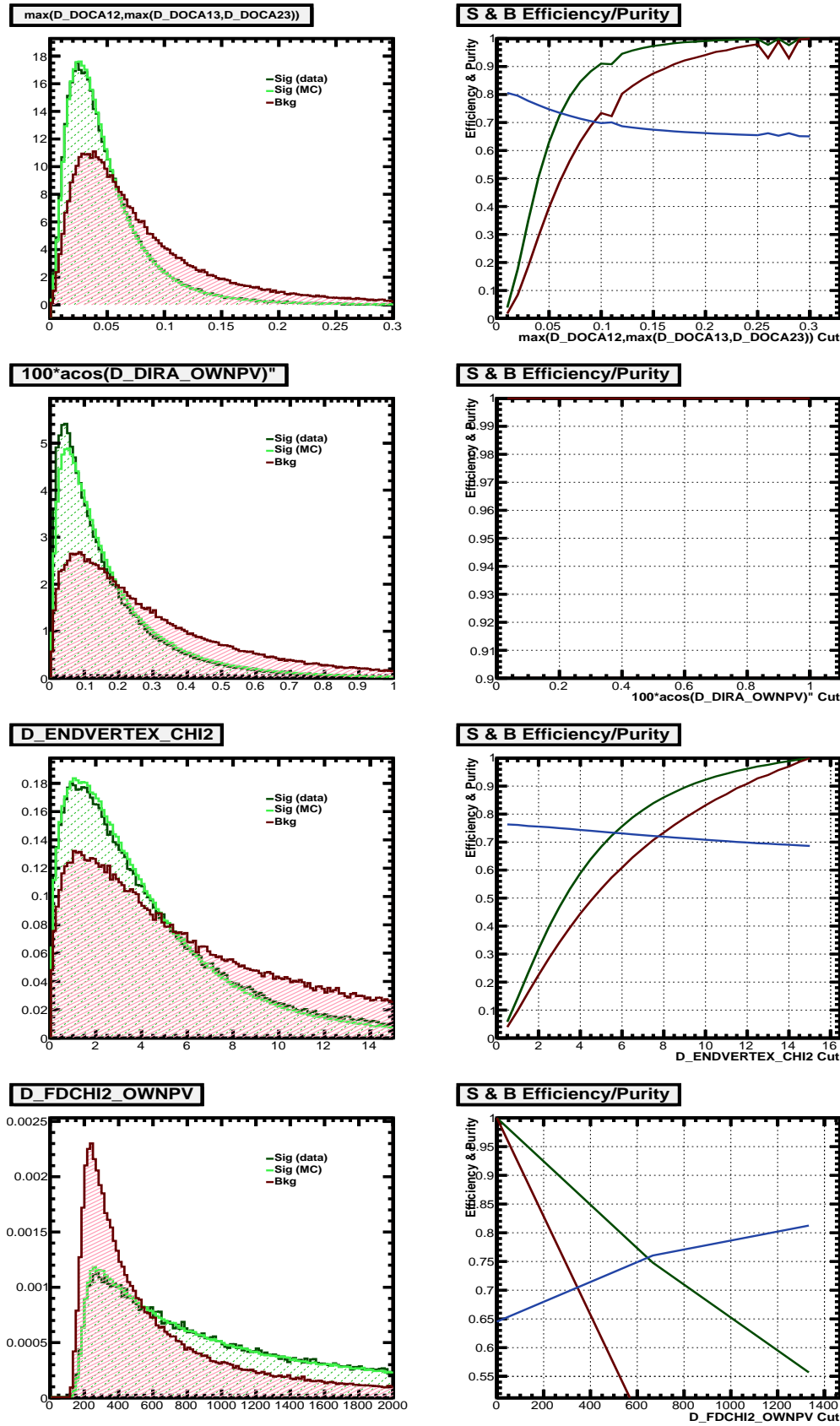


Figure 4.4: Second set of variables used in  $D^+ \rightarrow \pi^- \pi^+ \pi^+$  selection.

### 4.5.2 MVA selection

Once the events were selected, in order to further reject background, events satisfying this pre-selection are then additionally filtered using a multivariate analyzer based on a Boosted Decision Tree (BDT) technique [50]. The decision tree method uses variables (from the analysis) that emphasize the differences between background and signal, allowing a tree to be learned by recursively splitting the initial sample in many subsamples. The splitting is performed according to the value of the considered variable on each step (tree node) that gives the larger discrimination power among signal and background events. Proceeding this way, each event will reach a node and go down one of the two branches depending on the value of the variable represented at the node. After several steps the event will eventually reach a leaf and, once multiple events have gone through those same selection criteria, there will be many events populating that leaf. Each leaf is given a score based on the number of background vs signal events that landed on it. Leaves with a score below 1 (i.e. there are more background events than signal events) are labeled background and leaves with a score over 1 are labeled signal. The output of the decision tree method is known to be highly dependent on the training sample content. To avoid this instability, the so called boosting strategy is used: at the beginning, all events are given equal weights, but once the decision tree has been applied, events landing on leafs labeled as signal are given a weight of 1, while those landing on background leafs get a weight of -1; if an event (during testing) lands on a signal leaf when it is actually background (or vice versa) then its weight is boosted (increased) and a new tree is made with the new weights. This process can be repeated hundreds of times, leading to a highly trained boosted decision tree. The renormalized sum of all of the scores is summed for each event, resulting in all events getting a final score from -1 to 1, meaning unequivocally background or signal, respectively.

The BDT technique involves a “training” procedure to decide whether an event is more likely to be signal or background, based in previously provided signal and background samples. The signal sample is obtained from truth matched<sup>2</sup> MC produced with the 2012 settings. The background sample is obtained from the sidebands of  $D^+ \rightarrow \pi^- \pi^+ \pi^+$  after the initial selection described above, with mass  $1820 < M(\pi^+ \pi^- \pi) < 1830$  MeV/c<sup>2</sup> and  $1910 < M(\pi^+ \pi^- \pi) < 1920$  MeV/c<sup>2</sup>. The BDT uses 11 variables that are chosen because they showed better signal and background separation in training tests. There is

<sup>2</sup>We ensure this by requiring the true ID of the simulated particle to match that of the data.

discrimination power between signal and background in all of these variables. The ranking of the variables from BDT training is shown in Table 4.5.

Table 4.5: Variables used as inputs to train the BDT selection. Variable ranking from BDT training.

Rank	Variable	Variable Importance
1	cosDira	1.565e-01
2	logIP	1.418e-01
3	$\chi_{IP}^2$	1.311e-01
4	$\chi_{vtx}^2$	1.169e-01
5	DocaMax	9.356e-02
6	PTsum	9.182e-02
7	PT <sub>D</sub>	7.893e-02
8	$\chi_{IP_1}^2$	6.738e-02
9	$\chi_{IP_2}^2$	5.435e-02
10	$\chi_{IP_3}^2$	4.886e-02
11	$\chi_{FD}^2$	1.884e-02

The BDT configuration for the training is showed in Table 4.6. After the final application of this multivariate analysis, we chose a cut with value  $> 0.75$  on the BDT classifier, which gives a purity of 97%, as discussed in the next section.

Table 4.6: BDT configuration for the training.

Condition	Value
NTrees	1000
BoostType	Grad
Shrinkage	0.10
UseBaggedBoost	true
GradBaggingFraction	0.5
nCuts	20
MaxDepth	2
IgnoreNegWeightsInTraining	true

In a first stage, the final selection is determined by maximizing the significance ( $\frac{\text{Signal}}{\sqrt{\text{Signal}+\text{Background}}}$ ), where the expected signal and expected background are computed as the numbers of signal, and background events from the pre-selection, in the region  $\pm 2\sigma$  ( $\pm 18$  MeV) from the D mass peak. As maximizing the significance is not a good choice, because of the difficulty to get rid of pionic background, we choose a tighter cut than that given by the optimization. This provides a choice of requiring  $\text{BDT} > 0.75$ .

The results of the BDT training when applied to  $D^+ \rightarrow \pi^- \pi^+ \pi^+$  and data samples are shown in Fig. 4.5. The BDT package transforms the input variables

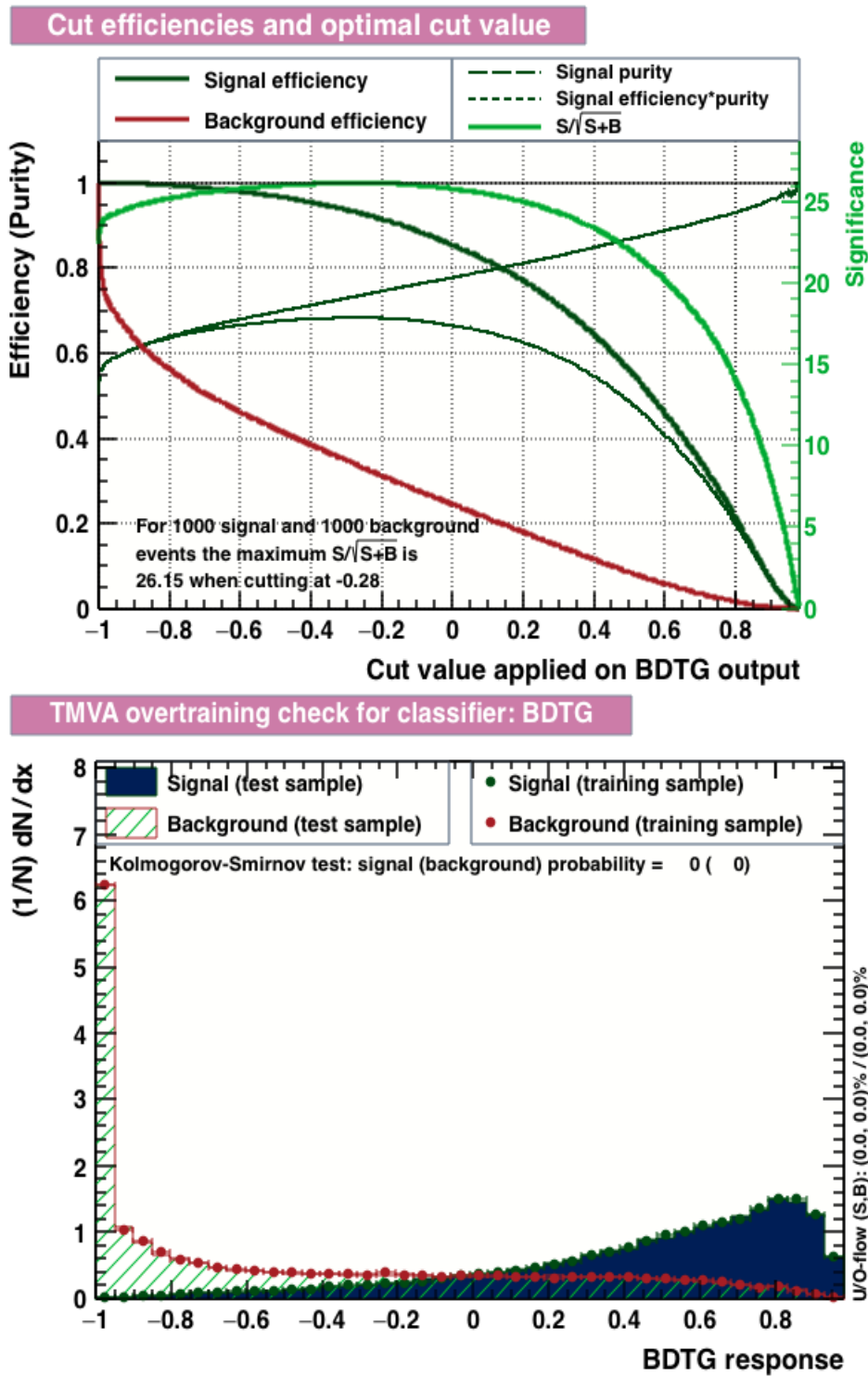


Figure 4.5: Output from training showing the BDT efficiencies (up) and signal and background distributions (down).

into an output variable of signal and background.<sup>3</sup>

<sup>3</sup> In preprocessing, BDT constructs a linear model which decorrelates variables and combines all correlations into single linear combination of variables. This can be transformed to an output which can be interpreted as probability. This transformation has to be monotonic and it can happen that several values of variable transform to the same output, which yields a peak. Whenever the function is flat a peak occurs at the corresponding value.

## 4.6

### Invariant mass fit

A one dimensional fit to the  $D$  candidate mass distribution is used to obtain the yields of the signal and backgrounds, that will subsequently be used in the Dalitz plot fit. The data have been fitted using two Gaussian functions for the signal and the combinatoric background is modeled by an exponential function. In this case, the resulting two Gaussian functions have widths  $\sigma_1$  and  $\sigma_2$ , means  $m_1$  and  $m_2$  and they are weighted by the factors  $f_1$  and  $(1 - f_1)$ , respectively. The resulting fit can be seen in Fig. 4.6, with signal shape parameters shown in Table 4.7.

The signal region is defined as a function of the effective mass and width, as  $m_{eff} \pm 2\sigma_{eff}$ , where  $\sigma_{eff}$  and  $m_{eff}$  are the weighted average of the two fitted Gaussian widths and mean values:

$$m_{eff} = f_1 \cdot m_1 + (1 - f_1) \cdot m_2 \quad (4-1)$$

$$\sigma_{eff} = \sqrt{f_1 \cdot \sigma_1^2 + (1 - f_1) \cdot \sigma_2^2} \quad (4-2)$$

this gives a central mass of  $m_{eff} = 1871.21 \text{ MeV}/c^2$ , a width of  $\sigma_{eff} = 9.04 \text{ MeV}/c^2$  and allows to establish the signal region defined by  $1853.13 < M(\pi^- \pi^+ \pi^+) < 1889.29 \text{ MeV}/c^2$ , which will be the sample used for the Dalitz plot analysis in Chapter 6.

Within the signal region there are  $593\,497 \pm 900$  events corresponding to signal and  $18\,349 \pm 201$  to background with a purity of 97% calculated within the  $2\sigma_{eff}$  mass window. This purity was chosen because, after studying several BDT cuts, trying to maintain the uniformity across the Dalitz, we finally had to prioritize high purity (due to the background complexity), so we must go up to 97% purity. The resulting fit can be seen in Figure 4.6, the Dalitz plot distribution within  $2\sigma_{eff}$  is shown in Fig. 4.7 and the mass sidebands are set as in Table 4.8.

In order to improve the mass resolution a  $D$  mass constraint is applied during the vertex fit [51]. Throughout the analysis we use variables calculated with a  $D$  mass constraint wherever possible. Exceptions arise, for example, when we examine distributions corresponding to  $D$  mass sidebands. The Dalitz plot (DP) coordinates are also calculated under this constraint.

$\sigma_1$	$12.4 \pm 0.2 \text{ MeV}/c^2$
$\sigma_2$	$7.3 \pm 0.1 \text{ MeV}/c^2$
$m_1$	$1870.2 \pm 0.1 \text{ MeV}/c^2$
$m_2$	$1871.6 \pm 0.02 \text{ MeV}/c^2$
$f_1$	$0.28 \pm 0.02$

Table 4.7: Signal shape parameters obtained from unbinned fit to the  $M(\pi^- \pi^+ \pi^+)$  invariant mass with two Gaussian functions.

Region	$M(\pi^- \pi^+ \pi^+)$ MeV/c <sup>2</sup>
Signal	1853.13 – 1889.29
Mass Sidebands	1820.0 – 1830.0 1910.0 – 1920.0

Table 4.8: Signal and sidebands regions

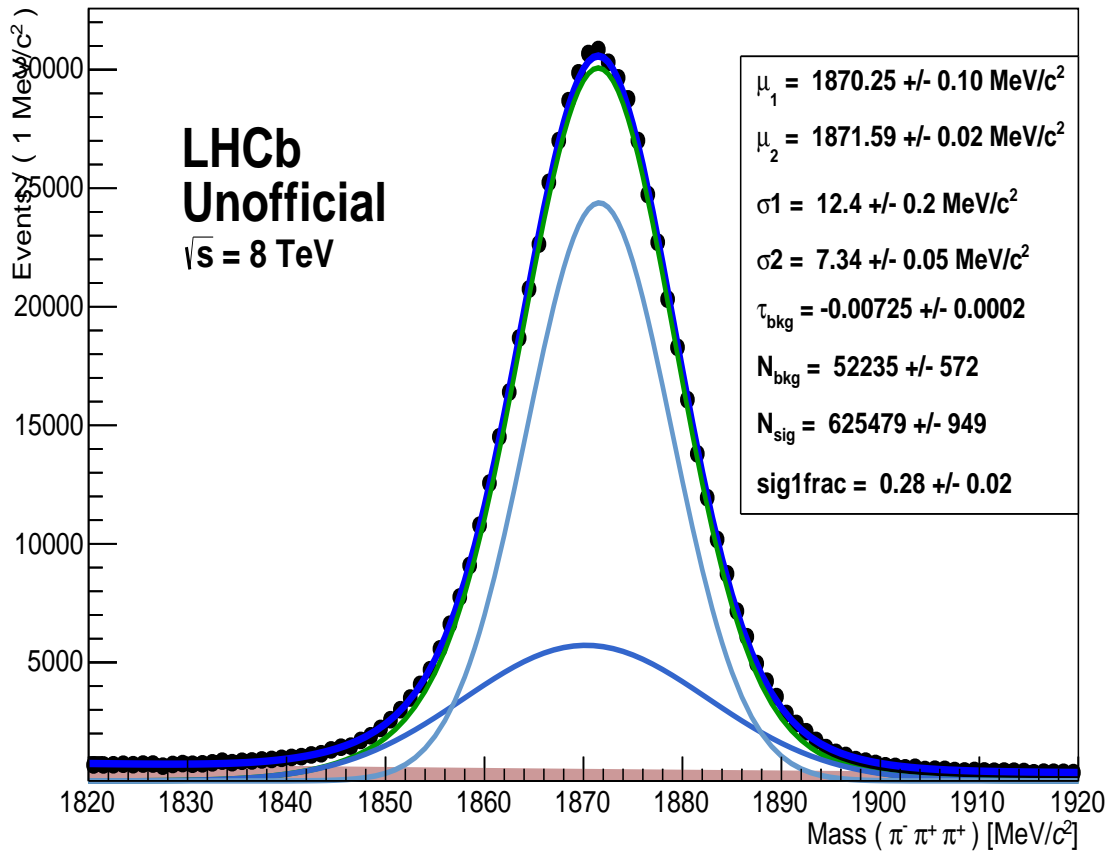


Figure 4.6: Invariant-mass distribution of  $D^+ \rightarrow \pi^- \pi^+ \pi^+$  candidates. The blue line shows the total  $D^+$  pdf, the red line shows the combinatorial background, the green shows the total signal pdf from the two (light blue) Gaussians.

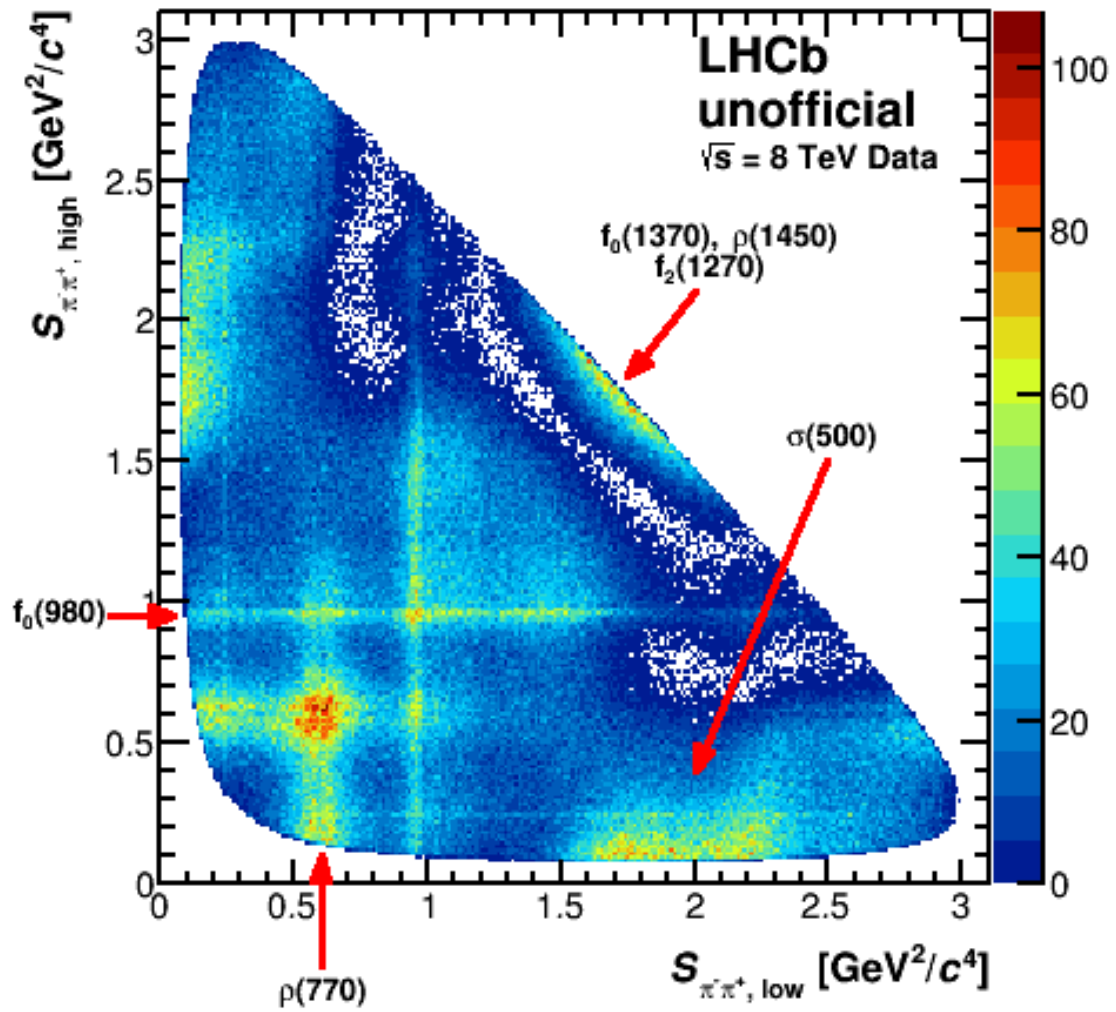


Figure 4.7: The  $\pi^- \pi^+ \pi^+$  Dalitz plot to be used in the Dalitz plot analysis. The more visible resonances are also indicated.

## 4.7

### Signal efficiency variation across the Dalitz plot

As the LHCb detector does not equally select events from regions of the phase space, the fit to data must include the efficiency variation as a function of its position on the Dalitz plot to correct biases introduced by selection, geometry of the detector, trigger and particle identification (PID),

In order to perform the studies the total efficiency is split into contributions for selection and particle identification effects<sup>4</sup>. The total efficiency mode is then calculated as

$$\epsilon^{\text{tot}} = \epsilon^{\text{selection}} \times \epsilon^{\text{PID}}, \quad (4-3)$$

where

- $\epsilon^{\text{selection}}$  is the offline selection efficiency, and determined from MC samples;
- $\epsilon^{\text{PID}}$  is the particle identification efficiency and is determined from data using the `PIDCalib` package tool [52].

The selection efficiency includes the contribution from the offline selection,  $\epsilon^{\text{selection}}$ , is determined from full-simulation MC samples in which we apply the same selection as in data.

The PID efficiency,  $\epsilon^{\text{PID}}$ , is determined from calibration data, reweighed to the signal kinematics and track multiplicity (from MC), using the `PIDCalib` tool. The evaluation of the calibration sample efficiency was performed separately for positive and negative tracks and was also split by magnet polarity. We then use the `PIDCalib` multibody tools with the signal MC samples as the reference for the kinematics (specifically  $p$  and  $p_T$  of the bachelor tracks) and the distribution of `nTracks` sampled from the  $D^+ \rightarrow \pi^- \pi^+ \pi^+$  data. For each signal MC event, the PID efficiency was evaluated by using the appropriate efficiency maps to find the PID efficiency of each bachelor track. The total PID efficiency for a single event is then defined as the product of the two bachelor track efficiencies. This method correctly accounts for the correlation between the kinematics of the two bachelor tracks (expressed in terms of  $p$  and  $p_T$ ) and for the track multiplicity of the event.

The total efficiency is the product of the components shown in Equation 4-3. In order to avoid statistical fluctuations, the resulting histogram is smoothed using a third order polynomial spline function. After the histograms being spline-smoothed the outcome  $\epsilon^{\text{tot}}$  is shown in Figure 4.8, where we use the

<sup>4</sup>We do not include correction for the geometry and trigger effects

so-called **square Dalitz plot**, which is defined by a coordinate transformation to the kinematic variables that maps the Dalitz plot into a rectangle. This transformation avoids the curved edge of bins on the boundary, which simplifies the use of non-parametric PDFs (histograms) to model the distribution of events over the Dalitz plot. The new coordinates are

$$m' = \frac{1}{\pi} \cos^{-1} \left( 2 \frac{m_{12} - m^{min}}{m^{max} - m^{min}} - 1 \right) , \quad (4-4)$$

$$\theta' = \frac{1}{\pi} \theta_{13} , \quad (4-5)$$

$$\theta', m' , \quad 0 \leq \theta', m' \leq 1 , \quad (4-6)$$

where  $\theta_{13}$  is the angle between particles 1 and 3 in the 12 rest frame.

As we have two identical ( $\pi^+ \pi^+$ ) particles in the final state, the Dalitz plot distribution is symmetrical with respect to the line  $s_{12} = s_{13}$ . In this sense, we prefer to use the so-called *folded* Dalitz plot.

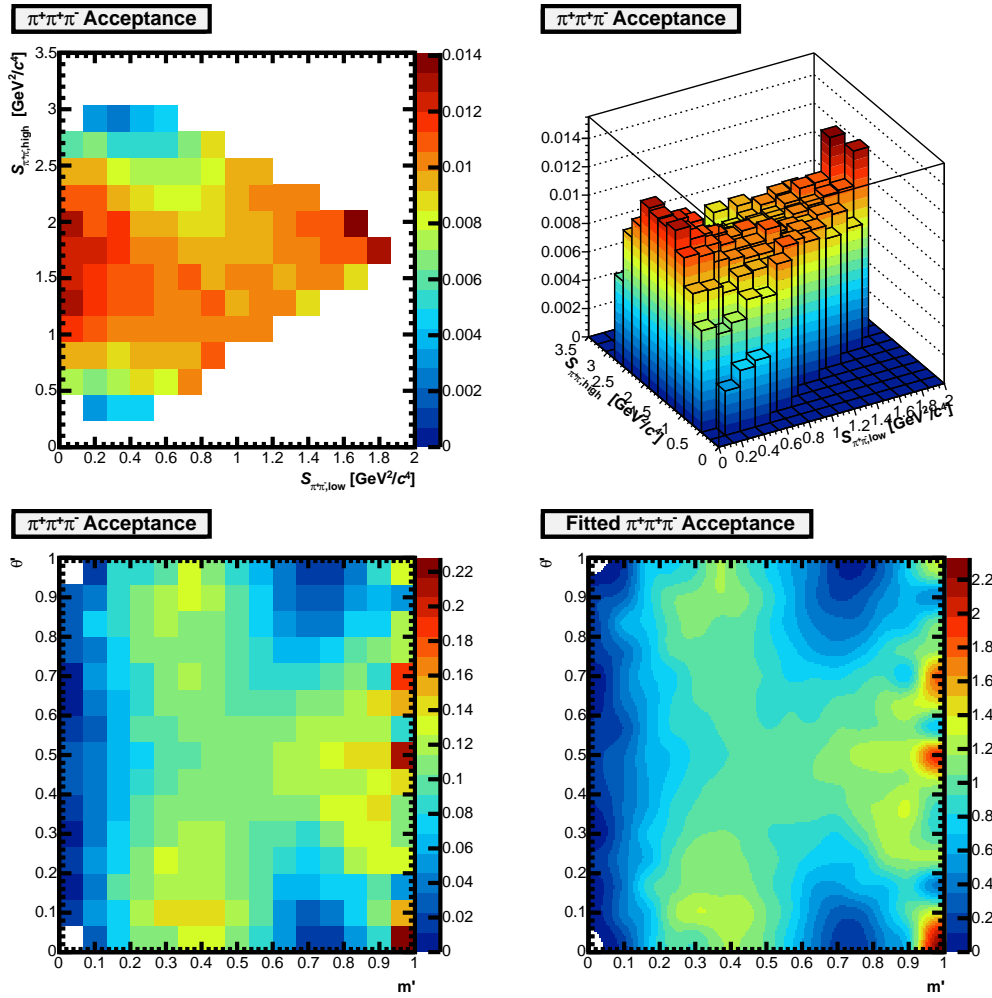


Figure 4.8: (Top) Total efficiency across the  $D^+ \rightarrow \pi^- \pi^+ \pi^+$  Dalitz plot histogram obtained after applying the selection criteria and weighed using the PIDCalib package. (Bottom) the (left) same histogram in squared coordinates and (right) smoothed square DP using a cubic spline function.

## 4.8 Background

As discussed in Section 4.6, we define the sidebands of the  $D^+ \rightarrow \pi^- \pi^+ \pi^+$  decay as being on the intervals  $[1820.0, 1830.0] \text{ MeV}/c^2$  and  $[1910.0, 1920.0] \text{ MeV}/c^2$  respectively. The Figure 4.9 shows the folded Dalitz plot distributions for these mass intervals. We parameterize this sidebands using a cubic spline polynomial function, in order to minimize statistical fluctuations. This result is showed in Figure 4.10.

We also experienced difficulties to get rid of the  $K_s^0$  contribution. As its contribution falls directly within the Dalitz plot, we apply a veto on its mass region:  $[484.8, 505.0] \text{ MeV}/c^2$ . Figure 4.11 shows a data Dalitz plot distribution in which the  $K_s^0$  veto was applied.

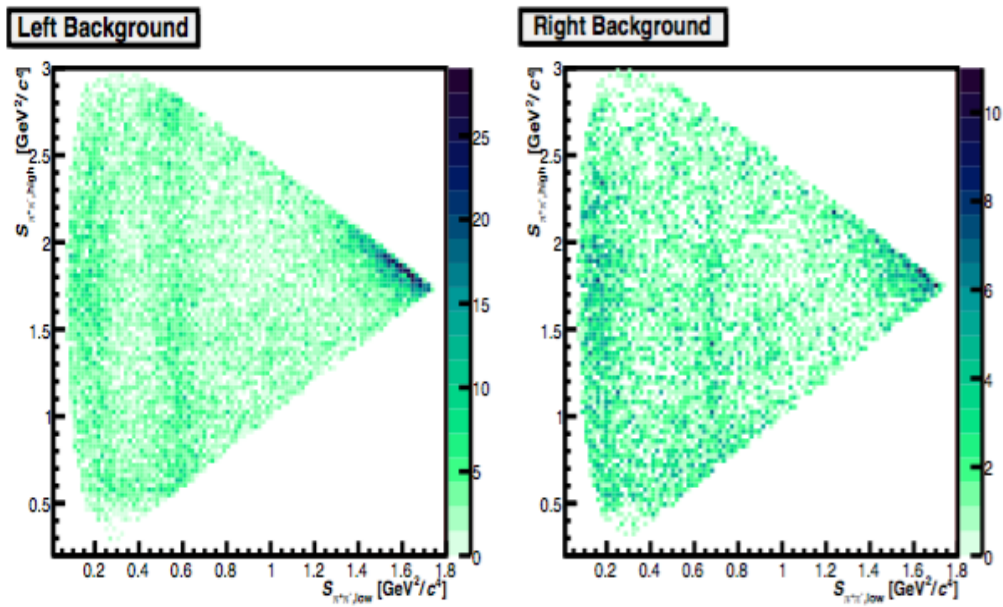


Figure 4.9: Plot of sidebands for the selection with 97% of purity. As seen, is difficult to get rid of the background, even go up to a high purity.

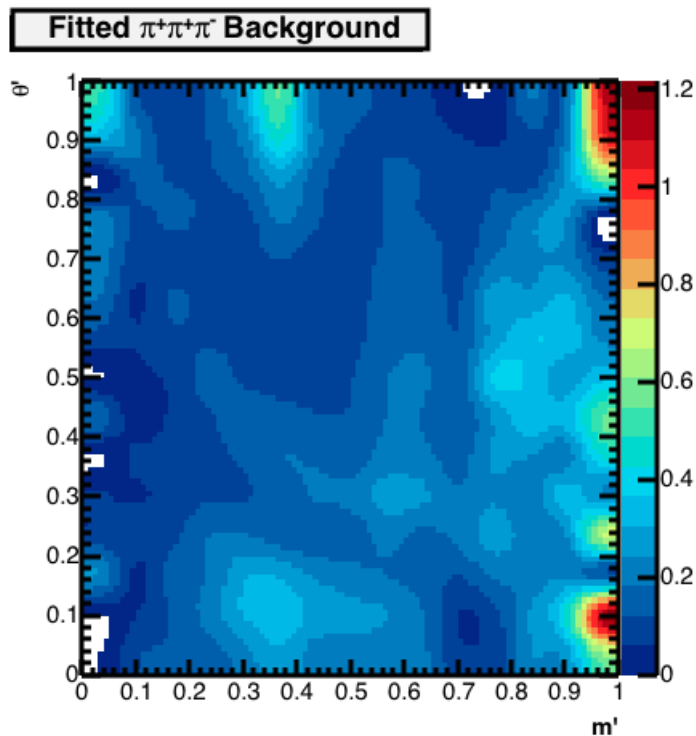


Figure 4.10: Fitted Square DP obtained using spline interpolation for the sidebands regions showed above.

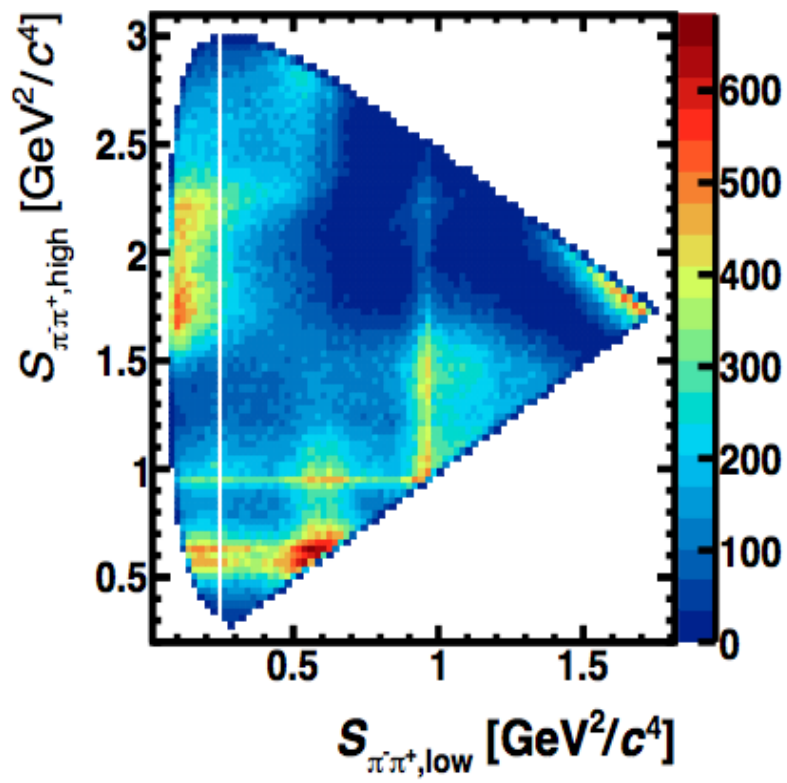


Figure 4.11: Dalitz plot distribution illustrating the veto applied on the  $K_s^0$  mass region.

## 5

### Dalitz plot fitting

In this chapter we present the most common formalism used to represent the  $D^+ \rightarrow \pi^- \pi^+ \pi^+$  decays through its possible resonant amplitudes. We shall also develop the models to be used to perform the fit to data employing the total decay amplitude described in Chapter 2, in order to construct the total probability density function (PDF) which will be minimized by the Maximum Likelihood method within the Dalitz plot fitting program that we use, the `Rio+` [53], developed by members of the LHCb Charm Rio Group (including myself) and used for the first time in LHCb analysis.

Because our data sample, besides containing real decay events, also has a small contamination of background events, and as we have also seen that efficiency effects distort the events distribution on the Dalitz plot, we must be able to build a fit model that takes into consideration all these features.

Considering the above mentioned, the following steps have been taken:

- Define a signal window for the  $D^+$  signal peak to enhance purity. A window of  $\pm 2\sigma_{eff}$  was taken, where  $\sigma_{eff}$  is the effective fitted width of the  $D^+$  peak in Sec. 4.6. This corresponds to  $1853.13 < M(\pi^- \pi^+ \pi^+) < 1889.29$  MeV/ $c^2$ .
- Obtain a histogram of the efficiency variation across the Dalitz plot, evaluated from signal MC events, as described in Sec. 4.7.
- Obtain the Dalitz plot distribution of background events in the  $D$  signal region, described in Sec. 4.6.
- Within the Isobar Model, identify which resonances must be added to the fit model. This is done by including the expected contributions, adding then other possible ones, and eventually removing those which prove not to be significant. Resonance parameters like masses and widths are fitted in some cases.
- A model-independent fit for the  $S$ -wave (MIPWA) is then implemented, where the  $\pi^+ \pi^-$  mass is divided in bins and magnitudes and phases are extracted for this scalar sector.

## 5.1 Signal and Background PDF

The Dalitz plot of the  $D^+ \rightarrow \pi^- \pi^+ \pi^+$  events is represented by a probability density function (PDF) which consists of signal and background probability functions. For the purpose of reference within the fitting package, and considering that the  $\pi^- \pi^+$  resonances lie in the (1,2) and (1,3) system, we choose to define the Dalitz plot in terms of the first two kinematic variables, as in Section 2.2, which from here on we shall designate  $s_{12}$  and  $s_{13}$ , respectively.

We form the Dalitz plot amplitudes using the Isobar Model described in Sec. 2.4.1, which considers the total amplitude as resulting from a sum of amplitudes from the individual decay channels. As we have seen such coherent total amplitude is given by:

$$\mathcal{A}(s_{12}, s_{13}) = a_{NR} e^{i\delta_{NR}} + \sum_i a_i e^{i\delta_i} [\mathcal{A}_i(s_{12}, s_{13}) + \mathcal{A}_i(s_{13}, s_{12})], \quad (5-1)$$

where  $\mathcal{A}_i(s_{12}, s_{13})$  are the dynamical amplitudes described in the Section 2.3 and  $a_i$ ,  $\delta_i$  are the parameters describing, respectively, the relative magnitude and phase of the different decay channels. In Eq. 5-1, the amplitude is explicitly symmetrized with respect to  $s_{12}$  and  $s_{13}$  due to the two identical  $\pi^+$  in the final state. The signal Dalitz-plot probability function, is therefore, in the absence of any reconstruction effects;

$$\mathcal{P}_{\text{sig}}(s_{12}, s_{13}) \sim |\mathcal{A}(s_{12}, s_{13})|^2, \quad (5-2)$$

The total PDF is given by the sum of those signal and background probability functions

$$\mathcal{PDF}(s_{12}, s_{13}) = \frac{\mathcal{P}_{\text{sig}}}{\mathcal{N}_{\text{sig}}}(s_{12}, s_{13}) \times \epsilon(s_{12}, s_{13}) \times f_s + \frac{\mathcal{P}_{\text{bkg}}}{\mathcal{N}_{\text{bkg}}}(m_{12}^2, m_{13}^2) \times (1 - f_s) \quad (5-3)$$

The signal fraction  $f_s$ , obtained from the mass fit and  $\epsilon(s_{12}, s_{13})$  is the acceptance across the DP, That is, the smoothed function obtained in Sec. 4.7 and shown in Fig. 4.8, is the signal purity. The factors  $\mathcal{N}_{\text{sig}}$  and  $\mathcal{N}_{\text{bkg}}$  guarantees that both signal and background PDF's are individually normalized.

We parameterize the combinatorial background using the histogram obtained from sidebands, as shown in Fig. 4.10. By doing so, we suppose that the combinatorial background contributing to the Dalitz plot in the signal region assumes the same form at the sidebands.

## 5.2

### Fitting procedure

To determine the complex amplitudes in a specific model, the data is fitted maximizing the total  $\mathcal{PDF}(s_{12}, s_{13})$  using the unbinned likelihood technique, written as the product on all events, of the fitting function value for each event  $i$

$$\mathcal{L} = \prod_{i=1}^N \mathcal{PDF}(s_{12}, s_{13}|\vec{\alpha}), \quad (5-4)$$

where  $N$  is the total number of candidates, and  $\vec{\alpha}$  represents the set of parameters to be determined by the fit. In the Isobar Model, these parameters are the magnitudes  $a_i$  and phases  $\delta_i$  of each resonance, but it can be extended to include masses and widths of resonances or any other parameter, as needed. In the MI-PWA fit, this set of parameters consists of the magnitudes and phases of the S-wave at each  $m_{\pi^+\pi^-}$  bin edge, along with the  $a_i$  and  $\delta_i$  from spin-1 and spin-2 resonances. The likelihood technique consists in finding the set of parameters  $\vec{\alpha}$  that maximizes  $\mathcal{L}$ , i.e. to find the function that gives the maximum value for all events. To use this technique, we use the ROOT's MINUIT package which minimizes the logarithm of a *fcn* function defined as

$$fcn = -2\ln\mathcal{L} = -2 \sum_{i=1}^N \ln(\mathcal{PDF}(s_{12}, s_{13}|\vec{\alpha})) \quad (5-5)$$

In order to get the fit to a properly convergence in the maximum likelihood method, the total PDF needs to be normalized over the whole Dalitz plot,

$$\int \int_{DP} |\mathcal{PDF}_{s,b}(s_{12}, s_{13})|^2 ds_{12} ds_{13} = 1, \quad (5-6)$$

This is guaranteed by Eq.(5-3), by means of the  $\mathcal{N}_{sig}$  and  $\mathcal{N}_{bkg}$  calculations, accomplished by using Gaus-Legendre integration method [54].

The probability of a certain final state being formed via a particular resonance is what we call decay fraction. Fractions are obtained from the fitted amplitudes, and errors are calculated using the error matrix provided by MINUIT. For a particular resonance  $i$ , the fraction  $f_i$  and its error,  $\delta f_i$ , are given by:

$$f_i = \frac{\int ds_1 ds_2 |A_i|^2}{N_f} = \frac{a_i^2 \cdot N_{ii}}{N_f}, \quad (5-7)$$

$$(\delta f_i)^2 = \sum_{j,k} \frac{\partial f_i}{\partial \alpha_j} \frac{\partial f_i}{\partial \alpha_k} \text{cov}(\alpha_j, \alpha_k) \quad (5-8)$$

where  $N_{ii}$  and  $N_f$  are the resonance  $i$  integral and the total DP integral, respectively, and  $\text{cov}(\alpha_j, \alpha_k)$  is the error matrix. For more details on the fractions calculation see Appendix B.

The unbinned maximum likelihood fit is not extended - just the shape of the Dalitz plot is being fitted. The  $\rho(770)\pi$  channel is chosen as reference, with magnitude  $a_{\rho(770)\pi}$  and phase  $\delta_{\rho(770)\pi}$  set to 1 and 0, respectively.

### 5.3

#### Fitting algorithm consistency test

To have confidence that the parameters found in the fit are being obtained correctly, it is necessary to carry out the fitting algorithm consistency tests, even more as our tool is being used for the first time in Dalitz plot analyses. If a particular model correctly describes the data, the program shall be able to find the optimal parameters. Additionally, being this the first time that the Model Independent Partial Wave Analysis MI-PWA is being implemented on this channel, we also tested this method on toy MC samples. In this way, we present below the test results for both the isobar model and MI-PWA.

#### 5.3.1

##### Isobar model consistency test

The code is validated by fitting ensembles of toy MC samples generated according to the same model and comparing the fit results with the generation parameters. A large number of samples is generated and fitted in order to make a statistically significant comparison. We use for this test a simplified model of the  $D^+ \rightarrow \pi^- \pi^+ \pi^+$  decay, inspired by the best fit obtained by E791, with the central values of table 5.1 as the generation parameters.

Contribution	E791
NR	$7.8 \pm 6.0$
$\rho(770)\pi^+$	$33.6 \pm 3.2$
$f_0(980)\pi^+$	$6.2 \pm 1.3$
$f_2(1270)\pi^+$	$19.4 \pm 2.5$
$f_0(1370)\pi^+$	$2.3 \pm 1.5$
$\rho(1450)\pi^+$	$0.7 \pm 0.7$
$\sigma\pi^+$	$46.3 \pm 9.0$

Table 5.1: Generation parameters of the code validation tests, inspired in the E791 model.

The procedure to make this test is based on the following steps:

- We generated a set of  $N$  samples of toyMC, where the events are obtained according to the total probability function from Equation (5-3).
- We fit each toy MC sample, thereby obtaining a distribution of values for each set of parameters. The average value of each distribution should be compared with the value of the corresponding parameter used in the generation of the samples. Also the standard deviation of each distribution is compared to the error provided by MINUIT.

We made this test generating 1000 samples with 100 000 events each. A histogram for each fitted parameter is filled with fit results and fitted with a Gaussian, as seen in figure 5.1. If the fit is working properly, the fitted parameter distribution is expected to be Gaussian with mean equal to the parameter value used in generation. Also, the Gaussian width is expected to be compatible with the error given by the fitter.

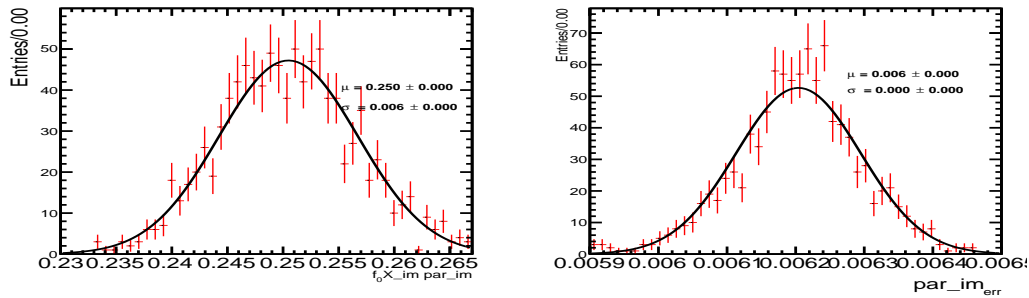


Figure 5.1: Fit results for the imaginary part of the  $f_0(1370)$  resonant coefficient. On the left we see the distribution of fit results for the parameter itself, while on the right we see the error distribution, both fitted by Gaussian functions.

Another validation test was performed by comparing Rio+ with the Laura++ package. In order to obtain the same results we had to modify the definition of our PDF<sup>1</sup> so that it matched that of Laura++. Corrected for these differences, we found that Laura++ and Rio+ fitters are in good agreement, as shown in table 5.3.1 from the fits to a toyMC sample with both packages. Amplitudes are not comparable due to distinct normalization strategies.

Having obtained satisfactory results from the consistency test, we proceeded to test the MI-PWA fitting algorithm.

<sup>1</sup>In Laura++ the Blatt-Weisskopf form factor for the mother (B or D) decay vertex uses the bachelor momentum computed in the resonance frame.

Resonance	Amplitude	Phase	Fraction
<b>Rio+ Fit</b>			
$\rho(770)$	1.00±fixed	0.0±fixed	54.9±2.1
$f_0(980)$	1.56±0.03	-47.0±2.4	20.8±1.3
$f_2(1270)$	0.31±0.01	26.0±5.8	2.3±0.4
$\rho(1450)$	2.09±0.14	74.8±6.6	4.5±1.0
$f_0X$	1.56±0.18	37.7±6.6	2.1±1.0
$\sigma(500)$	3.08±0.10	66.1±1.7	19.1±1.9
<b>Laura++ Fit</b>			
$\rho(770)$	1.00±fixed	0.0±fixed	54.9
$f_0(980)$	0.62±0.01	-46.9±2.4	20.9
$f_2(1270)$	0.21±0.01	25.2±5.9	2.4
$\rho(1450)$	0.29±0.02	74.4±6.8	4.5
$f_0X$	0.20±0.02	37.1±6.7	2.2
$\sigma(500)$	0.59±0.02	66.3±1.7	19.1

### 5.3.2

#### MI-PWA consistency test

In the case of the MI-PWA fit the approach is different, we have many more free parameters, contemplating to have a model independent description of the  $S$ -wave composition. At each fit iteration, a set of  $2n+2$  parameters, for the  $n$  edges of the mass bins, are floated. As the fit is model independent, the  $2n+2$  parameters from the iteration  $i$  are interpolated in the mass bins until obtained the best set of parameters describing the model. This interpolation is done by means of cubic spline functions, which are a special type of piecewise polynomial that depends on its first and second derivatives, calculated at the two edges of each bin, permitting to smooth the shape of the  $S$ -wave in such a way that it can be described by a continuous function. One source of difficulty of this method is the fact that the spline function for the mass interval  $k$ , depends on the boundary conditions (first and second derivatives) of the  $k-1$  and  $k+1$  endpoints, so we may need to define by hand, boundary conditions at the first and last points of the total mass interval i.e. at the points 0 and  $n+1$ . To overcome this, the most general solution is setting to zero the second derivative of those two boundary points.

The consistency test on the fitting algorithm is carried out as follows:

- We construct a model comprised of  $S$ ,  $P$  and  $D$  waves.
- The  $S$ -wave contains the  $\sigma(500)$ ,  $f_0(980)$  and  $f_0X$  resonances, while

$\rho(770)$ ,  $\rho(1540)$  are included in the  $P$ -wave and  $f_2(1270)$  for the  $D$ -wave.

- Using our local toy MC generator included in the Rio+ package, we generate one sample with the above Isobar Model, modeling all resonances with Breit–Wigner propagators.
- For the fit, the  $\pi^+\pi^-$  mass region is divided into  $n$  bins, corresponding to  $n + 1$  endpoints.
- We take the generated parameters (magnitudes and phases) for the  $S$ -wave components and calculate its analytical coefficients at each bin edge to give them as input for the MI-PWA fit.
- We make no assumption about the composition of the  $S$ -wave (the above coefficients are only starting points for the fit).
- The  $S$ -wave parameters are floated, and interpolated at each bin edge with cubic spline polynomial functions.
- The  $P$  and  $D$ -wave resonances are assumed well modeled by the Isobar Model, thus they are parameterized in the fit using Breit–Wigner formulation.
- The total fit is performed, using as reference the  $\rho(770)$  parameters.
- After the minimization, the parameters from  $P$  and  $D$ -wave resonances must be compatibles, and the magnitude and phase distribution of the  $S$ -wave must be similar to the one generated analytically.

To perform this test, we generated one sample with 500 000 events in the Isobar Model form and fit the  $S$ -wave component with the Rio+ fitter package using 40 bins for the MI-PWA. These results are shown in Fig. 5.2. We observe that the MI-PWA fit is in good agreement with the Isobar Generated sample thus we conclude that this tool is working nearly perfectly and it can be used to perform the Model Independent Partial Wave Analysis on real data.

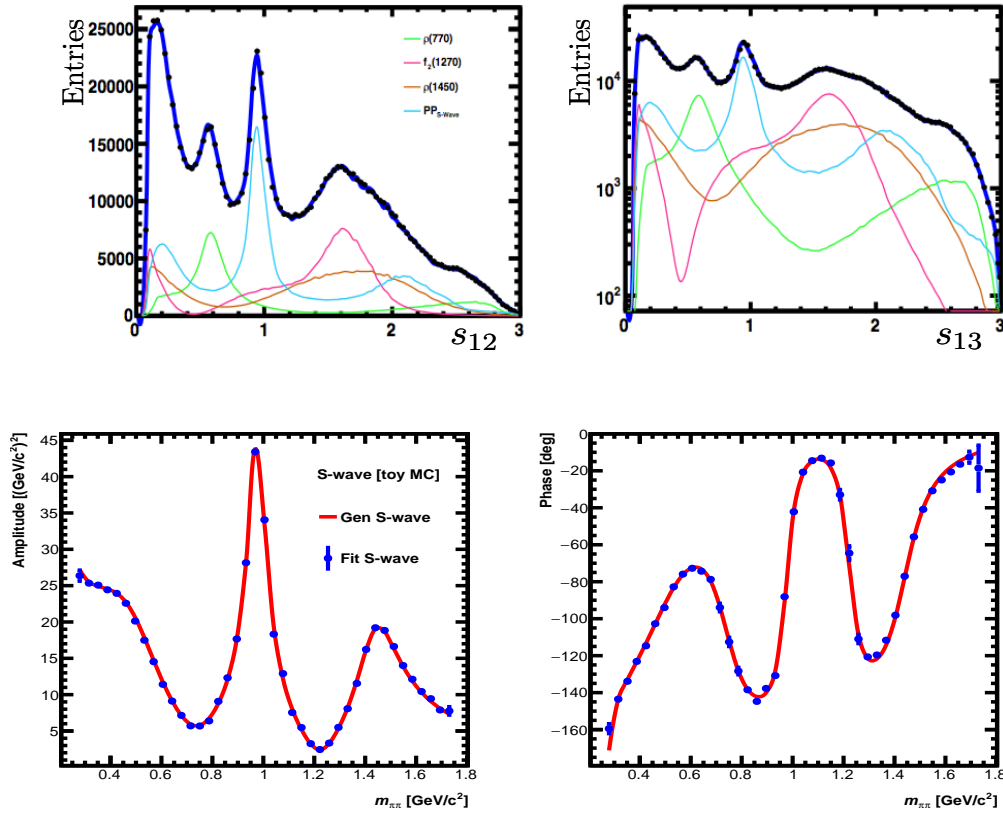


Figure 5.2: Results of the MI-PWA consistency test. Up: comparison of the distribution from the generated toy MC sample (black dots) and the PDF with parameters from fit (blue line). The light color lines represent the lineshapes of the individual contributions. Down: comparison of the generated (red line) and fitted (blue dots)  $S$ -wave. We can see that both the isobar generated sample, and the MI-PWA fit projections are in good agreement and hence we can be confident on the results when this method is applied to data.

### 5.3.3 Quality of Fit

Conducive to quantitatively check the quality of the fit, as well as to compare differences between models, we calculate the fit probability using the p-value (obtained from  $\frac{\sum \chi^2}{\text{ndof}}$ ) as an estimate of the goodness of fit. The  $\chi^2$  is calculated from the differences between observed toy MC generated from the model used and the expected data in each bin of a 2-dimensional histogram<sup>2</sup>:

<sup>2</sup>Although we are using a binned technique to evaluate an unbinned fit, and as it is widely known that there is no complete solution to the problem of Goodness of Fit (GoF) [55] for this case, thus the statement “quantitatively compare” must not be interpreted as a global quantity itself, but as how much the PDF from model- $x_1$ , is likely to describe the data, if compared to model- $x_2$ . The multi-dimensional  $\chi^2$  values are calculated using an adaptive binning scheme to ensure sufficient statistics in each of the bins. Only bins with at least 20 signal events are allowed to split.

$$\chi^2 = \frac{\sum_{i=1}^{N_{\text{bins}}} [(o_i - e_i)^2]}{e_i}, \quad (5-9)$$

$$P = \text{Prob}(\chi^2, \text{ndof})$$

where

- $o_i$  is the observed number of data events in each bin according to the fitted likelihood function.
- $e_i$  is the expected number of events in each bin according to the data distribution.
- $P$  represents the p-value for the given  $\chi^2$  and numbers of degrees of freedom,
- The degrees of freedom are calculated as  $\text{ndof} = N_{\text{bins}} - N_{\text{freeparameters}} - 1$ ,
- $N_{\text{bins}}$  is the number of bins filled with a pre-stated minimum number of events,
- $N_{\text{freeparameters}} - 1$  is the number of free parameters in the fit (the  $-1$  stands because each model is normalized to the observed data events)

We tested uniform and non uniform binning schemes. As generally the fit is better at some regions and worse at other, we used a non uniform binning scheme with 400 bins, aiming to favor those regions more populated of the Dalitz plot.

## 6

### Results

We can now present in this Chapter the main results for both, the Isobar and the Model Independent PWA approaches for the  $D^+ \rightarrow \pi^- \pi^+ \pi^+$  decay. To study the resonant structures of this decay we use 611 846 signal candidates with invariant mass within  $\pm 18.09$  MeV around the  $3\pi$  mass peak which also includes 3% of background. The most relevant results for the Isobar Model are showed first and then we take an acceptable isobar result as input for the  $S$ -wave in the MI-PWA fit. Finally, in order to make an idea on the relevance of the  $\pi^+ \pi^- S$ -wave amplitude, we compare results obtained employing both methods.

#### 6.1

##### Resonance models

Apart from non-resonance (NR), possible resonance candidates in the decay  $D^+ \rightarrow \pi^- \pi^+ \pi^+$  with corresponding variations of the formalism are listed in Table 6.1. We use the Bugg and Flattê line-shapes for the  $\sigma(500)$  and the  $f_0(980)$ , respectively, and the Gounaris-Sakurai formalism for the  $\rho(770)$  and  $\rho(1450)$ . The  $\rho(770) - \omega(782)$  interference is also taken into account. As stated in section 2.4.2, a direct  $\omega \rightarrow \pi^+ \pi^-$  decay is forbidden, but the final state can also be reached via interference with  $\rho(770)$ , so we include in the latter's parameterization the interference coming from  $\omega(782)$ . The values of the meson interaction radii are  $r_R = 1.5 \text{ GeV}^{-1}$  and  $r_D = 5.0 \text{ GeV}^{-1}$  respectively.

Table 6.1: Resonances that are included in the fit to the data sample. Parameters (and uncertainties) are taken from the PDG [56] unless stated otherwise.

$\pi\pi$	state	spin	PDG	Model	
			Mass(MeV)	Width (MeV)	
$f_0(500)$	$(\sigma)$	0	400 - 500 (478)	400 - 700 (324)	Bugg, BW, CP
$\rho(770)$		1	$775.49 \pm 0.34$	$149.1 \pm 0.8$	GS, BW, $\rho - \omega$ interf.
$f_0(980)$		0	$990 \pm 20$ (965)	40 - 100 (70)	Flattê, BW
$f_2(1270)$		2	$1275.1 \pm 1.2$	$185.1^{+2.9}_{-2.4}$	BW
$f_0(1370)$		0	1200-1500 (1434)	200 - 500 (173)	BW
$\rho(1450)$		1	$1465 \pm 25$	$400 \pm 60$	GS BW
$f_0(1500)$		0	$1505 \pm 6$	$109 \pm 7$	BW
$f_2(1525)$		2	$1525 \pm 5$	$73^{+6}_{-5}$	BW

We take the CLEO model as reference, despite the different resonance parameters and the  $\sigma(500)$  parameterization, which they modeled as a complex pole. The nomenclature describing the models gives first the baseline CLEO, model-1, and then “+” for any additions of resonances from Table 6.1, until reach the model- $n$ , for the  $n$ -th one addition or change. The model-1 contains the resonances  $\sigma(500)$ ,  $\rho(770)$ ,  $f_0(980)$ ,  $f_2(1270)$ ,  $f_0(1500)$  and the non-resonance term, NR. If we add  $\rho(1450)$  to this model we obtain model-1 +  $f_0(1500)$  i.e. (model-2) and so on. In model- $(n + 1)$  we start the fit near the local minimum found in model- $n$ .

In initial fits we found the fit in the regions of the  $\sigma(500)$  and  $f_0(1370)$  states to be poor so the masses and widths of these states are also floated, giving rise to model- $x$ , for  $x \geq 4$ .

The nominal fit model includes all of the resonances listed in Table 6.2, modeled as described in section 2.4.1. It uses the isobar model and is an unbinned maximum likelihood fit, performed using the `Rio+` DP fitting package [53], obtaining magnitudes, phases (and masses and widths where applicable) and decaying fractions for every (non-) resonant contribution, taking as reference the  $\rho(770)$  resonance parameters (i.e. with  $a_\rho(770) = 1$ ,  $\delta_\rho(770) = 0$  fixed).

Model	1	2	3	4	5	6
$\rho(770)$	✓	✓	✓	✓	✓	✓
$f_0(980)$	✓	✓	✓	✓	✓	✓
$f_2(1270)$	✓	✓	✓	✓	✓	✓
$\rho(1450)$	✗	✓	✓	✓	✓	✓
$f_0X$	✓	✓	✓	✓	✓	✓
$\sigma(500)$	✓	✓	✓	✓	✓	✓
NR	✗	✗	✓	✓	✓	✓
$f_0(1500)$	✓	✓	✓	✓	✓	✓

✓ : Included, fixed  $m_0, \Gamma_0$

✓ : Included, floating  $m_0, \Gamma_0$

✗ : Not included

Table 6.2: Distribution of the different models used in the fit (the color nomenclature stands only for illustrating purposes and it is not used in any other place).

## 6.2

### Isobar fit results

Now we present the results for each of the models showed in Table 6.2. These results are presented as follows: Starting with the CLEO model (baseline

model-1), we provide a brief description for the result of every model along with its correspondent tabulated values for magnitudes, phases and fit fractions for each resonance state. As this decay consists of three identical particles in the final state, the Dalitz invariants  $s_{12}$  and  $s_{13}$  are equal, therefore, presenting projections of these variables would add no relevant information. In this sense, we show the figures of the results on the so-called *folded* Dalitz plot, consisting of projections of the low and high mass along the  $s_{12} = s_{13}$  line.

**Model 1:** This is the baseline model. As can be seen on Figure 6.1, this fit is very poor but we can also see that the  $\sigma(500)$  dominates the  $D^+ \rightarrow \pi^- \pi^+ \pi^+$  decay with almost half of the total contribution, followed by  $\rho(770)$  with a fifth part, as Table 6.3 shows. These results are compatible with the ones from CLEO, in which  $\sigma(500)$  and  $\rho(770)$  contribute each with  $\sim 42\%$  and  $\sim 20\%$  respectively.

<b>Resonance</b>	<b>Magnitude</b>	<b>Phase (<math>^\circ</math>)</b>	<b>Fraction (%)</b>
$\rho(770)$	1 [fixed]	0 [fixed]	$20.7 \pm 0.2$
$f_0(980)$	$4.2 \pm 0.012$	$-159.2 \pm 0.5$	$8.2 \pm 0.2$
$f_2(1270)$	$1.2 \pm 0.004$	$94.6 \pm 0.4$	$13.2 \pm 0.1$
$f_0(1370)$	$2.8 \pm 0.04$	$-179 \pm 1.1$	$3.7 \pm 0.2$
$\sigma(500)$	$23.1 \pm 0.1$	$-99.6 \pm 0.2$	$49.6 \pm 0.6$
$f_0(1500)$	$2.4 \pm 0.04$	$154.7 \pm 0.8$	$3.3 \pm 0.2$
Total			98.7

Table 6.3: Results for magnitude, phase and fit fractions for the model-1. As mentioned above,  $\sigma(500)$  and  $\rho(770)$  dominates the decay. We can also observe secondary contributions from  $f_2(1270)$  and  $f_0(980)$ .

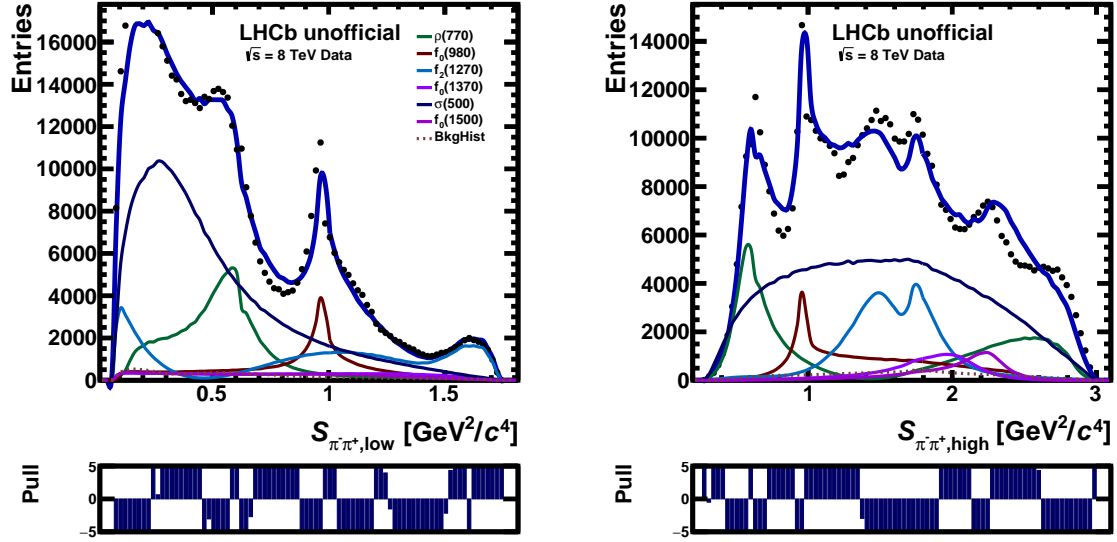


Figure 6.1: Squared mass ( $s_{low}$ ,  $s_{high}$ ) projections for the model-1. The dotted distribution represents the data, while the dark blue line represent the total PDF from the fit. Lineshapes for the intensity of individual contributions are also shown.

**Model 2:** In this model we add the  $\rho(1450)$  contribution. Whereas its fit fraction is very tiny, we found in latter fits that when not including its contribution, the total PDF description gets worse. Table 6.4 and Figure 6.2 show the fit results for this model.

Resonance	Magnitude	Phase ( $^\circ$ )	Fraction (%)
$\rho(770)$	1 [fixed]	0 [fixed]	$20.4 \pm 0.2$
$f_0(980)$	$4.4 \pm 0.02$	$-162.1 \pm 0.5$	$8.8 \pm 0.2$
$f_2(1270)$	$1.2 \pm 0.01$	$86 \pm 0.6$	$13.7 \pm 0.1$
$\rho(1450)$	$0.9 \pm 0.04$	$15.2 \pm 1.2$	$0.5 \pm 0.1$
$f_0(1370)$	$2.8 \pm 0.04$	$171.3 \pm 1.2$	$3.6 \pm 0.2$
$\sigma(500)$	$22.6 \pm 0.1$	$-102.8 \pm 0.3$	$46.5 \pm 0.7$
$f_0(1500)$	$2.2 \pm 0.05$	$153.8 \pm 0.9$	$2.9 \pm 0.2$
Total			96.4

Table 6.4: Results for the model-2. This is model-1 plus  $\rho(1450)$  resonance. It can be seen that the  $\rho(1450)$  fit fraction very small although not negligible.

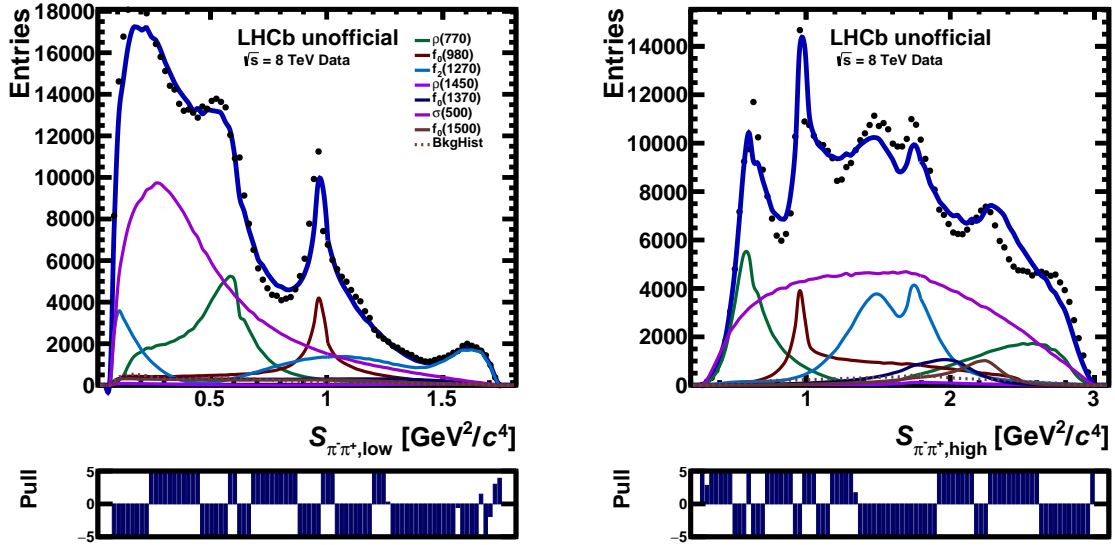


Figure 6.2:  $s_{\text{low}}$  and  $s_{\text{high}}$  projections for the model-2 PDF. Including the  $\rho(1450)$  resonance to model-1 does not improve the fit quality substantially but its contribution can not be ignored.

**Model 3:** In this model we add the non-resonant (NR) contribution. It is interesting to note that, while the  $\rho(1450)$  fraction is maintained, the  $f_0(1370)$  contribution drops significantly. Those results are shown in Table 6.2 and Figure 6.3

Resonance	Magnitude	Phase ( $^\circ$ )	Fraction (%)
$\rho(770)$	1 [fixed]	0 [fixed]	24.1 $\pm$ 0.3
$f_0(980)$	3.9 $\pm$ 0.02	-157.9 $\pm$ 0.5	8.1 $\pm$ 0.2
$f_2(1270)$	1.1 $\pm$ 0.01	89 $\pm$ 0.5	14.5 $\pm$ 0.2
$\rho(1450)$	0.7 $\pm$ 0.03	-80.2 $\pm$ 2.5	0.4 $\pm$ 0.1
$f_0(1370)$	0.9 $\pm$ 0.05	-175.6 $\pm$ 3.3	0.4 $\pm$ 0.1
$\sigma(500)$	23.2 $\pm$ 0.2	-88.1 $\pm$ 0.4	58.2 $\pm$ 1.5
NR	10.1 $\pm$ 0.2	-148.3 $\pm$ 1.1	7.5 $\pm$ 0.6
$f_0(1500)$	2.1 $\pm$ 0.04	-179.5 $\pm$ 1.1	2.9 $\pm$ 0.2
Total			116.02

Table 6.5: Fit results for the model-3, which consists of model-2 plus the NR term. In this model we observe that all the contributions, but  $\rho(1450)$ ,  $f_0(1370)$  and  $f_0(1500)$ , are increased, while the NR fit fraction is about 8%, which means that it cannot be neglected.

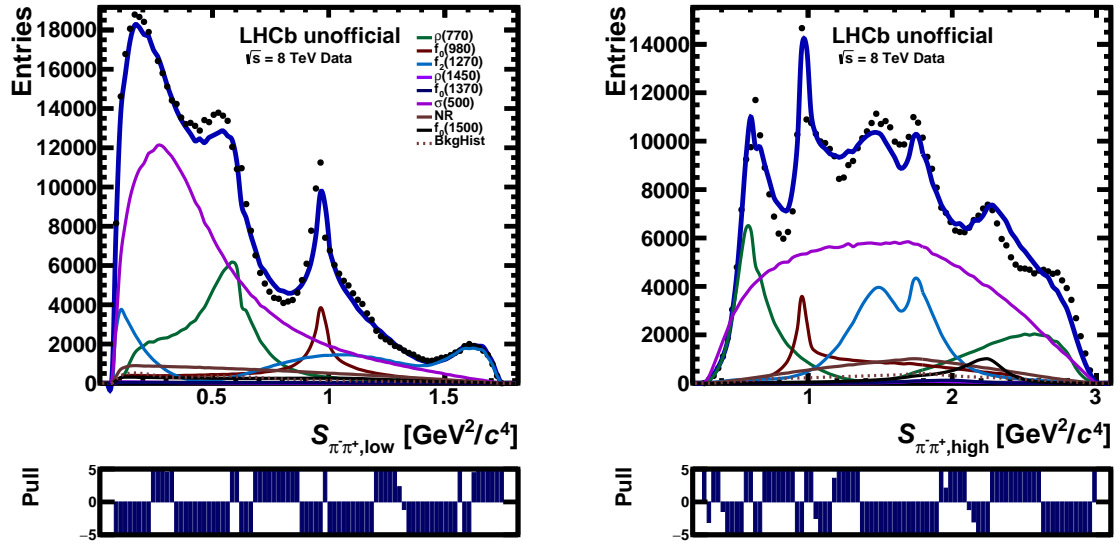


Figure 6.3: Results for the model-3 are shown in this figure. It can be observed that the fit gets a little better on the high mass region, but even considering eight contributions, the isobar model does not give an acceptable result.

As the above fits are very poor, we allowed to float masses and widths of those not well established resonances. These results are shown in the following paragraphs.

**Model 4:** In this model we allowed to float mass and width for  $f_0(1370)$  ( $f_0X$ ) resonance. As shown, although not satisfactory, the fit is slightly better than those with fix parameters. The fitted mass and width are respectively,  $m_{f_0(1370)} = 1.205 \pm 0.005$  GeV and  $\Gamma_{f_0(1370)} = 0.351 \pm 0.001$  GeV. It can be seen in Figure 6.4 that the fit has a slight improvement on the  $f_0X$  region. Table 6.6 shows that the  $f_0X$  fraction also increases a bit but not nearly enough for a good description of the data.

Resonance	Magnitude	Phase ( $^\circ$ )	Fraction (%)
$\rho(770)$	1 [fixed]	0 [fixed]	$25.5 \pm 0.7$
$f_0(980)$	$4.2 \pm 0.02$	$-159.2 \pm 0.5$	$10.1 \pm 0.3$
$f_2(1270)$	$1.1 \pm 0.004$	$85.2 \pm 0.4$	$14 \pm 0.4$
$\rho(1450)$	$0.5 \pm 0.02$	$-55.4 \pm 4.3$	$0.2 \pm 0.02$
$f_0(1370)$	$2.2 \pm 0.05$	$121.3 \pm 2.4$	$2.4 \pm 0.2$
$\sigma(500)$	$22.2 \pm 0.2$	$-89.9 \pm 0.4$	$56.1 \pm 2.2$
NR	$7.5 \pm 0.2$	$-140.4 \pm 1.8$	$4.3 \pm 0.4$
$f_0(1500)$	$2.1 \pm 0.03$	$177.9 \pm 0.7$	$3.2 \pm 0.2$
Total			115.7

Table 6.6: Results for model-4. In this fit we allowed to float mass and width for  $f_0 X$ . We observe that, compared to model-3, the  $f_0 X$  fit fractions increases six times, while the NR decreases half of its previous value.

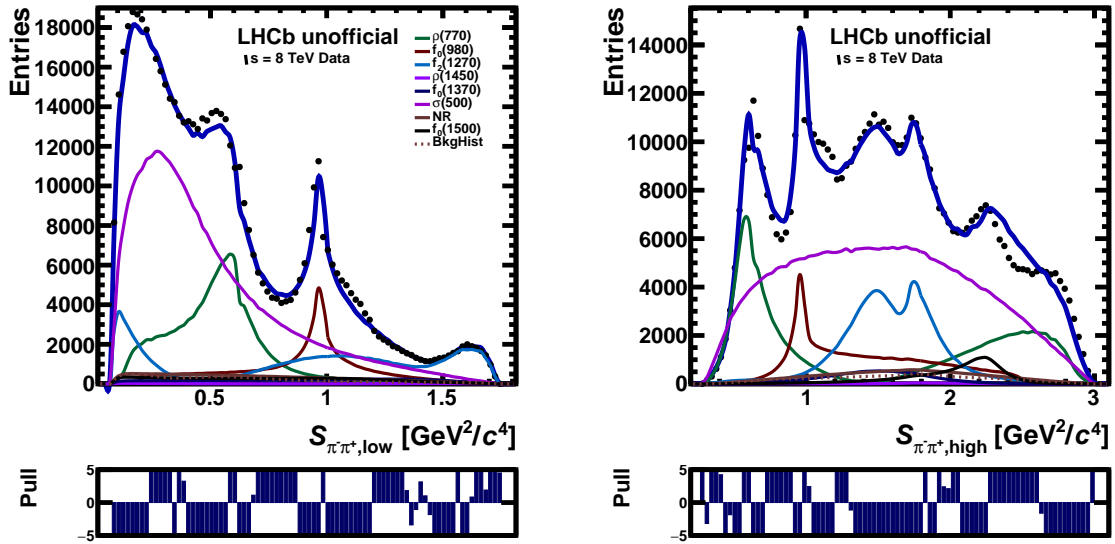


Figure 6.4: Squared mass projections illustrating model-4 results. The  $f_0 X$  region gets better described when floating its mass and width.

**Model 5:** In this model the mass and width for  $\sigma(500)$  resonance are allowed to float. The fitted values are respectively,  $m_{\sigma(500)} = 0.544 \pm 0.002$  GeV and  $\Gamma_{\sigma(500)} = 0.423 \pm 0.003$  GeV. It can be seen in Figure 6.5 that the fit has a slight improvement on the  $\sigma(500)$  region. Table 6.7 shows these results. One can observe that just floating mass and width for  $\sigma(500)$  is not enough for a good description of the data, and is also important to highlight that the  $\sigma(500)$  fit fraction is only 35% in this model.

Resonance	Magnitude	Phase ( $^\circ$ )	Fraction (%)
$\rho(770)$	1 [fixed]	0 [fixed]	$27.2 \pm 0.7$
$f_0(980)$	$3.7 \pm 0.02$	$-157.8 \pm 0.5$	$8.2 \pm 0.3$
$f_2(1270)$	$1 \pm 0.004$	$83 \pm 0.4$	$13.8 \pm 0.3$
$\rho(1450)$	$0.5 \pm 0.02$	$-54.1 \pm 3.5$	$0.2 \pm 0.04$
$f_0(1370)$	$0.3 \pm 0.04$	$117 \pm 8.6$	$0.1 \pm 0.04$
$\sigma(500)$	$5.8 \pm 0.1$	$-135.8 \pm 0.9$	$34.8 \pm 1$
NR	$10.5 \pm 0.3$	$-110 \pm 0.9$	$9.1 \pm 0.8$
$f_0(1500)$	$1.7 \pm 0.03$	$-171.4 \pm 1.4$	$2.2 \pm 0.2$
Total			95.7

Table 6.7: Model-5 results when mass and width for  $\sigma(500)$  are allowed to float. The main point here is the lower  $\sigma(500)$  fit fraction, compared to previous models.

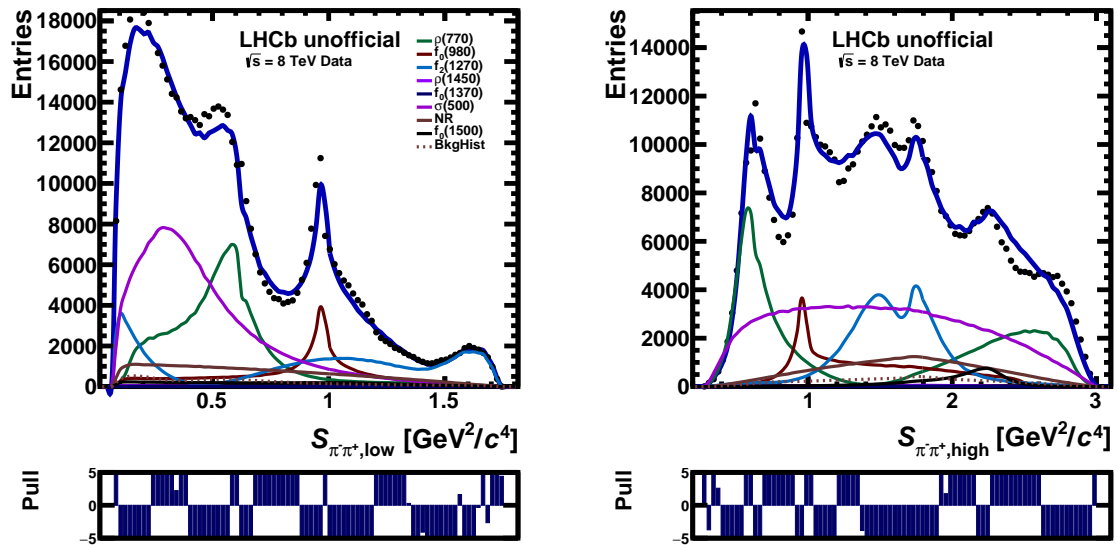


Figure 6.5: Projection for model-5. As observed, we do not obtain a good fit when floating the  $\sigma(500)$  mass and width.

**Model 6:** As observed above, fitting with fixed resonance parameters or only allowing to float either the  $f_0X$  or the  $f_0(500)$  parameters, the fit is not satisfactory. Following with this idea, we allowed to float mass and width for both the  $f_0X$  and the  $f_0(500)$  and compared with the results from previous models.

The fitted mass and width for  $f_0X$  are respectively,  $m_{f_0(1370)} = 1.551 \pm 0.0004$  GeV,  $\Gamma_{f_0(1370)} = 0.351 \pm 0.0003$  GeV, while the correspondent mass and width for  $f_0(500)$  are  $m_{\sigma(500)} = 0.506 \pm 0.002$  GeV,  $\Gamma_{\sigma(500)} = 0.424 \pm 0.003$  GeV. As seen in Figure 6.4 and in Table 6.6, even with eighteen free parameters, we

do not have a decent description for the data.

Resonance	Magnitude	Phase ( $^\circ$ )	Fraction (%)
$\rho(770)$	1 [fixed]	0 [fixed]	$26.2 \pm 0.3$
$f_0(980)$	$3.9 \pm 0$	$-162.8 \pm 0.5$	$8.8 \pm 0.2$
$f_2(1270)$	$1 \pm 0$	$79.4 \pm 0.5$	$13.2 \pm 0.2$
$\rho(1450)$	$0.5 \pm 0$	$27.5 \pm 2.5$	$0.2 \pm 0.1$
$f_0(1370)$	$4.8 \pm 0.1$	$-179.7 \pm 1.3$	$5.2 \pm 0.5$
$\sigma(500)$	$5.5 \pm 0.1$	$-152.9 \pm 0.8$	$30.2 \pm 1.2$
NR	$2.9 \pm 0.2$	$-52.6 \pm 5.4$	$0.7 \pm 0.2$
$f_0(1500)$	$1.1 \pm 0$	$-159.9 \pm 0.1$	$0.9 \pm 0.1$
Total			85.4

Table 6.8: Results for model-6, with eight resonances, with free masses and widths for  $f_0 X$  and  $\sigma(500)$ . This model increases the  $f_0 X$  portion but maintain a low  $\sigma(500)$  fit fraction and lowers the non-resonant contribution.

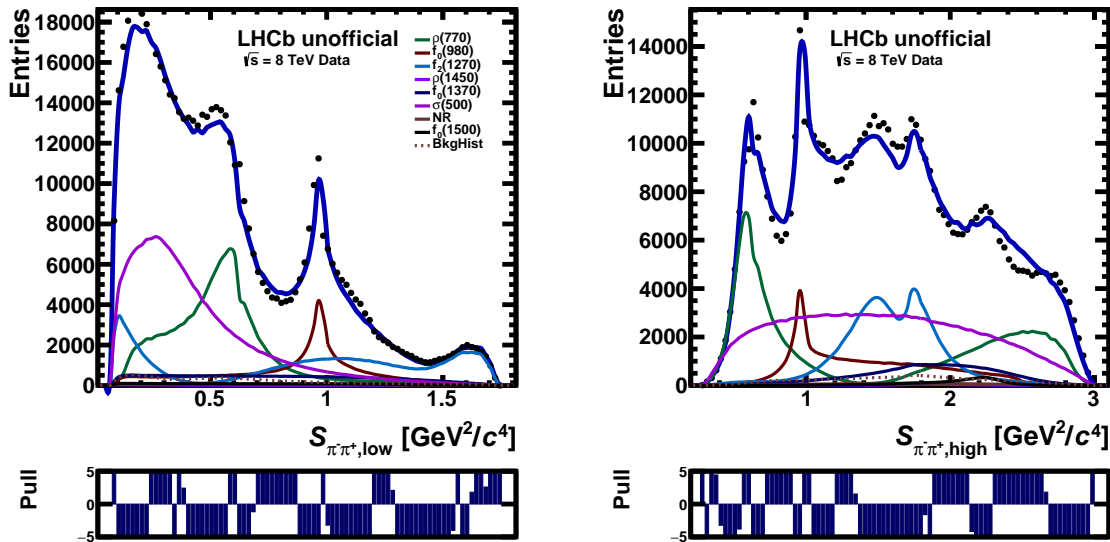


Figure 6.6: Results for the model-6 are shown. In this figure it is possible to observe the complications that presents the isobar model for the  $D^+ \rightarrow \pi^- \pi^+ \pi^+$  channel: even including all possible contributions, and floating the not well defined resonance parameters, the fit continues providing a poor performance.

### 6.2.1

#### Summary of Isobar Model results

In the previous section, the fit results for the Isobar Model, with some of its more relevant variants, were presented. Figure 6.7 shows a comparison of the fractions and phases for the model-3, which showed an acceptable

Model	1	2	3	4	5	6
$\rho(770)$	20.7±0.2	20.4±0.2	24.1±0.3	25.4 ±0.7	27.2± 0.7	26.1±0.3
$f_0(980)$	8.2±0.1	8.8±0.2	8.1± 0.2	10.1 ±0.3	8.2 ±0.3	8.8±0.2
$f_2(1270)$	13.2±0.2	13.7±0.1	14.5±0.2	14.04±0.4	13.8 ±0.3	13.2±0.2
$\rho(1450)$	✗	0.5±0.1	0.4± 0.1	0.2 ±0.02	0.2 ±0.04	0.2±0.05
$f_0X$	3.7±0.2	3.6±0.2	0.4± 0.1	2.4 ±0.2	0.1 ±0.04	5.2±0.5
$\sigma(500)$	49.6±0.6	46.5±0.7	58.2±1.4	56.1 ±2.2	34.8 ±1.0	30.2±1.2
NR	✗	✗	7.5± 0.6	4.3 ±0.4	9.1 ±0.8	0.7±0.2
$f_0(1500)$	3.3±0.2	2.9±0.2	2.9± 0.2	3.2 ±0.2	2.2 ±0.2	0.9±0.1
Total	98.7	96.4	116.02	115.7	95.7	85.4

Table 6.9: Summary of the models fitted using the Isobar Model. Results for all the relevant models are showed.

behavior. Table 6.9 summarizes the fit fractions and the total sum of fractions for all models, it can be seen that in all cases, the  $S$ -wave, which includes  $f_0(500)$ ,  $f_0(980)$ ,  $f_0(1370)$ ,  $f_0(1500)$  and NR, dominates the decay. The  $D$ -wave,  $f_2(1270)$ , is less than 15% for all models.

Generally speaking, a Dalitz plot analysis using Isobar Model may not be enough to achieve a correct description of the  $D^+ \rightarrow \pi^- \pi^+ \pi^+$  decay, thus the Model Independent Partial Wave Analysis must be implemented. Nevertheless, if we look in general, we can observe that even the simplest (CLEO) model gives a reasonable fit at low mass (if compared to the rest of the presented models), the main complication comes from the high mass region, where we have the  $f_0(1370)$  resonance (with mass and width poorly delimited), together with the  $f_2(1270)$ ,  $\rho(1450)$  and  $f_0(1500)$ , hence a better formulation of this scenario is needed, to include in the model another hidden effects that we probably are not taking into account.

On the other hand, during the course of this research we made a lot of tests not mentioned above. We attempted to experimentally measure the  $\rho$ - $\omega$  mixing parameters, we also floated the parameters of the Flatté function used to model the  $f_0(980)$ , and also allowed to float masses and widths of some resonances. In none of the cases we obtained an acceptable result, but this behavior was already expected, mainly because of the exposed in the last paragraph.

## $D^+ \rightarrow \pi^- \pi^+ \pi^+$ isobar fit results (Model 3)

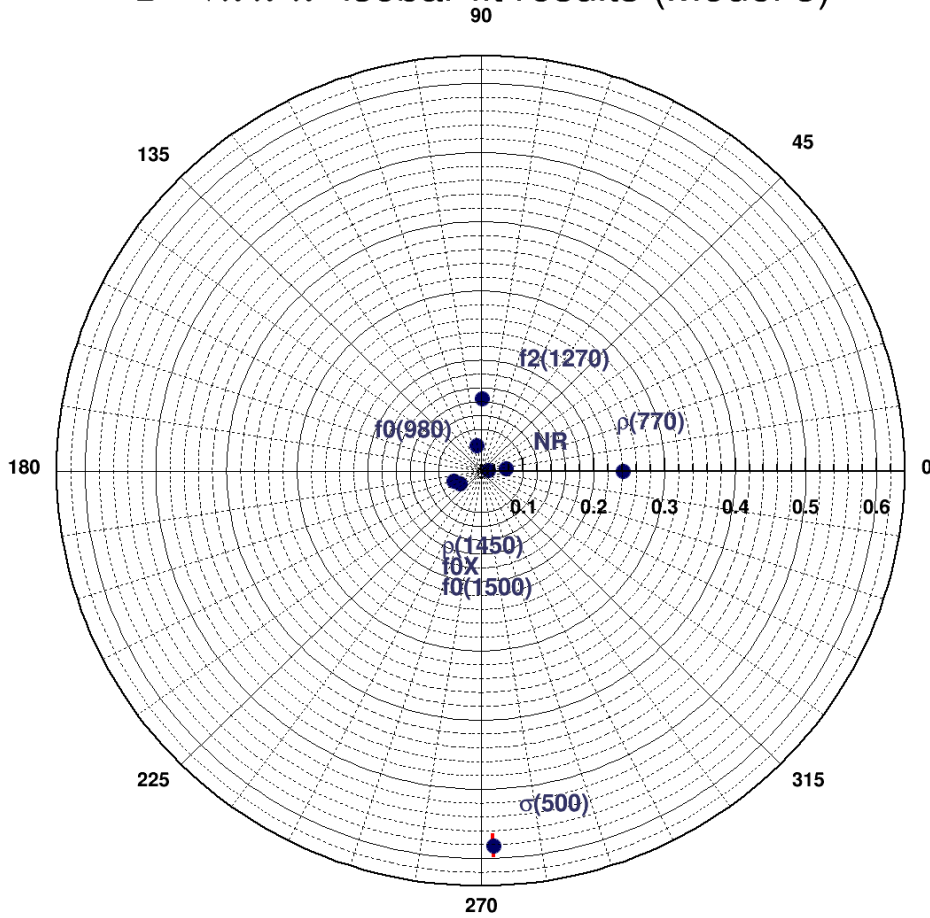


Figure 6.7: Polar coordinates comparison of fitted quantities for model-3. The radial  $r$  component represents the fit fraction, and  $\theta$  is the phase. It can be observed that the main contribution comes from  $\sigma(500)$ .

### 6.3

#### MI-PWA fit results

As we have seen in the previous section, using the isobar model is not enough for a correct description of the data, either considering that the decay  $D^+ \rightarrow \pi^- \pi^+ \pi^+$  is too complex or because the fit is dependent on model. The quasi model independent partial wave analysis used in this thesis considers the isobar model to describe  $P$  and  $D$  waves, whereas the  $S$ -wave description is constructed independent of any model, as described in Sec. 2.4.4

The contemplated resonant states for the  $P$ -wave are  $\rho(770)$  and  $\rho(1450)$ , while the  $f_2(1270)$  is included for the  $D$ -wave. The data fit using this approach gives magnitudes and phases for each considered resonance<sup>1</sup>

<sup>1</sup>The fit considers the  $S$ -wave as an individual component, so a global phase for the  $S$ -wave is fixed.

contributing to the  $D^+ \rightarrow \pi^- \pi^+ \pi^+$ , as well as the magnitude and phase for each  $\pi^+ \pi^-$  mass interval, for the  $S$ -wave.

In this analysis we divide the  $\pi^+ \pi^-$  spectrum in 40 mass intervals (41 end points), totalizing 82 free parameters to be determined by the fit. Apart from the fixed  $\rho(770)$  reference parameters, we have 4 parameters from the isobars corresponding to  $P$  and  $D$  waves, so we have a total of 86 free parameters to be fitted.

Table 6.10 shows the fit result in the form of magnitudes, phases and fractions for the considered contributions from  $P$ ,  $D$  waves, as well as the  $S$ -wave, which contribution is predominant, as observed.

Resonance	Magnitude	Phase ( $^\circ$ )	Fraction (%)
$\rho(770)$	1 [fixed]	0 [fixed]	$18.5 \pm 0.1$
$f_2(1270)$	$1.4 \pm 0$	$90.7 \pm 0.5$	$15.5 \pm 0.4$
$\rho(1450)$	$0.002 \pm 0.0001$	$-179.7 \pm 2.3$	$0.03 \pm 0.001$
$PP_{S-Wave}$	1	0	$60.8 \pm 0.3$
Total			94.9

Table 6.10: Results of the magnitude, phase and fraction for every included contribution on the MI-PWA fit. We can observe that the  $S$ -wave dominates de decay, with secondary contributions from  $\rho(770)$  and  $f_2(1270)$ . The  $\rho(1450)$  fit fraction is compatible with zero. In this fit, we used 86 free parameters, 82 from the  $S$ -wave and 4 for the  $f_2(1270)$  and  $\rho(1450)$  resonances parameters.

The projections for the three invariant masses, as well as the  $\chi^2$  of the fit, are represented in Fig. 6.8. The quality of fit is superior to the one obtained from isobar model, as expected, since the  $S$ -wave is described by a much larger number of parameters and is not associated to any model.

The Figure 6.9 shows the intensity and phase variation of the  $S$ -wave as function of the  $\pi^+ \pi^-$  mass. We can observe that the  $S$ -wave populates the whole  $\pi^+ \pi^-$  mass spectrum and it is more intense on the low mass region, i.e. below  $1 \text{ GeV}/c^2$  threshold. Is interesting the fact that the  $S$ -wave reaches its minimum values at both sides of the  $f_0(980)$ . This behavior could be interpreted as an effect of destructive interference between the  $S$ -wave components, this is, the  $f_0(980)$  interferes destructively with  $\sigma(500)$  as well as with  $f_0(1370)$ .

Another important point on the MI-PWA fit is the fact that the  $\rho(1450)$  contribution is compatible with zero and hence negligible. The origin of this behavior is unclear, however, the fit gets worse if we remove this contribution. We observed the same behavior on the isobar model fit.

It is also observed a significant phase variation along all the spectrum, with minimum value of  $-120^\circ$  at the low mass threshold, with high variation at the  $f_0(980)$  region and a significant oscillation at the  $f_0(1370)$  region.

The results for magnitudes and phases of the considered mass intervals, concerning to the  $S$ -wave, are shown in Table 6.11.

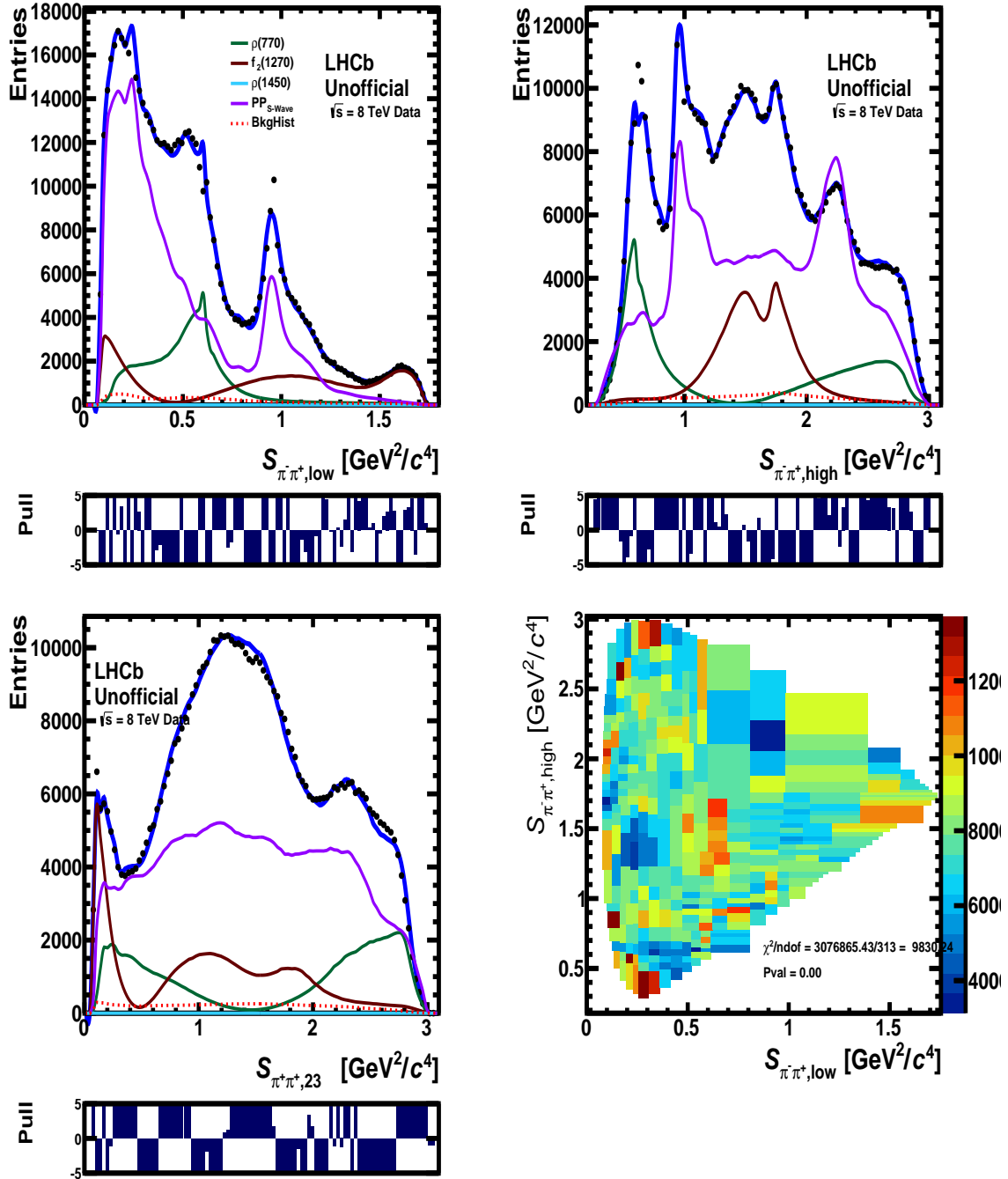


Figure 6.8: MI-PWA fit results. (Up)  $s_{low}$  and  $s_{high}$  projections from the fit. (Down)  $s_{23}$  projection -right- and  $\chi^2$  distribution with adaptive binning. It can be observed that the fit is better than the ones obtained in the Isobar Model, however, still need to be improved to get a complete description of the  $D^+ \rightarrow \pi^- \pi^+ \pi^+$  decay.

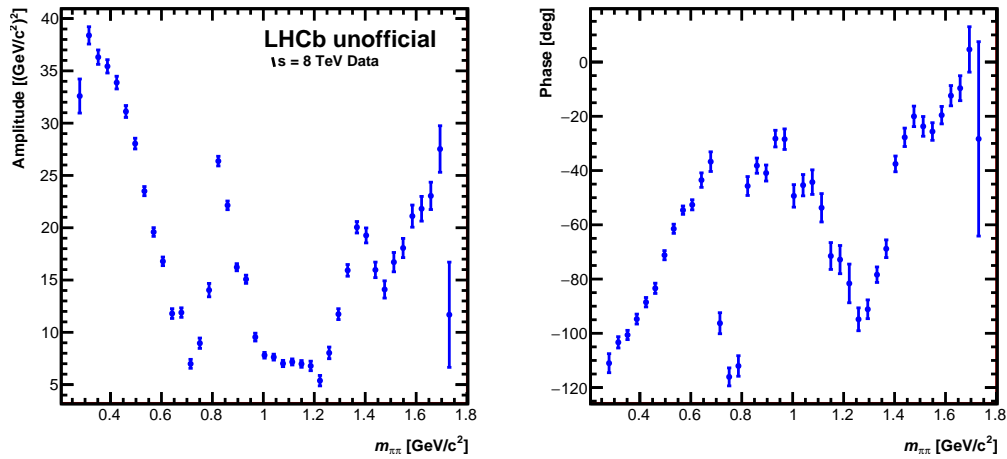


Figure 6.9: Magnitude and phase projections for the parameter distribution obtained from fit to data using Model Independent Partial Wave Analysis (MI-PWA) with 40 bins.

In general, although is being implemented for the first time on this channel, we can note that the MI-PWA fit is acceptable, with slight imperfections in the low mass region, specifically in the regions on the  $\rho(770)$  and  $f_0(980)$  resonances. Our explanation for this behavior is that in the first case, we have an interfering term coming from  $\omega(782)$ , with empirical parameters still needing to be better studied because, although we allowed them to float, it was not possible to obtain a good description of the  $\rho - \omega$  interference. For the second case, the difficulty in describing correctly the data comes from the fact that the  $f_0(980)$  width is too narrow and it is located at a high interference region, with contributions from almost all the rest of the  $S$ -wave components.

On the other hand, there is still room to improve this study, since is a relatively new research, we already have well developed the main tools of the analysis and new data has started to be taken recently at LHCb, therefore, we can analyze this channel with more statistics, using more sophisticated methods and techniques, as the case of implementing parallel calculations through GPU's (Graphics Process Unity), which allows to perform the fits in a tiny fraction of the time that it normally takes.

Bin	$m_{\pi^+\pi^-}$ (GeV/ $c^2$ )	Magnitude	Phase ( $^\circ$ )
1	0.27	$32.5 \pm 1.6$	$-111.01 \pm 3.5$
2	0.31	$38.3 \pm 0.8$	$-103.3 \pm 2.1$
3	0.35	$36.3 \pm 0.6$	$-100.6 \pm 1.7$
4	0.38	$35.4 \pm 0.6$	$-94.7 \pm 1.8$
5	0.42	$33.8 \pm 0.6$	$-88.5 \pm 1.7$
6	0.46	$31.1 \pm 0.57$	$-83.4 \pm 1.9$
7	0.49	$28.04 \pm 0.5$	$-71.2 \pm 1.6$
8	0.53	$23.5 \pm 0.4$	$-61.4 \pm 1.6$
9	0.56	$19.5 \pm 0.4$	$-54.6 \pm 1.5$
10	0.60	$16.7 \pm 0.5$	$-52.6 \pm 1.8$
11	0.64	$11.7 \pm 0.4$	$-43.5 \pm 2.6$
12	0.67	$11.8 \pm 0.4$	$-36.7 \pm 3.6$
13	0.71	$6.9 \pm 0.4$	$-96.2 \pm 3.8$
14	0.75	$8.9 \pm 0.5$	$-116.3 \pm 3.3$
15	0.78	$14.03 \pm 0.6$	$-112.8 \pm 3.7$
16	0.82	$26.3 \pm 0.5$	$-45.7 \pm 3.4$
17	0.85	$22.1 \pm 0.4$	$-38.1 \pm 2.7$
18	0.89	$16.2 \pm 0.3$	$-40.9 \pm 2.9$
19	0.93	$15.1 \pm 0.4$	$-28.2 \pm 3.1$
20	0.96	$9.5 \pm 0.4$	$-28.4 \pm 3.7$
21	1.0	$7.8 \pm 0.3$	$-49.3 \pm 4.1$
22	1.04	$7.6 \pm 0.3$	$-45.3 \pm 3.9$
23	1.08	$7.01 \pm 0.3$	$-44.2 \pm 4.5$
24	1.11	$7.2 \pm 0.3$	$-53.7 \pm 5.2$
25	1.14	$6.9 \pm 0.3$	$-71.5 \pm 4.9$
26	1.18	$6.7 \pm 0.4$	$-72.8 \pm 5.2$
27	1.22	$5.4 \pm 0.5$	$-81.6 \pm 7.1$
28	1.26	$8.03 \pm 0.5$	$-94.8 \pm 4.2$
29	1.29	$11.7 \pm 0.5$	$-91.1 \pm 3.4$
30	1.33	$15.9 \pm 0.5$	$-78.4 \pm 2.8$
31	1.36	$20.04 \pm 0.5$	$-68.8 \pm 3.2$
32	1.40	$19.2 \pm 0.7$	$-37.5 \pm 2.9$
33	1.44	$15.9 \pm 0.7$	$-27.7 \pm 3.3$
34	1.48	$14.1 \pm 0.8$	$-20.02 \pm 3.7$
35	1.52	$16.7 \pm 0.9$	$-23.7 \pm 3.6$
36	1.55	$18.1 \pm 0.9$	$-25.6 \pm 3.2$
37	1.58	$21.1 \pm 1.1$	$-19.5 \pm 3.2$
38	1.62	$21.8 \pm 1.181$	$-12.4 \pm 3.7$
39	1.66	$23.05 \pm 1.3$	$-9.6 \pm 4.5$
40	1.69	$27.5 \pm 2.2$	$4.6 \pm 8.3$
41	1.73	$11.6 \pm 5.03$	$-28.3 \pm 35.8$

Table 6.11: Fitted  $S$ -wave parameters at each mass bin edge in the form of magnitude and phase.

### 6.3.1

#### Summary of Isobar and MI-PWA fit results

We have presented in this chapter, the fit results for the  $D^+ \rightarrow \pi^- \pi^+ \pi^+$  decay using the Isobar Model and the Model Independent Partial Wave Analysis approach. In the section 6.2 were presented the fit results for the Isobar Model with some of its more relevant variants. We have seen that even with a fit model comprised of seven resonances plus a non-resonant state and allowing to float the masses and widths of two of those resonances, the obtained results are highly unsatisfactory. In some way, these results were already expected to behave this way, since an isobar fit of the  $D^+ \rightarrow \pi^- \pi^+ \pi^+$  decay is very challenging and because due to the complicated structure of its  $S$ -wave, a better formulation is needed.

Despite the aforementioned, the Isobar Model allowed us to make some interesting inferences and interpretations, many of them widely known from past experiences, and others not so well understood:

- Besides the complicated formulation of the  $S$ -wave, we have a set of well identified contributions comprised by  $\rho(770)$ ,  $f_2(1270)$ ,  $\sigma(500)$  and  $f_0(980)$ .
- Even with very small contributions, the  $f_0(1500)$  and  $\rho(1450)$  resonances are important to the stability of the fit.
- We have no clear picture for the non-resonant state (NR) against the  $f_0(1370)$  ( $f_0X$ ) contribution.
- Another important point is the fact that we are very sensitive to precise form of resonance line-shapes and in some cases we are using phenomenological models not well studied yet or not widely accepted by all the experimentalists and theorists, as the case of modeling the  $\rho(1450)$  with a Gounaris-Sakurai line-shape, and the models used to take into account the  $f_0(500)$ ,  $f_0(980)$  resonances or the  $\rho - \omega$  interference.

We have also shown the potentiality of the Model Independent Partial Wave Analysis to describe the  $S$ -wave on the  $D^+ \rightarrow \pi^- \pi^+ \pi^+$  decay, even being the latter a challenging channel, with high levels of combinatorial background, with a complicated resonant structure and particularly, with a rich and singular scalar structure piled up in a narrow  $\pi^+ \pi^-$  mass.

## Conclusions

The main objective of the present thesis was the study of the resonant structure of the  $D^+ \rightarrow \pi^- \pi^+ \pi^+$  decay using the so-called Isobar Model in a first approach and the Model Independent Partial Wave Analysis (MI-PWA), in a second stage, to measure the  $m_{\pi^+ \pi^-}$  amplitude of the  $S$ -wave.

Before describing the main components of the analysis we made a theoretical review of the essential aspects of the Dalitz plot analysis with emphasis on the Isobar Model and the Model Independent Partial Wave Analysis (MI-PWA) prior to reviewing the state-of-art of the research on the study of the resonant structure of the  $D^+ \rightarrow \pi^- \pi^+ \pi^+$  decay.

The analysis was done with 611 846 events in the  $3\pi$  signal region passing all selection criteria. This data was taken in 2012 by the LHCb detector, and corresponds to an integrated luminosity of  $2 \text{ fb}^{-1}$ . The first step to perform this analysis was a detailed study of the sample selection. The goal was to obtain a  $D^+ \rightarrow \pi^- \pi^+ \pi^+$  sample with the lowest possible contamination of background, with the maximum of the efficiency and at the same time maintaining the acceptance as uniform as possible. As this decay is highly contaminated with pionic background, it was necessary to implement a multivariate analysis in which the main variables of the decay are combined into a simple classifier previously trained to identify signal and background patterns.

Within the signal region there are 611 846 candidates corresponding to signal with a purity of 97% calculated within the  $2\sigma_{eff}$  mass window. This purity was chosen because, after studying several BDT cuts, trying to maintain the uniformity across the Dalitz, we finally had to prioritize high purity (due to the background complexity), so we must go up to 97% purity.

Because in this channel is very difficult to achieve a high purity just through rectangular cuts (we have a compromise between purity and signal efficiency), it was necessary to perform a multivariate analysis (MVA) using Boosted Decision Trees (BDT). Thus, we could obtain a sample with high purity, selecting a cut according to the above criteria.

Once we had defined our final selection, we used Monte Carlo generated samples to obtain an acceptance map in order to correct possible asymmetries that the selection could introduce.

We also needed to parameterize the background contributions, so we used the sidebands as input to an histogram posteriorly smoothed with spline functions. This histogram is introduced as a background specie in the fit. We

also applied a veto on the  $K_s^0$  mass.

Having completed the main steps of the analysis, we proceeded to fit the data. First we performed the fits using the Isobar Model approach and after that, we implemented the Model Independent Partial Wave Analysis (MI-PWA), for the first time on this channel.

For the Isobar Model we found that the final result is not enough to describe our data; even with eight contributions, and floating mass and width for some troublesome resonances, the fit is still poor. The main conclusion is that the Isobar Model is not enough, or we need to take into account another not well understood effects, in order to obtain a reasonably result.

On the Model Independent Partial Wave Analysis approach, we obtained slightly better results; still far from optimal, but this is a long term research and the results presented for now, are just starting points to a deeper study. In particular, we are planning to compare the  $S$ -wave phase behavior with the one from  $D_s^+ \rightarrow \pi^- \pi^+ \pi^+$ , to see if they are comparable, due to the fact that these decays have the same final state. The amplitude analysis of that decay is also underway, thus we will make this comparison.

Moreover, we only presented here statistical errors, we have not implemented systematic checks which, with the large sample we have, may dominate the results.

As a final conclusion, despite the eventualities that we had to overcome – either because this channel has a challenging background or due to the limitations of the Isobar Model to give a correct description of its resonant structure, or because we still have some not well understood effects on the MI-PWA fit – the general feeling is that these results are very promising in the long term and we will make it worthwhile.

## Bibliography

- [1] Weinberg, S. A model of leptons. *Phys. Rev. Lett.*, 19:1264–1266, 1967.
- [2] Salam, A. Weak and electromagnetic interactions. 1969. Proc. of the 8th Nobel Symposium on ‘Elementary particle theory, relativistic groups and analyticity’, Stockholm, Sweden, 1968, edited by N. Svartholm, p.367-377.
- [3] Glashow, S. L. Partial symmetries of weak interactions. *Nucl. Phys.*, 22:579–588, 1961.
- [4] Collaboration, C. Observation of a new boson at a mass of 125 gev with the cms experiment at the lhc. *Physics Letters B*, 716:30–61, 2012.
- [5] ATLAS Collaboration. Observation of a new particle in the search for the standard model higgs boson with the atlas detector at the lhc. *Physics Letters B*, 716:1–29, 2012.
- [6] Sakharov, A. D. Violation of cp invariance, c asymmetry, and baryon asymmetry of the universe. *Journal of Experimental and Theoretical Physics*, 5:24–27, 1967.
- [7] Kobayashi, M. and Maskawa, T. CP violation in the renormalizable theory of weak interaction. *Prog.Theor.Phys.*, 49:652–657, 1973. doi: 10.1143/PTP.49.652.
- [8] Cabibbo, N. Unitary symmetry and leptonic decays. *Phys.Rev.Lett.*, 10:531–533, 1963. doi:10.1103/PhysRevLett.10.531.
- [9] Fermi, E. Tentativo di una teoria dei raggi beta. *Il Nuovo Cimento*, 11:1–19, 1934.
- [10] Aaij, R. et al. Search for CP violation in  $D^+ \rightarrow \pi^- \pi^+ \pi^+$  decays. *Phys. Lett.*, B728:585, 2013.
- [11] Olive, K. A. et al. (Particle Data Group). *Chin. Phys. C*, 38(9):09001, 2014.
- [12] D. Herndon, P. S. and Cashmore, R. A generalised isobar model formalism. *Phys.Rev.D*, 11:3165, 1975.
- [13] Blatt, J. and Weisskopf, V. E. *Theoretical Nuclear Physics*. J. Wiley (New York), 1952.

- [14] Zemach, C. Three pion decays of unstable particles. *Phys.Rev.*, 133:B1201, 1964. doi:10.1103/PhysRev.133.B1201.
- [15] Gounaris, G. J. and Sakurai, J. J. Finite-width corrections to the vector-meson-dominance prediction for  $\rho \rightarrow e^+e^-$ . *Phys.Rev.Lett.*, 21:244, 1968. doi:10.1103/PhysRevLett.21.244.
- [16] Collaboration, C.-. Measurement of  $e^+e^- \rightarrow \pi^+\pi^-$  cross section with cmd-2 around rho-meson. *Phys. Lett.*, B527:161, 2002.
- [17] Bugg, D. Comments on the sigma and kappa. *Phys.Lett.*, B572:1–7, 2003. doi:10.1016/j.physletb.2004.06.050.
- [18] Weinberg, S. Pion scattering lengths. *Phys. Rev. Lett.*, 17:616, 1966.
- [19] collaboration, L. Analysis of the resonant components in  $b^0 \rightarrow j/\psi \pi^+ \pi^-$ . *Phys. Rev.*, D87:19, 2013.
- [20] Flatté, S. M. Nature of scalar resonances. *Phys. Lett.*, B63:224, 1976.
- [21] Bevan, A. J. et al. the physics of the b factories. *Eur. Phys.*, C74, 2014.
- [22] E. Aitala, e. a. Model independent measurement of swave  $k^- \pi^+$  systems using  $d^+ \rightarrow k^- \pi^+ \pi^+$  decays from fermilab e791. *Phys. Rev.*, D73, 2006.
- [23] Aitala, E. et al. experimental evidence for a light and broad scalar resonance in  $d^+ \rightarrow \pi^- \pi^+ \pi^+$ . *Phys. Rev. Lett.*, 86, 2001.
- [24] Collaboration, F. Dalitz plot analysis of  $d_s^+$  and  $d^+$  decay to  $\pi^- \pi^+ \pi^+$  using the k-matrix formalism. *Phys.Lett.*, B585, 2004.
- [25] c Collaboration, C. Dalitz plot analysis of  $d^+ \rightarrow \pi^- \pi^+ \pi^+$ . *Phys. Rev.*, D76, 2007.
- [26] Collaboration, B. Dalitz plot analysis of  $d_s^+ \rightarrow \pi^- \pi^+ \pi^+$ . *Phys. Rev.*, D79, 2009.
- [27] Alves Jr., A. A. et al. The LHCb detector at the LHC. *JINST*, 3:S08005, 2008. doi:10.1088/1748-0221/3/08/S08005.
- [28] Collaboration, L. Lhcb Magnet: Technical Design Report. *CERN/LHCC*, LHCb-TDR-1, 2000.
- [29] Collaboration, L. Lhcb velo upgrade technical design report. *CERN/LHCC*, LHCb TDR 13, 2013. 2013-021.

- [30] Hutchcroft, D. Velo pattern recognition. *LHCb-VELO*, pages 1–5, 2007. 2007-013.
- [31] Collaboration, L. Lhcb inner tracker technical design report. *CERN/LHCC 2002-029*, LHCb TDR 008, 2002.
- [32] Collaboration, L. Lhcb outer tracker technical design report. *CERN/LHCC/2001-024*, LHCb TDR 006:1–9, 2001.
- [33] Collaboration, L. Lhcb rich technical design report. *CERN LHCC LHCb TDR 3*, pages 1–9 and 47–56, 2000. 2000-037.
- [34] Collaboration, L. Lhcb calorimeters technical design report. *CERN/LHCC*, LHCb TDR 2, 2000. 2000-0036.
- [35] Collaboration, L. Lhcb muon system technical design report. *LHCb-VELO 2007-013*, LHCb TDR 4, 2001. 2001-010.
- [36] Gligorov, V. V. A single track HLT1 trigger.
- [37] collaboration, L. LHCb Trigger and Online Technical Design Report, 2014. LHCb-TDR-016.
- [38] G. Barrand, P. B. M. C. R. C. e. a., I. Belyaev. GAUDI - A software architecture and framework for building HEP data processing applications. *Comput.Phys.Commun*, 140:45–55, 2001.
- [39] I. Belyaev, S. E. P. M. J. P. W. P. F. R.-j., P. Charpentier and van Tilburg, J. Simulation application for the LHCb experiment. *eConf*, C0303241:TUMT003, 2003.
- [40] Sjöstrand, T., Mrenna, S., and Skands, P. PYTHIA 6.4 physics and manual. *JHEP*, 05:026, 2006. doi:10.1088/1126-6708/2006/05/026.
- [41] Lange, D. J. The evtgen particle decay simulation package. *Nuclear Instruments and Methods in Physics Research Section A: Accelerators, Spectrometers, Detectors and Associated Equipment*, 462(1):152–155, 2001.
- [42] et al, S. A. GEANT4: A Simulation toolkit. *Nucl.Instrum.Meth.*, A506:250–303, 2003.
- [43] The boole project. [online] <http://lhcb-release-area.web.cern.ch/LHCb-release-area/DOC/boole/>.
- [44] The boole project. [online] <http://lhcb-release-area.web.cern.ch/LHCb-release-area/DOC/moore/>.

- [45] The brunel project. [online] <http://lhcb-release-area.web.cern.ch/LHCb-release-area/DOC/brunel/>.
- [46] The davinci project. [online] <http://lhcb-release-area.web.cern.ch/LHCb-release-area/DOC/davinci/>.
- [47] The panoramix project. [online] <http://lhcb-release-area.web.cern.ch/LHCb-release-area/DOC/panoramix/>.
- [48] Lamont, M. Status of the LHC. *Journal of Physics: Conference Series*, 455-012001, 2013. Doi:10.1088/1742-6596/455/1/012001.
- [49] Pidcalib packages. [online] <https://twiki.cern.ch/twiki/bin/view/LHCb/PIDCalibPackage>.
- [50] Breiman, L., Friedman, J. H., Olshen, R. A., and Stone, C. J. *Classification and regression trees*. Wadsworth international group, Belmont, California, USA, 1984.
- [51] Hulsbergen, W. D. Decay chain fitting with a Kalman filter. *Nucl.Instrum.Meth.*, A552:566–575, 2005. doi:10.1016/j.nima.2005.06.078.
- [52] Powell, A. et al. Particle identification at LHCb. *PoS, ICHEP2010:020*, 2010. LHCb-PROC-2011-008.
- [53] Charm rio group. rio+ dalitz plot fitting package. Local Repository.
- [54] Press, W. H., Teukolsky, S. A., Vetterling, W. T., and Flannery, B. P. *Numerical Recipes in C*. Cambridge University Press, Cambridge, 1998.
- [55] Williams, M. How good are your fits. *arXiv:1006.3019v2*, 2010.
- [56] Beringer, J. et al. Review of particle physics. *Phys. Rev.*, D86:010001, 2012. doi:10.1103/PhysRevD.86.010001. and 2013 partial update for the 2014 edition.

**A**

**Search for CP violation in the decay  $D^+ \rightarrow \pi^- \pi^+ \pi^+$**



Contents lists available at ScienceDirect

Physics Letters B

www.elsevier.com/locate/physletb

Search for  $CP$  violation in the decay  $D^+ \rightarrow \pi^- \pi^+ \pi^+$ 

CrossMark

.LHCb Collaboration

## ARTICLE INFO

## Article history:

Received 29 October 2013

Received in revised form 6 December 2013

Accepted 10 December 2013

Available online 17 December 2013

Editor: M. Doser

## ABSTRACT

A search for  $CP$  violation in the phase space of the decay  $D^+ \rightarrow \pi^- \pi^+ \pi^+$  is reported using  $pp$  collision data, corresponding to an integrated luminosity of  $1.0 \text{ fb}^{-1}$ , collected by the LHCb experiment at a centre-of-mass energy of 7 TeV. The Dalitz plot distributions for  $3.1 \times 10^6$   $D^+$  and  $D^-$  candidates are compared with binned and unbinned model-independent techniques. No evidence for  $CP$  violation is found.

© 2013 The Authors. Published by Elsevier B.V.

## 1. Introduction

In the Standard Model (SM) charge-parity ( $CP$ ) violation in the charm sector is expected to be small. Quantitative predictions of  $CP$  asymmetries are difficult, since the computation of strong-interaction effects in the non-perturbative regime is involved. In spite of this, it was commonly assumed that the observation of asymmetries of the order of 1% in charm decays would be an indication of new sources of  $CP$  violation ( $CPV$ ). Recent studies, however, suggest that  $CP$  asymmetries of this magnitude could still be accommodated within the SM [1–4].

Experimentally, the sensitivity for  $CPV$  searches has substantially increased over the past few years. Especially with the advent of the large LHCb data set,  $CP$  asymmetries at the  $\mathcal{O}(10^{-2})$  level are disfavoured [5–9]. With uncertainties approaching  $\mathcal{O}(10^{-3})$ , the current  $CPV$  searches start to probe the regime of the SM expectations.

The most simple and direct technique for  $CPV$  searches is the computation of an asymmetry between the particle and anti-particle time-integrated decay rates. A single number, however, may not be sufficient for a comprehension of the nature of the  $CP$  violating asymmetry. In this context, three- and four-body decays benefit from rich resonance structures with interfering amplitudes modulated by strong-phase variations across the phase space. Searches for localised asymmetries can bring complementary information on the nature of the  $CPV$ .

In this Letter, a search for  $CP$  violation in the Cabibbo-suppressed decay  $D^+ \rightarrow \pi^- \pi^+ \pi^+$  is reported.<sup>1</sup> The investigation is performed across the Dalitz plot using two model-independent techniques, a binned search as employed in previous LHCb analyses [10,11] and an unbinned search based on the nearest-

neighbour method [12,13]. Possible localised charge asymmetries arising from production or detector effects are investigated using the decay  $D^+ \rightarrow \pi^- \pi^+ \pi^+$ , which has the same final state particles as the signal mode, as a control channel. Since it is a Cabibbo-favoured decay, with negligible loop (penguin) contributions,  $CP$  violation is not expected at any significant level.

## 2. LHCb detector and data set

The LHCb detector [14] is a single-arm forward spectrometer covering the pseudorapidity range  $2 < \eta < 5$ , designed for the study of particles containing  $b$  or  $c$  quarks. The detector includes a high-precision tracking system consisting of a silicon-strip vertex detector surrounding the  $pp$  interaction region, a large-area silicon-strip detector located upstream of a dipole magnet with a bending power of about 4 Tm, and three stations of silicon-strip detectors and straw drift tubes placed downstream. The combined tracking system provides a momentum measurement with relative uncertainty that varies from 0.4% at 5 GeV/c to 0.6% at 100 GeV/c, and impact parameter (IP) resolution of 20  $\mu\text{m}$  for tracks with high transverse momentum,  $p_T$ . Charged hadrons are identified using two ring-imaging Cherenkov (RICH) detectors [15]. Photon, electron and hadron candidates are identified by a calorimeter system consisting of scintillating-pad and preshower detectors, an electromagnetic calorimeter and a hadronic calorimeter. Muons are identified by a system composed of alternating layers of iron and multiwire proportional chambers [16]. The trigger [17] consists of a hardware stage, based on information from the calorimeter and muon systems, followed by a software stage, which applies full event reconstruction. At the hardware trigger stage, events are required to have muons with high transverse momentum or hadrons, photons or electrons with high transverse energy deposit in the calorimeters. For hadrons, the transverse energy threshold is  $3.5 \text{ GeV}/c^2$ .

The software trigger requires at least one good quality track from the signal decay with high  $p_T$  and high  $\chi_{\text{IP}}^2$ , defined as the difference in  $\chi^2$  of the primary vertex (PV) reconstructed with and without this particle. A secondary vertex (SV) is formed by three tracks

<sup>1</sup> Unless stated explicitly, the inclusion of charge conjugate states is implied.

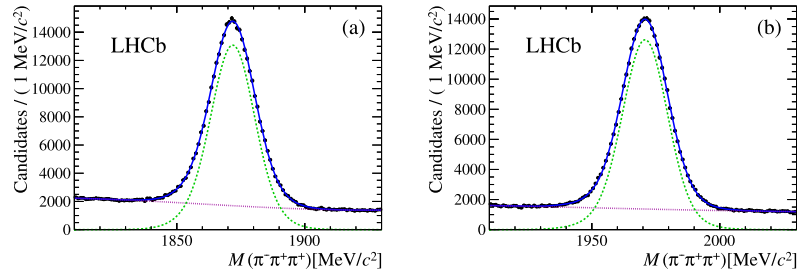


**Fig. 1.** Invariant-mass distributions for (a)  $D^+$  and (b)  $D_s^+$  candidates in the momentum range  $50 < p_{D_{(s)}} < 100$  GeV/c for magnet up data. Data points are shown in black. The solid (blue) line is the fit function, the (green) dashed line is the signal component and the (magenta) dotted line is the background.

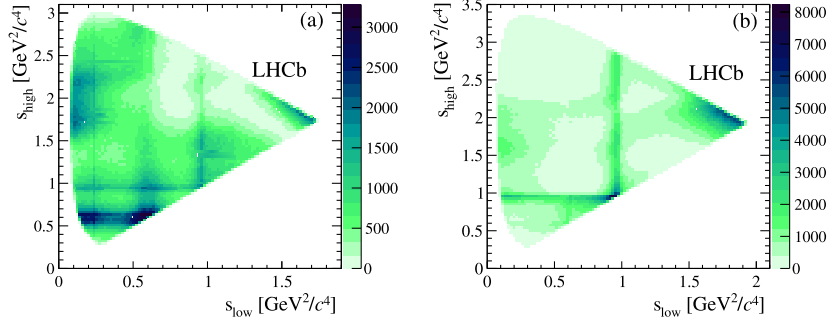


**Fig. 2.** Dalitz plots for (a)  $D^+ \rightarrow \pi^- \pi^+ \pi^+$  and (b)  $D_s^+ \rightarrow \pi^- \pi^+ \pi^+$  candidates selected within  $\pm 2\sigma$  around the respective  $\bar{m}$  weighted average mass.

with good quality, each not pointing to any PV, and with requirements on  $p_T$ , momentum  $p$ , scalar sum of  $p_T$  of the tracks, and a significant displacement from any PV.

The data sample used in this analysis corresponds to an integrated luminosity of  $1.0 \text{ fb}^{-1}$  of  $pp$  collisions at a centre-of-mass energy of 7 TeV collected by the LHCb experiment in 2011. The magnetic field polarity is reversed regularly during the data taking in order to minimise effects of charged particle and antiparticle detection asymmetries. Approximately half of the data are collected with each polarity, hereafter referred to as “magnet up” and “magnet down” data.

### 3. Event selection

To reduce the combinatorial background, requirements on the quality of the reconstructed tracks, their  $\chi_{\text{IP}}^2$ ,  $p_T$ , and scalar  $p_T$  sum are applied. Additional requirements are made on the secondary vertex fit quality, the minimum significance of the displacement from the secondary to any primary vertex in the event, and the  $\chi_{\text{IP}}^2$  of the  $D_{(s)}^+$  candidate. This also reduces the contribution of secondary  $D$  mesons from  $b$ -hadron decays to 1–2%, avoiding the introduction of new sources of asymmetries. The final-state particles are required to satisfy particle identification (PID) criteria based on the RICH detectors.

After these requirements, there is still a significant background contribution, which could introduce charge asymmetries across the Dalitz plot. This includes semileptonic decays like  $D^+ \rightarrow K^- \pi^+ \mu^+ \nu$  and  $D^+ \rightarrow \pi^- \pi^+ \mu^+ \nu$ ; three-body decays, such as  $D^+ \rightarrow K^- \pi^+ \pi^+$ ; prompt two-body  $D^0$  decays forming a three-prong vertex with a random pion; and  $D^0$  decays from the  $D^{*+}$  chain, such as  $D^{*+} \rightarrow D^0(K^- \pi^+, \pi^- \pi^+, K^- \pi^+ \pi^0) \pi^+$ . The contribution from  $D^+ \rightarrow K^- \pi^+ \pi^+$  and prompt  $D^0$  decays that involve the misidentification of the kaon as a pion is reduced to a negligible level with a more stringent PID requirement on the  $\pi^-$

candidate. The remaining background from semileptonic decays is controlled by applying a muon veto to all three tracks, using information from the muon system [18]. The contribution from the  $D^{*+}$  decay chain is reduced to a negligible level with a requirement on  $\chi_{\text{IP}}^2$  of the  $\pi^+$  candidate with lowest  $p_T$ .

Fits to the invariant mass distribution  $M(\pi^- \pi^+ \pi^+)$  are performed for the  $D^+$  and  $D_s^+$  candidates satisfying the above selection criteria and within the range  $1810 < M(\pi^- \pi^+ \pi^+) < 1930$  MeV/ $c^2$  and  $1910 < M(\pi^- \pi^+ \pi^+) < 2030$  MeV/ $c^2$ , respectively. The signal is described by a sum of two Gaussian functions and the background is represented by a third-order polynomial. The data sample is separated according to magnet polarity and candidate momentum ( $p_{D_{(s)}}^+ < 50$  GeV/c,  $50 < p_{D_{(s)}}^+ < 100$  GeV/c, and  $p_{D_{(s)}}^+ > 100$  GeV/c), to take into account the dependence of the mass resolution on the momentum. The parameters are determined by simultaneous fits to these  $D_{(s)}^+$  and  $D_{(s)}^-$  subsamples.

The  $D^+$  and  $D_s^+$  invariant mass distributions and fit results for the momentum range  $50 < p_{D_{(s)}}^+ < 100$  GeV/c are shown in Fig. 1 for magnet up data. The total yields after summing over all fits are  $(2678 \pm 7) \times 10^3 D^+ \rightarrow \pi^- \pi^+ \pi^+$  and  $(2704 \pm 8) \times 10^3 D^+ \rightarrow \pi^- \pi^+ \pi^+$  decays. The final samples used for the CPV search consist of all candidates with  $M(\pi^- \pi^+ \pi^+)$  within  $\pm 2\sigma$  around  $\bar{m}_{D_{(s)}}$ , where  $\bar{\sigma}$  and  $\bar{m}_{D_{(s)}}$  are the weighted average of the two fitted Gaussian widths and mean values. The values of  $\bar{\sigma}$  range from 8 to 12 MeV/ $c^2$ , depending on the momentum region. For the signal sample there are  $3114 \times 10^3$  candidates, including background, while for the control mode there are  $2938 \times 10^3$  candidates with purities of 82% and 87%, respectively. The purity is defined as the fraction of signal decays in this mass range.

The  $D^+ \rightarrow \pi^- \pi^+ \pi^+$  and  $D^+ \rightarrow \bar{K}^- \pi^+ \pi^+$  Dalitz plots are shown in Fig. 2, with  $s_{\text{low}}$  and  $s_{\text{high}}$  being the lowest and highest invariant mass squared combination,  $M^2(\pi^- \pi^+)$ , respectively. Clear resonant structures are observed in both decay modes.

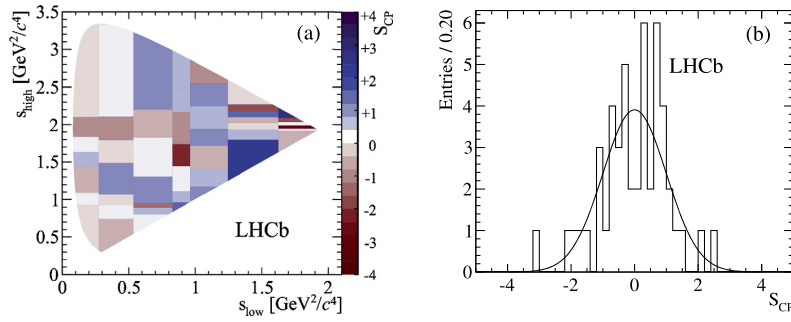


**Fig. 3.** (a) Distribution of  $S_{CP}^i$  with 49  $D_s^+$  adaptive bins of equal population in the  $D_s^+ \rightarrow \pi^- \pi^+ \pi^+$  Dalitz plot and (b) the corresponding one-dimensional distribution (histogram) with a standard normal Gaussian function superimposed (solid line).

#### 4. Binned analysis

##### 4.1. Method

The binned method used to search for localised asymmetries in the  $D^+ \rightarrow \pi^- \pi^+ \pi^+$  decay phase space is based on a bin-by-bin comparison between the  $D^+$  and  $D^-$  Dalitz plots [19,20]. For each bin of the Dalitz plot, the significance of the difference between  $D^+$  and  $D^-$  candidates,  $S_{CP}^i$ , is computed as

$$S_{CP}^i \equiv \frac{N_i^+ - \alpha N_i^-}{\sqrt{\alpha(N_i^+ + N_i^-)}}, \quad \alpha \equiv \frac{N^+}{N^-}, \quad (1)$$

where  $N_i^+$  ( $N_i^-$ ) is the number of  $D^+$  ( $D^-$ ) candidates in the  $i$ th bin and  $N^+$  ( $N^-$ ) is the sum of  $N_i^+$  ( $N_i^-$ ) over all bins. The parameter  $\alpha$  removes the contribution of global asymmetries which may arise due to production [21,22] and detection asymmetries, as well as from  $CPV$ . Two binning schemes are used, a uniform grid with bins of equal size and an adaptive binning where the bins have the same population.

In the absence of localised asymmetries, the  $S_{CP}^i$  values follow a standard normal Gaussian distribution. Therefore,  $CPV$  can be detected as a deviation from this behaviour. The numerical comparison between the  $D^+$  and  $D^-$  Dalitz plots is made by a  $\chi^2$  test, with  $\chi^2 = \sum_i (S_{CP}^i)^2$ . A p-value for the hypothesis of no  $CPV$  is obtained considering that the number of degrees of freedom (ndf) is equal to the total number of bins minus one, due to the constraint on the overall  $D^+/D^-$  normalisation.

A  $CPV$  signal is established if a p-value lower than  $3 \times 10^{-7}$  is found, in which case it can be converted to a significance for the exclusion of  $CP$  symmetry in this channel. If no evidence of  $CPV$  is found, this technique provides no model-independent way to set an upper limit.

##### 4.2. Control mode and background

The search for local asymmetries across the  $D_s^+ \rightarrow \pi^- \pi^+ \pi^+$  Dalitz plot is performed using both the uniform and the adaptive (“ $D_s^+$  adaptive”) binning schemes mentioned previously. A third scheme is also used: a “scaled  $D^+$ ” scheme, obtained from the  $D^+$  adaptive binning by scaling the bin edges by the ratios of the maximum values of  $s_{\text{high}}(D_s^+)/s_{\text{high}}(D^+)$  and  $s_{\text{low}}(D_s^+)/s_{\text{low}}(D^+)$ . This scheme provides a one-to-one mapping of the corresponding Dalitz plots and allows to probe regions in the signal and control channel phase spaces where the momentum distributions of the three final state particles are similar.

The study is performed using  $\alpha = 0.992 \pm 0.001$ , as measured for the  $D_s^+$  sample, and different granularities: 20, 30, 40, 49

and 100 adaptive bins for both the  $D_s^+$  adaptive and scaled  $D^+$  schemes, and  $5 \times 5$ ,  $6 \times 7$ ,  $8 \times 9$  and  $12 \times 12$  bins for the uniform grid scheme. Only bins with a minimum occupancy of 20 entries are considered. The p-values obtained are distributed in the range 4–87%, consistent with the hypothesis of absence of localised asymmetries. As an example, Fig. 3 shows the distributions of  $S_{CP}^i$  for the  $D_s^+$  adaptive binning scheme with 49 bins.

As a further cross-check, the  $D_s^+$  sample is divided according to magnet polarity and hardware trigger configurations. Typically, the p-values are above 1%, although one low value of 0.07% is found for a particular trigger subset of magnet up data with 40 adaptive bins. When combined with magnet down data, the p-value increases to 11%.

The possibility of local asymmetries induced by the background under the  $D^+$  signal peak is studied by considering the candidates with mass  $M(\pi^- \pi^+ \pi^+)$  in the ranges 1810–1835  $\text{MeV}/c^2$  and 1905–1935  $\text{MeV}/c^2$ , for which  $\alpha = 1.000 \pm 0.002$ . Using a uniform grid with four different granularities, the p-values are computed for each of the two sidebands. The data are also divided according to the magnet polarity. The p-values are found to be within 0.4–95.5%, consistent with differences in the number of  $D^+$  and  $D^-$  candidates arising from statistical fluctuations. Since the selection criteria suppress charm background decays to a negligible level, it is assumed that the background contribution to the signal is similar to the sidebands. Therefore, asymmetries eventually observed in the signal mode cannot be attributed to the background.

##### 4.3. Sensitivity studies

To study the  $CPV$  sensitivity of the method for the current data set, a number of simulated pseudo-experiments are performed with sample size and purity similar to that observed in data. The  $D^+ \rightarrow \pi^- \pi^+ \pi^+$  decays are generated according to an amplitude model inspired by E791 results [23], where the most important contributions originate from  $\rho^0(770)\pi^+$ ,  $\sigma(500)\pi^+$  and  $f_2(1270)\pi^+$  resonant modes. Background events are generated evenly in the Dalitz plot. Since no theoretical predictions on the presence or size of  $CPV$  are available for this channel, various scenarios are studied by introducing phase and magnitude differences between the main resonant modes for  $D^+$  and  $D^-$ . The sensitivity for different binning strategies is also evaluated.

Phase differences in the range  $0.5$ – $4.0^\circ$  and magnitude differences in the range 0.5–4.0% are tested for  $\rho^0(770)\pi^+$ ,  $\sigma(500)\pi^+$  and  $f_2(1270)\pi^+$  modes. The study shows a sensitivity (p-values below  $10^{-7}$ ) around  $1^\circ$  to  $2^\circ$  in phase differences and 2% in amplitude in these channels. The sensitivity decreases when the number of bins is larger than 100, so a few tens of bins approaches the optimal choice. A slightly better sensitivity for the adaptive binning strategy is found in most of the studies.

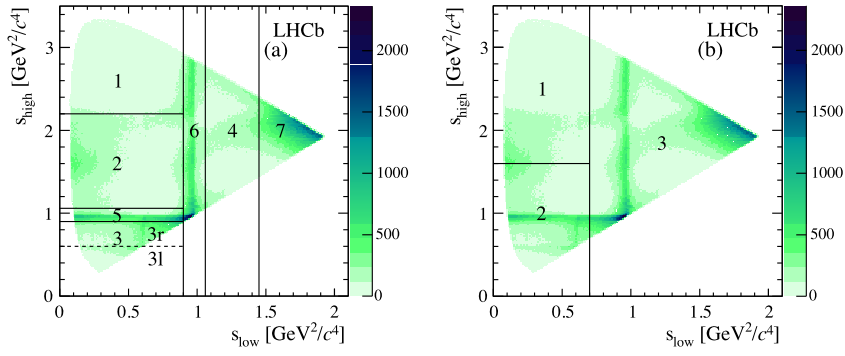


Fig. 4. Dalitz plot for  $D_s^+ \rightarrow \pi^- \pi^+ \pi^+$  control sample decays divided into (a) seven regions R1–R7 and (b) three regions P1–P3. Region R3 is further divided into two regions of  $s_{\text{high}}$  at masses smaller (R3l) and larger (R3r) than the  $\rho^0(770)$  resonance.

Since the presence of background tends to dilute a potential sign of CPV, additional pseudo-experiment studies are made for different scenarios based on signal yields and purities attainable on data. Results show that better sensitivities are found for higher yields, despite the lower purity.

## 5. Unbinned analysis

### 5.1. $k$ -Nearest neighbour analysis technique

The unbinned model-independent method of searching for CPV in many-body decays uses the concept of nearest neighbour events in a combined  $D^+$  and  $D^-$  samples to test whether they share the same parent distribution function [12,13,24]. To find the  $n_k$  nearest neighbour events of each  $D^+$  and  $D^-$  event, the Euclidean distance between points in the Dalitz plot of three-body  $D^+$  and  $D^-$  decays is used. For the whole event sample a test statistic  $T$  for the null hypothesis is calculated,

$$T = \frac{1}{n_k(N_+ + N_-)} \sum_{i=1}^{N_+ + N_-} \sum_{k=1}^{n_k} I(i, k), \quad (2)$$

where  $I(i, k) = 1$  if the  $i$ th event and its  $k$ th nearest neighbour have the same charge and  $I(i, k) = 0$  otherwise and  $N_+$  ( $N_-$ ) is the number of events in the  $D^+$  ( $D^-$ ) sample.

The test statistic  $T$  is the mean fraction of like-charged neighbour pairs in the combined  $D^+$  and  $D^-$  decays sample. The advantage of the  $k$ -nearest neighbour method (kNN), in comparison with other proposed methods for unbinned analyses [24], is that the calculation of  $T$  is simple and fast and the expected distribution of  $T$  is well known: for the null hypothesis it follows a Gaussian distribution with mean  $\mu_T$  and variance  $\sigma_T^2$  calculated from known parameters of the distributions,

$$\mu_T = \frac{N_+(N_+ - 1) + N_-(N_- - 1)}{N(N - 1)}, \quad (3)$$

$$\lim_{N, n_k, D \rightarrow \infty} \sigma_T^2 = \frac{1}{N n_k} \left( \frac{N_+ N_-}{N^2} + 4 \frac{N_+^2 N_-^2}{N^4} \right), \quad (4)$$

where  $N = N_+ + N_-$  and  $D$  is a space dimension. For  $N_+ = N_-$  a reference value

$$\mu_{TR} = \frac{1}{2} \left( \frac{N - 2}{N - 1} \right) \quad (5)$$

is obtained and for a very large number of events  $N$ ,  $\mu_T$  approaches 0.5. However, since the observed deviations of  $\mu_T$  from  $\mu_{TR}$  are sometimes tiny, it is necessary to calculate  $\mu_T - \mu_{TR}$ . The

convergence in Eq. (4) is fast and  $\sigma_T$  can be obtained with a good approximation even for space dimension  $D = 2$  for the current values of  $N_+$ ,  $N_-$  and  $n_k$  [13,24].

The kNN method is applied to search for CPV in a given region of the Dalitz plot in two ways: by looking at a “normalization” asymmetry ( $N_+ \neq N_-$  in a given region) using a pull  $(\mu_T - \mu_{TR})/\Delta(\mu_T - \mu_{TR})$  variable, where the uncertainty on  $\mu_T$  is  $\Delta\mu_T$  and the uncertainty on  $\mu_{TR}$  is  $\Delta\mu_{TR}$ , and looking for a “shape” or particle density function (pdf) asymmetry using another pull  $(T - \mu_T)/\sigma_T$  variable.

As in the binned method, this technique provides no model-independent way to set an upper limit if no CPV is found.

### 5.2. Control mode and background

The Cabibbo-favoured  $D_s^+$  decays serve as a control sample to estimate the size of production and detection asymmetries and systematic effects. The sensitivity for local CPV in the Dalitz plot of the kNN method can be increased by taking into account only events from the region where CPV is expected to be enhanced by the known intermediate resonances in the decays. Since these regions are characterised by enhanced variations of strong phases, the conditions for observation of CPV are more favourable. Events from other regions are expected to only dilute the signal of CPV.

The Dalitz plot for the control channel  $D_s^+ \rightarrow \pi^- \pi^+ \pi^+$  is partitioned into three (P1–P3) or seven (R1–R7) regions shown in Fig. 4. The division R1–R7 is such that regions enriched in resonances are separated from regions dominated by smoother distributions of events. Region R3 is further divided into two regions of  $s_{\text{high}}$  at masses smaller (R3l) and larger (R3r) than the  $\rho^0(770)$  resonance, in order to study possible asymmetries due to a sign change of the strong phase when crossing the resonance pole. The three regions P1–P3 correspond to a more complicated structure of resonances in the signal decay  $D^+ \rightarrow \pi^- \pi^+ \pi^+$  (see Fig. 11).

The value of the test statistic  $T$  measured using the kNN method with  $n_k = 20$  for the full Dalitz plot (called R0) of  $D^+ \rightarrow \pi^- \pi^+ \pi^+$  candidates is compared to the expected Gaussian  $T$  distribution with  $\mu_T$  and  $\sigma_T$  calculated from data. The calculated p-value is 44% for the hypothesis of no CP asymmetry. The p-values are obtained by integrating the Gaussian  $T$  distribution from a given value up to its maximum value of 1. The results are shown in Fig. 5 separately for each region. They do not show any asymmetry between  $D^+$  and  $D^-$  samples. Since no CPV is expected in the control channel, the local detection asymmetries are smaller than the present sensitivity of the kNN method. The production asymmetry is accounted for in the kNN method as a deviation of the measured value of  $\mu_T$  from the

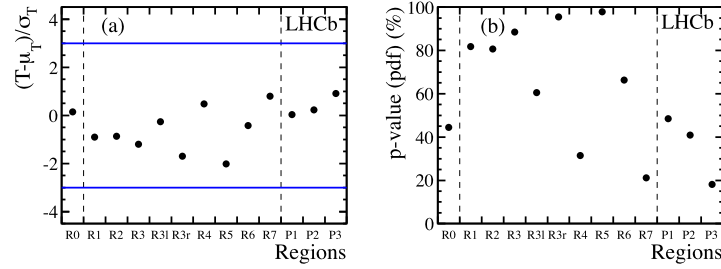


**Fig. 5.** (a) Pull values of  $T$  and (b) the corresponding p-values for  $D_s^+ \rightarrow \pi^- \pi^+ \pi^+$  control sample candidates restricted to each region, obtained using the kNN method with  $n_k = 20$ . The horizontal blue lines in (a) represent  $-3$  and  $+3$  pull values. The region R0 corresponds to the full Dalitz plot. Note that the points for the overlapping regions are correlated.

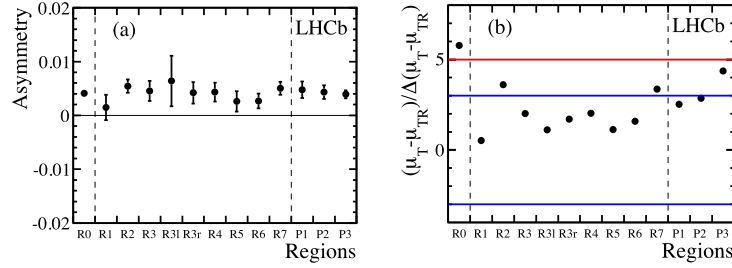


**Fig. 6.** (a) Raw asymmetry  $A = (N_- - N_+) / (N_- + N_+)$  and (b) the pull values of  $\mu_T$  for  $D_s^+ \rightarrow \pi^- \pi^+ \pi^+$  control sample candidates restricted to each region. The horizontal lines in (b) represent  $+3$  and  $+5$  pull values. The region R0 corresponds to the full Dalitz plot. Note that the points for the overlapping regions are correlated.

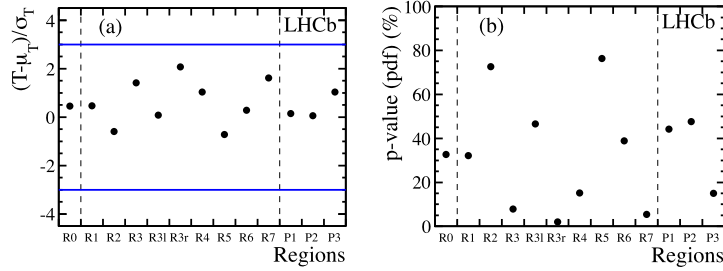


**Fig. 7.** (a) Pull values of  $T$  and (b) the corresponding p-values for the background candidates restricted to each region obtained using the kNN method with  $n_k = 20$ . The horizontal blue lines in (a) represent  $-3$  and  $+3$  pull values. The region R0 corresponds to the full Dalitz plot. Note that the points for the overlapping regions are correlated.

reference value  $\mu_{TR}$ . In the present sample, the obtained value  $\mu_T - 0.5 = (84 \pm 15) \times 10^{-7}$ , with  $(\mu_T - \mu_{TR}) / \Delta(\mu_T - \mu_{TR}) = 5.8\sigma$ , in the full Dalitz plot is a consequence of the observed global asymmetry of about 0.4%. This value is consistent with the previous measurement from LHCb [22]. The comparison of the raw asymmetry  $A = (N_- - N_+) / (N_- + N_+)$  and the pull values of  $\mu_T$  in all regions are presented in Fig. 6. The measured raw asymmetry is similar in all regions as expected for an effect due to the production asymmetry. It is interesting to note the relation  $\mu_T - \mu_{TR} \approx A^2 / 2$  at order  $1/N$  between the raw asymmetry and the parameters of the kNN method.

A region-by-region comparison of  $D_s^+$  candidates for magnet down and magnet up data gives insight into left-right detection asymmetries. No further asymmetries, except for the global production asymmetry discussed above, are found.

The number of nearest neighbour events  $n_k$  is the only parameter of the kNN method. The results for the control channel show no significant dependence of p-values on  $n_k$ . Higher values of  $n_k$  reduce statistical fluctuations due to the local population density and should be preferred. On the other hand, increasing the number of nearest neighbours with limited number of events in the

sample can quickly increase the radius of the local region under investigation.

The kNN method also is applied to the background events, defined in Section 4.2. Contrary to the measurements for the  $D^+ \rightarrow \pi^- \pi^+ \pi^+$  candidates, for background no production asymmetry is observed. The calculated  $\mu_T - 0.5 = (-5.80 \pm 0.46) \times 10^{-7}$  for the full Dalitz plot is very close to the value  $\mu_{TR} - 0.5 = (-5.8239 \pm 0.0063) \times 10^{-7}$  expected for an equal number of events in  $D^+$  and  $D^-$  samples (Eq. (5)). The measured pull values of  $T$  and the corresponding p-values obtained using the kNN method with  $n_k = 20$  are presented for the background in Fig. 7, separately for each region. The comparison of normalisation asymmetries and pull values of  $\mu_T$  in all regions are presented in Fig. 8. All the kNN method results are consistent with no significant asymmetry.

### 5.3. Sensitivity studies

The sensitivity of the kNN method is tested with the same pseudo-experiment model described in Section 4.3. If the simulated asymmetries are spread out in the Dalitz plot the events may be moved from one region to another. For these asymmetries it is

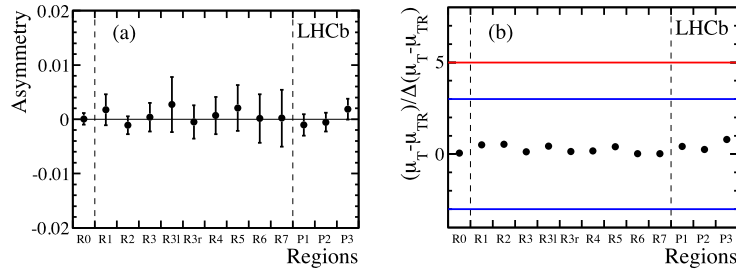


**Fig. 8.** (a) Raw asymmetry and (b) pull value of  $\mu_T$  as a function of a region for the background candidates. The horizontal lines in (b) represent +3 and +5 pull values. The region R0 corresponds to the full Dalitz plot. Note that the points for the overlapping regions are correlated.

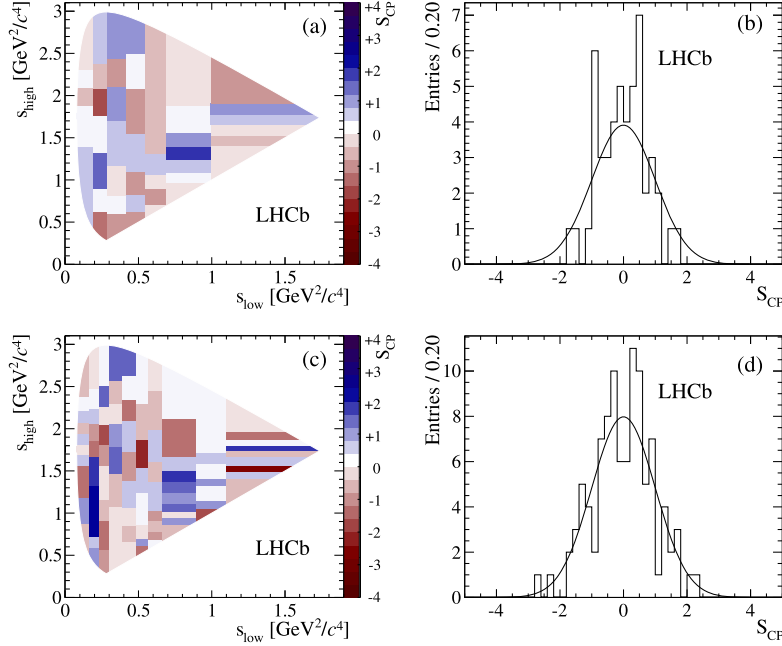


**Fig. 9.** Distributions of  $S_{CP}^i$  across the  $D^+$  Dalitz plane, with the adaptive binning scheme of uniform population for the total  $D^+ \rightarrow \pi^- \pi^+ \pi^+$  data sample with (a) 49 and (c) 100 bins. The corresponding one-dimensional  $S_{CP}^i$  distributions (b) and (d) are shown with a standard normal Gaussian function superimposed (solid line).

observed that the difference in shape of the probability density functions is in large part absorbed in the difference in the normalisation. This indicates that the choice of the regions is important for increasing the sensitivity of the kNN method. In general the method applied in a given region is sensitive to weak phase differences greater than  $(1-2)^\circ$  and magnitude differences of  $(2-4)\%$ .

## 6. Results

### 6.1. Binned method

The search for CPV in the Cabibbo-suppressed mode  $D^+ \rightarrow \pi^- \pi^+ \pi^+$  is pursued following the strategy described in Section 4. For the total sample size of about 3.1 million  $D^+$  and  $D^-$  candidates, the normalisation factor  $\alpha$ , defined in Eq. (1), is  $0.990 \pm 0.001$ . Both adaptive and uniform binning schemes in the Dalitz plot are used for different binning sizes.

The  $S_{CP}^i$  values across the Dalitz plot and the corresponding histogram for the adaptive binning scheme with 49 and 100 bins are illustrated in Fig. 9. The p-values for these and other binning

**Table 1**

Results for the  $D^+ \rightarrow \pi^- \pi^+ \pi^+$  decay sample using the adaptive binning scheme with different numbers of bins. The number of degrees of freedom is the number of bins minus 1.

Number of bins	$\chi^2$	p-value (%)
20	14.0	78.1
30	28.2	50.6
40	28.5	89.2
49	26.7	99.5
100	89.1	75.1

choices are shown in Table 1. All p-values show statistical agreement between the  $D^+$  and  $D^-$  samples.

The same  $\chi^2$  test is performed for the uniform binning scheme, using 20, 32, 52 and 98 bins also resulting in p-values consistent with the null hypothesis, all above 90%. The  $S_{CP}^i$  distribution in the Dalitz plot for 98 bins and the corresponding histogram is shown in Fig. 10.

As consistency checks, the analysis is repeated with independent subsamples obtained by separating the total sample accord-

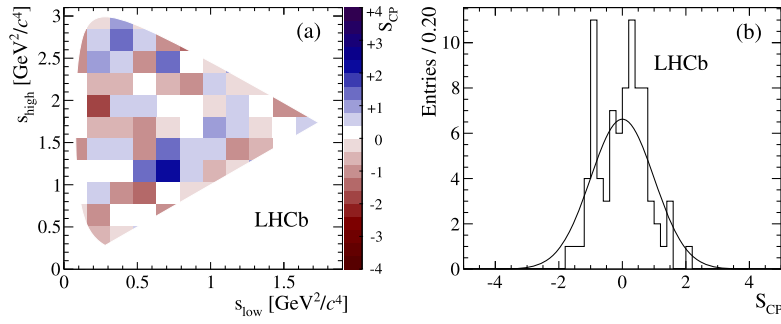


**Fig. 10.** (a) Distribution of  $S_{CP}^i$  with 98 bins in the uniform binning scheme for the total  $D^+ \rightarrow \pi^- \pi^+ \pi^+$  data sample and (b) the corresponding one-dimensional  $S_{CP}^i$  distribution (b) with a standard normal Gaussian function superimposed (solid line).

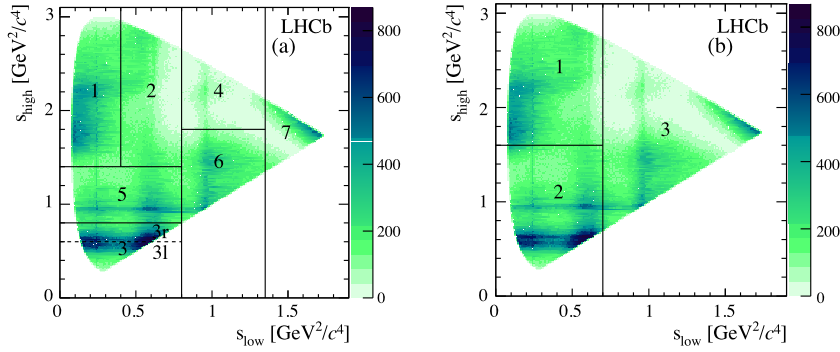


**Fig. 11.** Dalitz plot for  $D^+ \rightarrow \pi^- \pi^+ \pi^+$  candidates divided into (a) seven regions R1–R7 and (b) three regions P1–P3.

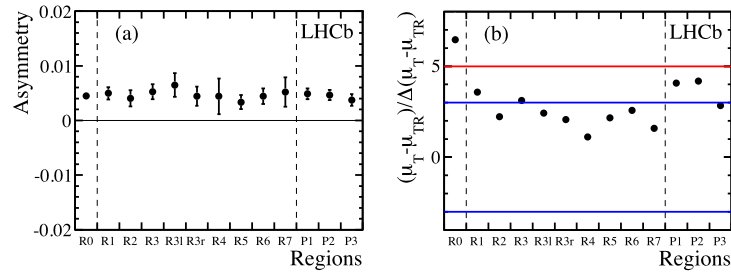


**Fig. 12.** (a) Raw asymmetry and (b) the pull values of  $\mu_T$  for  $D^+ \rightarrow \pi^- \pi^+ \pi^+$  candidates restricted to each region. The horizontal lines in (b) represent pull values  $+3$  and  $+5$ . The region R0 corresponds to the full Dalitz plot. Note that the points for the overlapping regions are correlated.

ing to magnet polarity, hardware trigger configurations, and data-taking periods. The resulting p-values range from 0.3% to 98.3%.

All the results above indicate the absence of CPV in the  $D^+ \rightarrow \pi^- \pi^+ \pi^+$  channel at the current analysis sensitivity.

## 6.2. Unbinned method

The kNN method is applied to the Cabibbo-suppressed mode  $D^+ \rightarrow \pi^- \pi^+ \pi^+$  with the two region definitions shown in Fig. 11. To account for the different resonance structure in  $D^+$  and  $D^0$  decays, the region R1–R7 definition for the signal mode is different from the definition used in the control mode (compare Figs. 4(a) and 11(a)). The region P1–P3 definitions are the same. The results for the raw asymmetry are shown in Fig. 12. The production asymmetry is clearly visible in all the regions with the same magnitude as in the control channel (see Fig. 6). It is accounted for in the kNN method as a deviation of the measured value of  $\mu_T$  from the ref-

erence value  $\mu_{TR}$  shown in Fig. 12. In the signal sample the values  $\mu_T - 0.5 = (98 \pm 15) \times 10^{-7}$  and  $(\mu_T - \mu_{TR}) / \Delta(\mu_T - \mu_{TR}) = 6.5\sigma$  in the full Dalitz plot are a consequence of the 0.4% global asymmetry similar to that observed in the control mode and consistent with the previous measurement from LHCb [21].

The pull values of  $T$  and the corresponding p-values for the hypothesis of no CPV are shown in Fig. 13 for the same regions. To check for any systematic effects, the test is repeated for samples separated according to magnet polarity. Since the sensitivity of the method increases with  $n_k$ , the analysis is repeated with  $n_k = 500$  for all the regions. All p-values are above 20%, consistent with no CP asymmetry in the signal mode.

## 7. Conclusion

A search for CPV in the decay  $D^+ \rightarrow \pi^- \pi^+ \pi^+$  is performed using  $pp$  collision data corresponding to an integrated luminosity

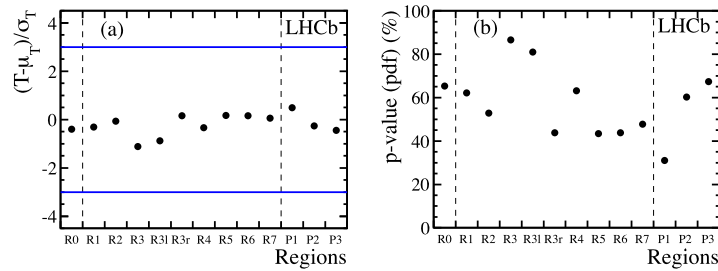


**Fig. 13.** (a) Pull values of  $T$  and (b) the corresponding  $p$ -values for  $D^+ \rightarrow \pi^- \pi^+ \pi^+$  candidates restricted to each region obtained using the kNN method with  $n_k = 20$ . The horizontal blue lines in (a) represent pull values  $-3$  and  $+3$ . The region R0 corresponds to the full Dalitz plot. Note that the points for the overlapping regions are correlated.

of  $1.0 \text{ fb}^{-1}$  collected by the LHCb experiment at a centre-of-mass energy of 7 TeV. Two model-independent methods are applied to a sample of 3.1 million  $D^+ \rightarrow \pi^- \pi^+ \pi^+$  decay candidates with 82% signal purity.

The binned method is based on the study of the local significances  $S_{CP}^i$  in bins of the Dalitz plot, while the unbinned method uses the concept of nearest neighbour events in the pooled  $D^+$  and  $D^-$  sample. Both methods are also applied to the Cabibbo-favoured  $D^+ \rightarrow \frac{2}{3} \pi^- \pi^+ \pi^+$  decay and to the mass sidebands to control possible asymmetries not originating from  $CPV$ .

No single bin in any of the binning schemes presents an absolute  $S_{CP}^i$  value larger than 3. Assuming no  $CPV$ , the probabilities of observing local asymmetries across the phase-space of the  $D^+$  meson decay as large or larger than those in data are above 50% in all the tested binned schemes. In the unbinned method, the  $p$ -values are above 30%. All results are consistent with no  $CPV$ .

#### Acknowledgements

We express our gratitude to our colleagues in the CERN accelerator departments for the excellent performance of the LHC. We thank the technical and administrative staff at the LHCb institutes. We acknowledge support from CERN and from the national agencies: CAPES, CNPq, FAPERJ and FINEP (Brazil); NSFC (China); CNRS/IN2P3 and Region Auvergne (France); BMBF, DFG, HGF and MPG (Germany); SFI (Ireland); INFN (Italy); FOM and NWO (The Netherlands); SCSR (Poland); MEN/IFA (Romania); MinES, Rosatom, RFBR and NRC “Kurchatov Institute” (Russia); MinECo, XuntaGal and GENCAT (Spain); SNSF and SER (Switzerland); NAS Ukraine (Ukraine); STFC (United Kingdom); NSF (USA). We also acknowledge the support received from the ERC under FP7. The Tier1 computing centres are supported by IN2P3 (France), KIT and BMBF (Germany), INFN (Italy), NWO and SURF (The Netherlands), PIC (Spain), GridPP (United Kingdom). We are thankful for the computing resources put at our disposal by Yandex LLC (Russia), as well as to the communities behind the multiple open source software packages that we depend on.

#### References

- [1] J. Brod, Y. Grossman, A.L. Kagan, J. Zupan, A consistent picture for large penguins in  $D^0 \rightarrow \pi^+ \pi^-, K^+ K^-$ , J. High Energy Phys. 1210 (2012) 161, arXiv:1203.6659.
- [2] J. Brod, A.L. Kagan, J. Zupan, Size of direct CP violation in singly Cabibbo-suppressed D decays, Phys. Rev. D 86 (2012) 014023, arXiv:1111.5000.

#### LHCb Collaboration

R. Aaij<sup>40</sup>, B. Adeva<sup>36</sup>, M. Adinolfi<sup>45</sup>, C. Adrover<sup>6</sup>, A. Affolder<sup>51</sup>, Z. Ajaltouni<sup>5</sup>, J. Albrecht<sup>9</sup>, F. Alessio<sup>37</sup>, M. Alexander<sup>50</sup>, S. Ali<sup>40</sup>, G. Alkhazov<sup>29</sup>, P. Alvarez Cartelle<sup>36</sup>, A.A. Alves Jr.<sup>24</sup>, S. Amato<sup>2</sup>, S. Amerio<sup>21</sup>,

- [3] B. Bhattacharya, M. Gronau, J.L. Rosner, CP asymmetries in singly-Cabibbo-suppressed D decays to two pseudoscalar mesons, Phys. Rev. D 85 (2012) 054014, arXiv:1201.2351.
- [4] LHCb Collaboration, R. Aaij, et al., and A. Bharucha, et al., Implications of LHCb measurements and future prospects, Eur. Phys. J. C 73 (2013) 2373, arXiv:1208.3355.
- [5] LHCb Collaboration, R. Aaij, et al., Search for CP violation in the  $D^+ \rightarrow \phi \pi^+$  and  $D^+ \rightarrow K_S^0 \pi^+$  decays, J. High Energy Phys. 1306 (2013) 112, arXiv:1303.4906.
- [6] LHCb Collaboration, A search for time-integrated CP violation in  $D^0 \rightarrow K^- K^+$  and  $D^0 \rightarrow \pi^- \pi^+$  decays, LHCb-CONF-2013-003.
- [7] CDF Collaboration, T. Aaltonen, et al., Measurement of the difference in CP-violating asymmetries in  $D^0 \rightarrow K^+ K^-$  and  $D^0 \rightarrow \pi^+ \pi^-$  decays at CDF, Phys. Rev. Lett. 109 (2012) 111801, arXiv:1207.2158.
- [8] LHCb Collaboration, R. Aaij, et al., Measurement of  $D^0$ - $\bar{D}^0$  mixing parameters and search for CP violation using  $D^0 \rightarrow K^+ \pi^-$  decays, Phys. Rev. Lett., in press, arXiv:1309.6534.
- [9] LHCb Collaboration, R. Aaij, et al., Measurements of indirect CP violation in  $D^0 \rightarrow K^- K^+$  and  $D^0 \rightarrow \pi^- \pi^+$  decays, Phys. Rev. Lett., in press, arXiv:1310.7201.
- [10] LHCb Collaboration, R. Aaij, et al., Search for CP violation in  $D^+ \rightarrow K^- K^+ \pi^+$  decays, Phys. Rev. D 84 (2011) 112008, arXiv:1110.3970.
- [11] LHCb Collaboration, R. Aaij, et al., Model-independent search for CP violation in  $D^0 \rightarrow K^- K^+ \pi^+ \pi^-$  and  $D^0 \rightarrow \pi^- \pi^+ \pi^- \pi^+$  decays, Phys. Lett. B 726 (2013) 623, arXiv:1308.3189.
- [12] N. Henze, A multivariate two-sample test based on the number of nearest neighbor type coincidences, Ann. Stat. 16 (2) (1988) 772.
- [13] M.F. Schilling, Multivariate two-sample tests based on nearest neighbors, J. Am. Stat. Assoc. 81 (1986) 799.
- [14] LHCb Collaboration, A.A. Alves Jr., et al., The LHCb detector at the LHC, J. Instrum. 3 (2008) S08005.
- [15] M. Adinolfi, et al., Performance of the LHCb RICH detector at the LHC, Eur. Phys. J. C 73 (2013) 2431, arXiv:1211.6759.
- [16] A.A. Alves Jr., et al., Performance of the LHCb muon system, J. Instrum. 8 (2013) P02022, arXiv:1211.1346.
- [17] R. Aaij, et al., The LHCb trigger and its performance in 2011, J. Instrum. 8 (2013) P04022, arXiv:1211.3055.
- [18] F. Archilli, et al., Performance of the muon identification at LHCb, J. Instrum. 8 (2013) P10020, arXiv:1306.0249.
- [19] I. Bediaga, et al., On a CP anisotropy measurement in the Dalitz plot, Phys. Rev. D 80 (2009) 096006, arXiv:0905.4233.
- [20] BaBar Collaboration, B. Aubert, et al., Search for CP violation in neutral D meson Cabibbo-suppressed three-body decays, Phys. Rev. D 78 (2008) 051102, arXiv:0802.4035.
- [21] LHCb Collaboration, R. Aaij, et al., Measurement of the  $D^+$  production asymmetry in 7 TeV  $pp$  collisions, Phys. Lett. B 718 (2013) 902–909, arXiv:1210.4112.
- [22] LHCb Collaboration, R. Aaij, et al., Measurement of the  $D^+ \rightarrow D^-$  production asymmetry in 7 TeV  $pp$  collisions, Phys. Lett. B 713 (2012) 186, arXiv:1205.0897.
- [23] Fermilab E791 Collaboration, E.M. Aitala, et al., Experimental evidence for a light and broad scalar resonance in  $D^+ \rightarrow \pi^- \pi^+ \pi^+$  decay, Phys. Rev. Lett. 86 (2001) 770, arXiv:hep-ex/0007028.
- [24] M. Williams, How good are your fits? Unbinned multivariate goodness-of-fit tests in high energy physics, J. Instrum. 5 (2010) P09004, arXiv:1006.3019.

Y. Amhis<sup>7</sup>, L. Anderlini<sup>17,f</sup>, J. Anderson<sup>39</sup>, R. Andreassen<sup>56</sup>, M. Andreotti<sup>16,e</sup>, J.E. Andrews<sup>57</sup>, R.B. Appleby<sup>53</sup>, O. Aquines Gutierrez<sup>10</sup>, F. Archilli<sup>18</sup>, A. Artamonov<sup>34</sup>, M. Artuso<sup>58</sup>, E. Aslanides<sup>6</sup>, G. Auremma<sup>24,m</sup>, M. Baalouch<sup>5</sup>, S. Bachmann<sup>11</sup>, J.J. Back<sup>47</sup>, A. Badalov<sup>35</sup>, C. Baesso<sup>59</sup>, V. Balagura<sup>30</sup>, W. Baldini<sup>16</sup>, R.J. Barlow<sup>53</sup>, C. Barschel<sup>37</sup>, S. Barsuk<sup>7</sup>, W. Barter<sup>46</sup>, V. Batozskaya<sup>27</sup>, Th. Bauer<sup>40</sup>, A. Bay<sup>38</sup>, J. Beddow<sup>50</sup>, F. Bedeschi<sup>22</sup>, I. Bediaga<sup>1</sup>, S. Belogurov<sup>30</sup>, K. Belous<sup>34</sup>, I. Belyaev<sup>30</sup>, E. Ben-Haim<sup>8</sup>, G. Bencivenni<sup>18</sup>, S. Benson<sup>49</sup>, J. Benton<sup>45</sup>, A. Berezhnoy<sup>31</sup>, R. Bernet<sup>39</sup>, M.-O. Bettler<sup>46</sup>, M. van Beuzekom<sup>40</sup>, A. Bien<sup>11</sup>, S. Bifani<sup>44</sup>, T. Bird<sup>53</sup>, A. Bizzeti<sup>17,h</sup>, P.M. Bjørnstad<sup>53</sup>, T. Blake<sup>47</sup>, F. Blanc<sup>38</sup>, J. Blouw<sup>10</sup>, S. Blusk<sup>58</sup>, V. Bocci<sup>24</sup>, A. Bondar<sup>33</sup>, N. Bondar<sup>29</sup>, W. Bonivento<sup>15</sup>, S. Borghi<sup>53</sup>, A. Borgia<sup>58</sup>, T.J.V. Bowcock<sup>51</sup>, E. Bowen<sup>39</sup>, C. Bozzi<sup>16</sup>, T. Brambach<sup>9</sup>, J. vandenBrand<sup>41</sup>, J. Bressieux<sup>38</sup>, D. Brett<sup>53</sup>, M. Britsch<sup>10</sup>, T. Britton<sup>58</sup>, N.H. Brook<sup>45</sup>, H. Brown<sup>51</sup>, A. Bursche<sup>39</sup>, G. Busetto<sup>21,q</sup>, J. Buytaert<sup>37</sup>, S. Cadeddu<sup>15</sup>, R. Calabrese<sup>16,e</sup>, O. Callot<sup>7</sup>, M. Calvi<sup>20,j</sup>, M. Calvo Gomez<sup>35,n</sup>, A. Camboni<sup>35</sup>, P. Campana<sup>18,37</sup>, D. Campora Perez<sup>37</sup>, A. Carbone<sup>14,c</sup>, G. Carboni<sup>23,k</sup>, R. Cardinale<sup>19,i</sup>, A. Cardini<sup>15</sup>, H. Carranza-Mejia<sup>49</sup>, L. Carson<sup>52</sup>, K. Carvalho Akiba<sup>2</sup>, G. Casse<sup>51</sup>, L. Castillo Garcia<sup>37</sup>, M. Cattaneo<sup>37</sup>, Ch. Cauet<sup>9</sup>, R. Cenci<sup>57</sup>, M. Charles<sup>8</sup>, Ph. Charpentier<sup>37</sup>, S.-F. Cheung<sup>54</sup>, N. Chiapolini<sup>39</sup>, M. Chrzaszcz<sup>39,25</sup>, K. Ciba<sup>37</sup>, X. Cid Vidal<sup>37</sup>, G. Ciezarek<sup>52</sup>, P.E.L. Clarke<sup>49</sup>, M. Clemencic<sup>37</sup>, H.V. Cliff<sup>46</sup>, J. Closier<sup>37</sup>, C. Coca<sup>28</sup>, V. Coco<sup>40</sup>, J. Cogan<sup>6</sup>, E. Cogneras<sup>5</sup>, P. Collins<sup>37</sup>, A. Comerma-Montells<sup>35</sup>, A. Contu<sup>15,37</sup>, A. Cook<sup>45</sup>, M. Coombes<sup>45</sup>, S. Coquereau<sup>8</sup>, G. Corti<sup>37</sup>, B. Couturier<sup>37</sup>, G.A. Cowan<sup>49</sup>, D.C. Craik<sup>47</sup>, S. Cunliffe<sup>52</sup>, R. Currie<sup>49</sup>, C. D'Ambrosio<sup>37</sup>, J. Dalseno<sup>45</sup>, P. David<sup>8</sup>, P.N.Y. David<sup>40</sup>, A. Davis<sup>56</sup>, I. De Bonis<sup>4</sup>, K. De Bruyn<sup>40</sup>, S. De Capua<sup>53</sup>, M. De Cian<sup>11</sup>, J.M. De Miranda<sup>1</sup>, L. De Paula<sup>2</sup>, W. De Silva<sup>56</sup>, P. De Simone<sup>18</sup>, D. Decamp<sup>4</sup>, M. Deckenhoff<sup>9</sup>, L. DelBuono<sup>8</sup>, N. Déleage<sup>4</sup>, D. Derkach<sup>54</sup>, O. Deschamps<sup>5</sup>, F. Dettori<sup>41</sup>, A. DiCanto<sup>11</sup>, H. Dijkstra<sup>37</sup>, M. Dogaru<sup>28</sup>, S. Donleavy<sup>51</sup>, F. Dordei<sup>11</sup>, A. Dosil Suárez<sup>36</sup>, D. Dossett<sup>47</sup>, A. Dovbnya<sup>42</sup>, F. Dupertuis<sup>38</sup>, P. Durante<sup>37</sup>, R. Dzhelyadin<sup>34</sup>, A. Dziurda<sup>25</sup>, A. Dzyuba<sup>29</sup>, S. Easo<sup>48</sup>, U. Egede<sup>52</sup>, V. Egorychev<sup>30</sup>, S. Eidelman<sup>33</sup>, D. van Eijk<sup>40</sup>, S. Eisenhardt<sup>49</sup>, U. Eitschberger<sup>9</sup>, R. Ekelhof<sup>9</sup>, L. Eklund<sup>50,37</sup>, I. El Rifai<sup>5</sup>, Ch. Elsasser<sup>39</sup>, A. Falabella<sup>14,e</sup>, C. Färber<sup>11</sup>, C. Farinelli<sup>40</sup>, S. Farry<sup>51</sup>, D. Ferguson<sup>49</sup>, V. Fernandez Albor<sup>36</sup>, F. Ferreira Rodrigues<sup>17</sup>, M. Ferro-Luzzi<sup>37</sup>, S. Filippov<sup>32</sup>, M. Fiore<sup>16,e</sup>, M. Fiorini<sup>16,e</sup>, C. Fitzpatrick<sup>37</sup>, M. Fontana<sup>10</sup>, F. Fontanelli<sup>19,i</sup>, R. Forty<sup>37</sup>, O. Francisco<sup>2</sup>, M. Frank<sup>37</sup>, C. Frei<sup>37</sup>, M. Frosini<sup>17,37,f</sup>, E. Furaro<sup>23,k</sup>, A. Gallas Torreira<sup>36</sup>, D. Galli<sup>14,c</sup>, M. Gandelman<sup>2</sup>, P. Gandini<sup>58</sup>, Y. Gao<sup>3</sup>, J. Garofoli<sup>58</sup>, P. Garosi<sup>53</sup>, J. Garratino<sup>46</sup>, L. Garrido<sup>35</sup>, C. Gaspar<sup>37</sup>, R. Gauld<sup>54</sup>, E. Gersabeck<sup>11</sup>, M. Gersabeck<sup>53</sup>, T. Gershon<sup>47</sup>, Ph. Ghez<sup>4</sup>, V. Gibson<sup>46</sup>, L. Giubega<sup>28</sup>, V.V. Gligorov<sup>37</sup>, C. Göbel<sup>59</sup>, D. Golubkov<sup>30</sup>, A. Golutvin<sup>52,30,37</sup>, A. Gomes<sup>2</sup>, P. Gorbounov<sup>30,37</sup>, H. Gordon<sup>37</sup>, M. Grabalosa Gándara<sup>5</sup>, R. Graciani Diaz<sup>35</sup>, L.A. Granado Cardoso<sup>37</sup>, E. Graugés<sup>35</sup>, G. Graziani<sup>17</sup>, A. Greco<sup>28</sup>, E. Greening<sup>54</sup>, S. Gregson<sup>46</sup>, P. Griffith<sup>44</sup>, L. Grillo<sup>11</sup>, O. Grünberg<sup>60</sup>, B. Gui<sup>58</sup>, E. Gushchin<sup>32</sup>, Yu. Guz<sup>34,37</sup>, T. Gys<sup>37</sup>, C. Hadjivasiliou<sup>58</sup>, G. Haefeli<sup>38</sup>, C. Haen<sup>37</sup>, T.W. Hafkenscheid<sup>61</sup>, S.C. Haines<sup>46</sup>, S. Hall<sup>52</sup>, B. Hamilton<sup>57</sup>, T. Hampson<sup>45</sup>, S. Hansmann-Menzemer<sup>11</sup>, N. Harnew<sup>54</sup>, S.T. Harnew<sup>45</sup>, J. Harrison<sup>53</sup>, T. Hartmann<sup>60</sup>, J. He<sup>37</sup>, T. Head<sup>37</sup>, V. Heijne<sup>40</sup>, K. Hennessy<sup>51</sup>, P. Henrard<sup>5</sup>, J.A. Hernando Morata<sup>36</sup>, E. van Herwijnen<sup>37</sup>, M. Heß<sup>60</sup>, A. Hicheur<sup>1</sup>, E. Hicks<sup>51</sup>, D. Hill<sup>54</sup>, M. Hoballah<sup>5</sup>, C. Hombach<sup>53</sup>, W. Hulsbergen<sup>40</sup>, P. Hunt<sup>54</sup>, T. Huse<sup>51</sup>, N. Hussain<sup>54</sup>, D. Hutchcroft<sup>51</sup>, D. Hynds<sup>50</sup>, V. Iakovenko<sup>43</sup>, M. Idzik<sup>26</sup>, P. Ilten<sup>12</sup>, R. Jacobsson<sup>37</sup>, A. Jaeger<sup>11</sup>, E. Jans<sup>40</sup>, P. Jaton<sup>38</sup>, A. Jawahery<sup>57</sup>, F. Jing<sup>3</sup>, M. John<sup>54</sup>, D. Johnson<sup>54</sup>, C.R. Jones<sup>46</sup>, C. Joram<sup>37</sup>, B. Jost<sup>37</sup>, M. Kabbalo<sup>9</sup>, S. Kandybei<sup>42</sup>, W. Kanso<sup>6</sup>, M. Karacson<sup>37</sup>, T.M. Karbach<sup>37</sup>, I.R. Kenyon<sup>44</sup>, T. Ketel<sup>41</sup>, B. Khanji<sup>20</sup>, O. Kochebina<sup>7</sup>, I. Komarov<sup>38</sup>, R.F. Koopman<sup>41</sup>, P. Koppenburg<sup>40</sup>, M. Korolev<sup>31</sup>, A. Kozlinskiy<sup>40</sup>, L. Kravchuk<sup>32</sup>, K. Kreplin<sup>11</sup>, M. Krepis<sup>47</sup>, G. Krocker<sup>11</sup>, P. Krokovny<sup>33</sup>, F. Kruse<sup>9</sup>, M. Kucharczyk<sup>20,25,37,j</sup>, V. Kudryavtsev<sup>33</sup>, K. Kurek<sup>27</sup>, T. Kvaratskheliya<sup>30,37</sup>,

E. Maurice<sup>6</sup>, A. Mazurov<sup>16,37,e</sup>, M. McCann<sup>52</sup>, J. McCarthy<sup>44</sup>, A. McNab<sup>53</sup>, R. M. C. Nulty<sup>12</sup>, B. M. C. Skelly<sup>51</sup>, B. Meadows<sup>56,54</sup>, F. Meier<sup>9</sup>, M. Meissner<sup>11</sup>, M. Merk<sup>40</sup>, D. A. Milanes<sup>8</sup>, M.-N. Minard<sup>4</sup>, J. Molina Rodriguez<sup>59</sup>, S. Monteil<sup>5</sup>, D. Moran<sup>53</sup>, P. Morawski<sup>25</sup>, A. Morodà<sup>6</sup>, M. J. Morello<sup>22,s</sup>, R. Mountain<sup>58</sup>, I. Mous<sup>40</sup>, F. Muheim<sup>49</sup>, K. Müller<sup>39</sup>, R. Muresan<sup>28</sup>, B. Mury<sup>26</sup>, B. Muster<sup>38</sup>, P. Naik<sup>45</sup>, T. Nakada<sup>38</sup>, R. Nandakumar<sup>48</sup>, I. Nasteva<sup>1</sup>, M. Needham<sup>49</sup>, S. Neubert<sup>37</sup>, N. Neufeld<sup>37</sup>, A. D. Nguyen<sup>38</sup>, T. D. Nguyen<sup>38</sup>, C. Nguyen-Mau<sup>38,o</sup>, M. Nicol<sup>7</sup>, V. Niess<sup>5</sup>, R. Niet<sup>9</sup>, N. Nikitin<sup>31</sup>, T. Nikodem<sup>11</sup>, A. Nomerotski<sup>54</sup>, A. Novoselov<sup>34</sup>, A. Oblakowska-Mucha<sup>26</sup>, V. Obraztsov<sup>34</sup>, S. Oggero<sup>40</sup>, S. Ogilvy<sup>50</sup>, O. Okhrimenko<sup>43</sup>, R. Oldeman<sup>15,d</sup>, G. Onderwater<sup>61</sup>, M. Orlandea<sup>28</sup>, J. M. Otalora Goicochea<sup>2</sup>, P. Owen<sup>52</sup>, A. Oyanguren<sup>35</sup>, B. K. Pal<sup>58</sup>, A. Palano<sup>13,b</sup>, M. Palutan<sup>18</sup>, J. Panman<sup>37</sup>, A. Papanestis<sup>48</sup>, M. Pappagallo<sup>50</sup>, C. Parkes<sup>53</sup>, C. J. Parkinson<sup>52</sup>, G. Passaleva<sup>17</sup>, G. D. Patel<sup>51</sup>, M. Patel<sup>52</sup>, C. Patrignani<sup>19,i</sup>, C. Pavel-Nicorescu<sup>28</sup>, A. Pazos Alvarez<sup>36</sup>, A. Pearce<sup>53</sup>, A. Pellegrino<sup>40</sup>, G. Pensio<sup>24,l</sup>, M. Pepe Altarelli<sup>37</sup>, S. Perazzini<sup>14,c</sup>, E. Perez Trigo<sup>36</sup>, A. Pérez-Calero Yzquierdo<sup>35</sup>, P. Perret<sup>5</sup>, M. Perrin-Terrin<sup>6</sup>, L. Pescatore<sup>44</sup>, E. Pesen<sup>62</sup>, G. Pessina<sup>20</sup>, K. Petridis<sup>52</sup>, A. Petrolini<sup>19,i</sup>, E. Picatoste Olloqui<sup>35</sup>, B. Pietrzyk<sup>4</sup>, T. Pilař<sup>47</sup>, D. Pinci<sup>24</sup>, S. Playfer<sup>49</sup>, M. Plo Casasus<sup>36</sup>, F. Polci<sup>8</sup>, G. Polok<sup>25</sup>, A. Poluektov<sup>47,33</sup>, E. Polycarpo<sup>2</sup>, A. Popov<sup>34</sup>, D. Popov<sup>10</sup>, B. Popovici<sup>28</sup>, C. Potterat<sup>35</sup>, A. Powell<sup>54</sup>, J. Prisciandaro<sup>38</sup>, A. Pritchard<sup>51</sup>, C. Prouve<sup>7</sup>, V. Pugatch<sup>43</sup>, A. Puig Navarro<sup>38</sup>, G. Punzi<sup>22,r</sup>, W. Qian<sup>4</sup>, B. Rachwal<sup>25</sup>, J. H. Rademacker<sup>45</sup>, B. Rakotomiaramanana<sup>38</sup>, M. S. Rangel<sup>2</sup>, I. Raniuk<sup>42</sup>, N. Rauschmayr<sup>37</sup>, G. Raven<sup>41</sup>, S. Redford<sup>54</sup>, S. Reichert<sup>53</sup>, M. M. Reid<sup>47</sup>, A. C. dos Reis<sup>1</sup>, S. Ricciardi<sup>48</sup>, A. Richards<sup>52</sup>, K. Rinnert<sup>51</sup>, V. Rives Molina<sup>35</sup>, D. A. Roa Romero<sup>5</sup>, P. Robbe<sup>7</sup>, D. A. Roberts<sup>57</sup>, A. B. Rodrigues<sup>1</sup>, E. Rodrigues<sup>53</sup>, P. Rodriguez Perez<sup>36</sup>, S. Roiser<sup>37</sup>, V. Romanovsky<sup>34</sup>, A. Romero Vidal<sup>36</sup>, M. Rotondo<sup>21</sup>, J. Rouvinet<sup>38</sup>, T. Ruf<sup>37</sup>, F. Ruffini<sup>22</sup>, H. Ruiz<sup>35</sup>, P. Ruiz Valls<sup>35</sup>, G. Sabatino<sup>24,k</sup>, J. J. Saborido Silva<sup>36</sup>, N. Sagidova<sup>29</sup>, P. Sail<sup>50</sup>, B. Saitta<sup>15,d</sup>, V. Salustino Guimaraes<sup>2</sup>, B. Sanmartin Sedes<sup>36</sup>, R. Santacesaria<sup>24</sup>, C. Santamarina Rios<sup>36</sup>, E. Santovetti<sup>23,k</sup>, M. Sapunov<sup>6</sup>, A. Sarti<sup>18</sup>, C. Satriano<sup>24,m</sup>, A. Satta<sup>23</sup>, M. Savrie<sup>16,e</sup>, D. Savrina<sup>30,31</sup>, M. Schiller<sup>41</sup>, H. Schindler<sup>37</sup>, M. Schlupp<sup>9</sup>, M. Schmelling<sup>10</sup>, B. Schmidt<sup>37</sup>, O. Schneider<sup>38</sup>, A. Schopper<sup>37</sup>, M.-H. Schune<sup>7</sup>, R. Schwemmer<sup>37</sup>, B. Sciascia<sup>18</sup>, A. Sciubba<sup>24</sup>, M. Seco<sup>36</sup>, A. Semennikov<sup>30</sup>, K. Senderowska<sup>26</sup>, I. Sepp<sup>52</sup>, N. Serra<sup>39</sup>, J. Serrano<sup>6</sup>, P. Seyfert<sup>11</sup>, M. Shapkin<sup>34</sup>, I. Shapoval<sup>16,42,e</sup>, Y. Shcheglov<sup>29</sup>, T. Shears<sup>51</sup>, L. Shekhtman<sup>33</sup>, O. Shevchenko<sup>42</sup>, V. Shevchenko<sup>30</sup>, A. Shires<sup>9</sup>, R. Silva Coutinho<sup>47</sup>, M. Sirendi<sup>46</sup>, N. Skidmore<sup>45</sup>, T. Skwarnicki<sup>58</sup>, N. A. Smith<sup>51</sup>, E. Smith<sup>54,48</sup>, E. Smith<sup>52</sup>, J. Smith<sup>46</sup>, M. Smith<sup>53</sup>, M. D. Sokoloff<sup>56</sup>, F. J. P. Soler<sup>50</sup>, F. Soomro<sup>38</sup>, D. Souza<sup>45</sup>, B. Souza De Paula<sup>2</sup>, B. Spaan<sup>9</sup>, A. Sparke<sup>49</sup>, P. Spradlin<sup>50</sup>, F. Stagni<sup>37</sup>, S. Stahl<sup>11</sup>, O. Steinkamp<sup>39</sup>, S. Stevenson<sup>54</sup>, S. Stoica<sup>28</sup>, S. Stone<sup>58</sup>, B. Storaci<sup>39</sup>, S. Stracka<sup>22,37</sup>, M. Straticiu<sup>28</sup>, U. Straumann<sup>39</sup>, V. K. Subbiah<sup>37</sup>, L. Sun<sup>56</sup>, W. Sutcliffe<sup>52</sup>, S. Swientek<sup>9</sup>, V. Syropoulos<sup>41</sup>, M. Szczekowski<sup>27</sup>, P. Szczypka<sup>38,37</sup>, D. Szilard<sup>2</sup>, T. Szumlak<sup>26</sup>, S. T'Jampens<sup>4</sup>, M. Teklishyn<sup>7</sup>, G. Tellarini<sup>16,e</sup>, E. Teodoro<sup>28</sup>, F. Teubert<sup>37</sup>, C. Thomas<sup>54</sup>, E. Thomas<sup>37</sup>, J. van Tilburg<sup>11</sup>, V. Tisserand<sup>4</sup>, M. Tobin<sup>38</sup>, S. Tolk<sup>41</sup>, L. Tomassetti<sup>16,e</sup>, D. Tonelli<sup>37</sup>, S. Topp-Joergensen<sup>54</sup>, N. Torr<sup>54</sup>, E. Tournefier<sup>4,52</sup>, S. Tourneur<sup>38</sup>, M. T. Tran<sup>38</sup>, M. Tresch<sup>39</sup>, A. Tsaregorodtsev<sup>6</sup>, P. Tsopelas<sup>40</sup>, N. Tuning<sup>40,37</sup>, M. Ubeda Garcia<sup>37</sup>, A. Ukleja<sup>27</sup>, A. Ustyuzhanin<sup>52,p</sup>, U. Uwer<sup>11</sup>, V. Vagnoni<sup>14</sup>, G. Valenti<sup>14</sup>, A. Vallier<sup>7</sup>, R. Vazquez Gomez<sup>18</sup>, P. Vazquez Regueiro<sup>36</sup>, C. Vázquez Sierra<sup>36</sup>, S. Vecchi<sup>16</sup>, J. J. Velthuis<sup>45</sup>, M. Veltri<sup>17,g</sup>, G. Veneziano<sup>38</sup>, M. Vesterinen<sup>37</sup>, B. Viaud<sup>7</sup>, D. Vieira<sup>2</sup>, X. Vilasis-Cardona<sup>35,n</sup>, A. Vollhardt<sup>39</sup>, D. Volynskiy<sup>10</sup>, D. Voong<sup>45</sup>, A. Vorobyev<sup>29</sup>, V. Vorobyev<sup>33</sup>, C. Voß<sup>60</sup>, H. Voss<sup>10</sup>, R. Waldi<sup>60</sup>, C. Wallace<sup>47</sup>, R. Wallace<sup>12</sup>, S. Wandernoth<sup>11</sup>, J. Wang<sup>58</sup>, D. R. Ward<sup>46</sup>, N. K. Watson<sup>44</sup>, A. D. Webber<sup>53</sup>, D. Websdale<sup>52</sup>, M. Whitehead<sup>47</sup>, J. Wicht<sup>37</sup>, J. Wiechczynski<sup>25</sup>, D. Wiedner<sup>11</sup>, L. Wiggers<sup>40</sup>, G. Wilkinson<sup>54</sup>, M. P. Williams<sup>47,48</sup>, M. Williams<sup>55</sup>, F. F. Wilson<sup>48</sup>, J. Wimperley<sup>57</sup>, J. Wishahi<sup>9</sup>, W. Wislicki<sup>27</sup>, M. Wittek<sup>25</sup>, G. Wormser<sup>7</sup>, S. A. Wotton<sup>46</sup>, S. Wright<sup>46</sup>, S. Wu<sup>3</sup>, K. Wyllie<sup>37</sup>, Y. Xie<sup>49,37</sup>, Z. Xing<sup>58</sup>, Z. Yang<sup>3</sup>, X. Yuan<sup>3</sup>, O. Yushchenko<sup>34</sup>, M. Zangoli<sup>14</sup>, M. Zaverdyayev<sup>10,a</sup>, F. Zhang<sup>3</sup>, L. Zhang<sup>58</sup>, W. C. Zhang<sup>12</sup>, Y. Zhang<sup>3</sup>, A. Zhelezov<sup>11</sup>, A. Zhokhov<sup>30</sup>, L. Zhong<sup>3</sup>, A. Zvyagin<sup>37</sup>

- <sup>10</sup> Max-Planck-Institut für Kernphysik (MPIK), Heidelberg, Germany  
<sup>11</sup> Physikalisches Institut, Ruprecht-Karls-Universität Heidelberg, Heidelberg, Germany  
<sup>12</sup> School of Physics, University College Dublin, Dublin, Ireland  
<sup>13</sup> Sezione INFN di Bari, Bari, Italy  
<sup>14</sup> Sezione INFN di Bologna, Bologna, Italy  
<sup>15</sup> Sezione INFN di Cagliari, Cagliari, Italy  
<sup>16</sup> Sezione INFN di Ferrara, Ferrara, Italy  
<sup>17</sup> Sezione INFN di Firenze, Firenze, Italy  
<sup>18</sup> Laboratori Nazionali dell'INFN di Frascati, Frascati, Italy  
<sup>19</sup> Sezione INFN di Genova, Genova, Italy  
<sup>20</sup> Sezione INFN di Milano Bicocca, Milano, Italy  
<sup>21</sup> Sezione INFN di Padova, Padova, Italy  
<sup>22</sup> Sezione INFN di Pisa, Pisa, Italy  
<sup>23</sup> Sezione INFN di Roma Tor Vergata, Roma, Italy  
<sup>24</sup> Sezione INFN di Roma La Sapienza, Roma, Italy  
<sup>25</sup> Henryk Niewodniczanski Institute of Nuclear Physics Polish Academy of Sciences, Kraków, Poland  
<sup>26</sup> AGH – University of Science and Technology, Faculty of Physics and Applied Computer Science, Kraków, Poland  
<sup>27</sup> National Center for Nuclear Research (NCBJ), Warsaw, Poland  
<sup>28</sup> Horia Hulubei National Institute of Physics and Nuclear Engineering, Bucharest-Magurele, Romania  
<sup>29</sup> Petersburg Nuclear Physics Institute (PNPI), Gatchina, Russia  
<sup>30</sup> Institute of Theoretical and Experimental Physics (ITEP), Moscow, Russia  
<sup>31</sup> Institute of Nuclear Physics, Moscow State University (SINP MSU), Moscow, Russia  
<sup>32</sup> Institute for Nuclear Research of the Russian Academy of Sciences (INR RAN), Moscow, Russia  
<sup>33</sup> Budker Institute of Nuclear Physics (SB RAS) and Novosibirsk State University, Novosibirsk, Russia  
<sup>34</sup> Institute for High Energy Physics (IHEP), Protvino, Russia  
<sup>35</sup> Universitat de Barcelona, Barcelona, Spain  
<sup>36</sup> Universidad de Santiago de Compostela, Santiago de Compostela, Spain  
<sup>37</sup> European Organization for Nuclear Research (CERN), Geneva, Switzerland  
<sup>38</sup> Ecole Polytechnique Fédérale de Lausanne (EPFL), Lausanne, Switzerland  
<sup>39</sup> Physik-Institut, Universität Zürich, Zürich, Switzerland  
<sup>40</sup> Nikhef National Institute for Subatomic Physics, Amsterdam, The Netherlands  
<sup>41</sup> Nikhef National Institute for Subatomic Physics and VU University Amsterdam, Amsterdam, The Netherlands  
<sup>42</sup> NSC Kharkiv Institute of Physics and Technology (NSC KIPT), Kharkiv, Ukraine  
<sup>43</sup> Institute for Nuclear Research of the National Academy of Sciences (KINR), Kyiv, Ukraine  
<sup>44</sup> University of Birmingham, Birmingham, United Kingdom  
<sup>45</sup> H.H. Wills Physics Laboratory, University of Bristol, Bristol, United Kingdom  
<sup>46</sup> Cavendish Laboratory, University of Cambridge, Cambridge, United Kingdom  
<sup>47</sup> Department of Physics, University of Warwick, Coventry, United Kingdom  
<sup>48</sup> STFC Rutherford Appleton Laboratory, Didcot, United Kingdom  
<sup>49</sup> School of Physics and Astronomy, University of Edinburgh, Edinburgh, United Kingdom  
<sup>50</sup> School of Physics and Astronomy, University of Glasgow, Glasgow, United Kingdom  
<sup>51</sup> Oliver Lodge Laboratory, University of Liverpool, Liverpool, United Kingdom  
<sup>52</sup> Imperial College London, London, United Kingdom  
<sup>53</sup> School of Physics and Astronomy, University of Manchester, Manchester, United Kingdom  
<sup>54</sup> Department of Physics, University of Oxford, Oxford, United Kingdom  
<sup>55</sup> Massachusetts Institute of Technology, Cambridge, MA, United States  
<sup>56</sup> University of Cincinnati, Cincinnati, OH, United States  
<sup>57</sup> University of Maryland, College Park, MD, United States  
<sup>58</sup> Syracuse University, Syracuse, NY, United States  
<sup>59</sup> Pontifícia Universidade Católica do Rio de Janeiro (PUC-Rio), Rio de Janeiro, Brazil<sup>t</sup>  
<sup>60</sup> Institut für Physik, Universität Rostock, Rostock, Germany<sup>u</sup>  
<sup>61</sup> KVI-University of Groningen, Groningen, The Netherlands<sup>v</sup>  
<sup>62</sup> Celal Bayar University, Manisa, Turkey<sup>w</sup>

<sup>a</sup> P.N. Lebedev Physical Institute, Russian Academy of Science (LPI RAS), Moscow, Russia.

<sup>b</sup> Università di Bari, Bari, Italy.

<sup>c</sup> Università di Bologna, Bologna, Italy.

<sup>d</sup> Università di Cagliari, Cagliari, Italy.

<sup>e</sup> Università di Ferrara, Ferrara, Italy.

<sup>f</sup> Università di Firenze, Firenze, Italy.

<sup>g</sup> Università di Urbino, Urbino, Italy.

<sup>h</sup> Università di Modena e Reggio Emilia, Modena, Italy.

<sup>i</sup> Università di Genova, Genova, Italy.

<sup>j</sup> Università di Milano Bicocca, Milano, Italy.

<sup>k</sup> Università di Roma Tor Vergata, Roma, Italy.

<sup>l</sup> Università di Roma La Sapienza, Roma, Italy.

<sup>m</sup> Università della Basilicata, Potenza, Italy.

<sup>n</sup> LIFAELS, La Salle, Universitat Ramon Llull, Barcelona, Spain.

<sup>o</sup> Hanoi University of Science, Hanoi, Viet Nam.

<sup>p</sup> Institute of Physics and Technology, Moscow, Russia.

<sup>q</sup> Università di Padova, Padova, Italy.

<sup>r</sup> Università di Pisa, Pisa, Italy.

<sup>s</sup> Scuola Normale Superiore, Pisa, Italy.

<sup>t</sup> Associated to Universidade Federal do Rio de Janeiro (UFRJ), Rio de Janeiro, Brazil.

<sup>u</sup> Associated to Physikalisches Institut, Ruprecht-Karls-Universität Heidelberg, Heidelberg, Germany.

<sup>v</sup> Associated to Nikhef National Institute for Subatomic Physics, Amsterdam, The Netherlands.

<sup>w</sup> Associated to European Organization for Nuclear Research (CERN), Geneva, Switzerland.

## B

### Calculating fit fractions in $\text{Rio}^+$ .

#### B.1

##### Fractions and errors for the amplitude-phase form.

In the simple isobar model the decay amplitude is

$$\mathcal{A} = \sum a_j e^{i\delta_j} A_j(s_1, s_2).$$

In this way, the parameter space is generated by the  $2n$  parameters  $(a_j, \delta_j)$ .

If we define  $N_f$  as the integral over the whole phase space of the signal PDF, then:

$$N_f = \int ds_1 ds_2 \left| \sum a_j e^{i\delta_j} A_j \right|^2 = \left| \sum a_j a_k e^{i(\delta_j - \delta_k)} \underbrace{\int ds_1 ds_2 A_j A_k^*}_{N_{jk}} \right|,$$

$$N_f = \left| \sum a_j a_k e^{i(\delta_j - \delta_k)} N_{jk} \right|.$$

The decay fraction  $f_i$  is defined as

$$f_i = \frac{\int ds_1 ds_2 |A_i|^2}{N_f} = \frac{a_i^2 \cdot N_{ii}}{N_f}$$

The error on the fraction  $f_i$  is given by

$$(\delta f_i)^2 = \sum_{j,k} \frac{\partial f_i}{\partial \alpha_j} \frac{\partial f_i}{\partial \alpha_k} \text{cov}(\alpha_j, \alpha_k)$$

We have to calculate the derivatives  $\frac{\partial f_i}{\partial \alpha_j}$  and  $\frac{\partial f_i}{\partial \alpha_k}$  each of which includes the derivative of  $N_f$ . We show here the general expression for the first case:

$$\frac{\partial f_i}{\partial \alpha_k} = \frac{\partial}{\partial \alpha_k} \left( \frac{a_i^2 N_{ii}}{N_f} \right) = \frac{\frac{\partial}{\partial \alpha_k} a_i^2 N_{ii}}{N_f} - \frac{a_i^2 N_{ii}}{N_f^2} \frac{\partial N_f}{\partial \delta_k}$$

$$\frac{\partial N_f}{\partial a_k} = \frac{\partial}{\partial a_k} \sum_{i,j} a_i a_j e^{i(\delta_i - \delta_j)} N_{ij} = \sum_{i,j} a_j e^{i(\delta_i - \delta_j)} N_{ij} + \sum_{i,j} a_i e^{i(\delta_i - \delta_j)} N_{ij}$$

using the sine and cosine parities and the fact that  $N_{ij} + N_{ji} = 2\text{Re}(N_{ij})$ ,

we have:

$$\frac{\partial N_f}{\partial a_k} = \sum_{i,j} a_i \cos(\delta_i - \delta_j) (2\mathcal{R}e(N_{ij})) = 2 \sum_{i,j} \mathcal{R}e(a_i e^{i(\delta_i - \delta_j)} N_{ij})$$

Similarly for the derivative on  $\delta$ :

$$\frac{\partial N_f}{\partial \delta_k} = -2 \sum_{i,j} \mathcal{I}m(a_i a_j e^{i(\delta_i - \delta_j)} N_{ij})$$

The error on the decay fraction is

$$\frac{\partial f_i}{\partial a_k} = \frac{\partial}{\partial a_k} \left( \frac{a_i^2 N_{ii}}{N_f} \right) = \frac{2a_i}{N_f} N_{ii} \delta_{ik} - \frac{a_i^2 N_{ii}}{N_f^2} \frac{\partial N_f}{\partial a_k}$$

$$\frac{\partial f_i}{\partial \delta_k} = \frac{\partial}{\partial \delta_k} \left( \frac{a_i^2 N_{ii}}{N_f} \right) = -\frac{a_i^2 N_{ii}}{N_f^2} \frac{\partial N_f}{\partial \delta_k}$$

(B-1)

## 2) Fractions and errors for the real-imaginary form.

In this case, the decay amplitude is given by

$$\mathcal{A} = \sum (a_j + ib_j) A_j(s_1, s_2).$$

The expression for  $N_f$  is

$$N_f = \int ds_1 ds_2 \left| \sum (a_j + ib_j) A_j \right|^2 = \left| \sum (a_j + ib_j)(a_k - ib_k) \underbrace{\int ds_1 ds_2 A_j A_k^*}_{N_{jk}} \right|,$$

$$N_f = \left| \sum [(a_j a_k + b_j b_k) + i(a_k b_j - a_j b_k)] N_{jk} \right|.$$

And the correspondent expression for the fraction is

$$f_i = \frac{(a_i^2 + b_i^2) \cdot N_{ii}}{N_f}$$

in this sense, the error caused by  $b$  in  $N_f$  is given by

$$\frac{\partial N_f}{\partial b_k} = \frac{\partial}{\partial b_k} \sum_{i,j} [(a_i a_j + b_i b_j) + i(a_j b_i - a_i b_j) N_{ij}] = \sum_{i,j} (b_j + i a_j) N_{ij} + \sum_{i,j} (b_i - i a_i) N_{ij}$$

$$\frac{\partial N_f}{\partial b_k} = \sum_{i,j} b_j (N_{ij} + N_{ji}) = 2 \sum_{i,j} \mathcal{R}e(b_j N_{ij}).$$

Similarly for  $a$ :

$$\frac{\partial N_f}{\partial a_k} = 2 \sum_{i,j} \mathcal{R}e(a_j N_{ij}).$$

The error on the decay fraction is

$$\boxed{\begin{aligned} \frac{\partial f_i}{\partial a_k} &= \frac{\partial}{\partial a_k} \left( \frac{(a_i^2 + b_i^2) N_{ii}}{N_f} \right) = \frac{2a_i}{N_f} N_{ii} \delta_{ik} - \frac{(a_i^2 + b_i^2) N_{ii}}{N_f^2} \frac{\partial N_f}{\partial a_k} \\ \frac{\partial f_i}{\partial b_k} &= \frac{\partial}{\partial b_k} \left( \frac{(a_i^2 + b_i^2) N_{ii}}{N_f} \right) = \frac{2b_i}{N_f} N_{ii} \delta_{ik} - \frac{(a_i^2 + b_i^2) N_{ii}}{N_f^2} \frac{\partial N_f}{\partial b_k} \end{aligned}} \quad (\text{B-2})$$

## B.2

### Interference fractions and errors for the amplitude-phase form.

In this case, the fraction for the interference between the resonances  $i$  and  $j$  is expressed as:

$$f_{ij} = \frac{\int ds_1 ds_2 |A_i A_j^*|}{N_f} = 2 \frac{a_i a_j N_{ij}}{N_f}$$

The error on the interference fraction is given by

$$(\delta f_{ij})^2 = \sum_{k,l} \frac{\partial f_{ij}}{\partial \alpha_k} \frac{\partial f_{ij}}{\partial \alpha_l} \text{cov}(\alpha_k, \alpha_l)$$

The derivatives are given by:

$$\frac{\partial f_{ij}}{\partial \alpha_k} = \frac{\partial}{\partial \alpha_k} \left( \frac{a_i a_j N_{ij}}{N_f} \right) = \frac{\frac{\partial}{\partial \alpha_k} a_i a_j N_{ij}}{N_f} - \frac{a_i a_j N_{ij}}{N_f^2} \frac{\partial N_f}{\partial \alpha_k}$$

$$\frac{\partial f_{ij}}{\partial \alpha_k} = \left( \frac{\partial a_i}{\partial \alpha_k} a_j + \frac{\partial a_j}{\partial \alpha_k} a_i \right) \frac{N_{ij}}{N_f} - \frac{a_i a_j N_{ij}}{N_f^2} \frac{\partial N_f}{\partial \alpha_k}$$

The  $\frac{\partial N_f}{\partial \alpha_k}$  and  $\frac{\partial N_f}{\partial \delta_k}$  derivatives are already calculated above, so the total expression for the errors on the interference fractions is given by:

$$\boxed{\begin{aligned} \frac{\partial f_{ij}}{\partial a_k} &= \frac{\partial}{\partial a_k} \left( \frac{a_i a_j N_{ij}}{N_f} \right) = (a_i \delta_{jk} + a_j \delta_{ik}) \frac{N_{ij}}{N_f} - \frac{a_i a_j N_{ij}}{N_f^2} \frac{\partial N_f}{\partial a_k} \\ \frac{\partial f_{ij}}{\partial \delta_k} &= \frac{\partial}{\partial \delta_k} \left( \frac{a_i a_j N_{ij}}{N_f} \right) = - \frac{a_i a_j N_{ij}}{N_f^2} \frac{\partial N_f}{\partial \delta_k} \end{aligned}} \quad (\text{B-3})$$

As the total interference fraction is equal to  $f_{ij} + f_{ji}$ , the total error equals to:

$$Err_{ij} = \sqrt{(\delta f_{ij})^2 + (\delta f_{ji})^2} = \sqrt{2} (\delta f_{ij})$$